UTILIZING LASER DIRECT WRITING TO FABRICATE *IN VITRO* BIOENGINEERED SYSTEMS

FOR ELUCIDATING CELLULAR DYNAMICS IN BREAST TUMOR AND WOUND

MICROENVIRONMENTS

AN ABSTRACT

SUBMITTED ON THE SEVENTEENTH DAY OF JANUARY 2023

TO THE DEPARTMENT OF BIOMEDICAL ENGINEERING

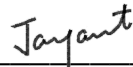IN PARTIAL FULFILLMENT OF THE REQUIREMENTS

OF THE SCHOOL OF SCIENCE AND ENGINEERING

OF TULANE UNIVERSITY

FOR THE DEGREE

OF DOCTOR OF PHILOSOPHY

BY

_____
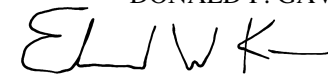JAYANT SAKSENA

APPROVED: _____
DOUGLAS B. CHRISEY, Ph.D.
Director

_____
MATTHEW E. BUROW, Ph.D.

_____
DONALD P. GAVER, Ph.D.

_____
EDWARD W. KARP, MBA

Abstract

Laser direct writing is a powerful technique to additively and subtractively process biological materials for fabricating *in vitro* bioengineered constructs. Additive laser direct write processing involves cell printing at a resolution which exceeds that of conventional bioprinting techniques, and enables precise patterning of cells for studying cellular interactions. Subtractive laser direct write processing involves CAD/CAM photoablation, which allows for precise etching of biological substrates, including tissues and cell layers, in user-defined geometries for designing a variety of experimental models. A next-generation laser direct write platform was developed by re-engineering an excimer laser to enhance its output energy and subsequently configuring control systems for the laser and other components of the instrument while ensuring reliable and robust functionality.

The additive capability of the laser direct write system was utilized to bioprint the breast tumor microenvironment, within which the most enriched cell types are the cancer cells, cancer-associated fibroblasts and tumor-associated macrophages. A novel protocol was developed to print heterocellular breast cancer-fibroblast arrays, with homotypic and heterotypic spots in defined geometries, to allow for study of cancer-stromal interactions. As conventional

bioprinted constructs generally lack the immune component, another novel protocol was developed to viably bioprint human macrophages *in vitro* with high fidelity, paving the way for bioprinted immunocompetent constructs for modeling not just breast cancer but disparate healthy and diseased tissue microenvironments.

The subtractive capability of LDW was utilized to develop novel photoablated wound healing assays. A method to photoablate wounds of any given geometry was developed and utilized to elucidate the role of wound symmetry in diabetic dermal wounds. Symmetric dermal wounds were found to heal at faster rates even after controlling for glycemic conditions. Further, a reaction-diffusion based mathematical model was combined with precise laser photoablation to decouple the contributions of cell migration and proliferation to wound closure. This assay was then utilized to investigate the influence of stromal and adipose signaling on breast cancer metastasis, as well as the influence of growth factors and cytokines on cutaneous wound healing. Using patient-derived xenograft cells, juxtacrine stromal signaling was found to enhance breast cancer cell migration and proliferation, an effect that could be recapitulated *in vitro* by co-culturing patient-derived cancer cells with human fibroblasts. Next, using adipose-derived stem cells harvested from lean and obese patients, paracrine obese adipose signaling was found to enhance breast cancer cell proliferation while paracrine lean adipose signaling was found to enhance breast cancer cell

motility. Finally, continuous epidermal growth factor treatment was found to enhance dermal fibroblast migration and proliferation in wounds, while intermittent tumor necrosis factor alpha treatment was found to enhance fibroblast proliferation but suppress migration.

Collectively, these bioengineered systems demonstrate the value of the dual additive and subtractive processing functionality of the laser direct write platform for fabricating novel *in vitro* experimental model systems, which can lead to physiologically relevant insights that may not have been revealed using conventional techniques, and thereby accelerate discovery of novel therapeutic targets and drugs.

UTILIZING LASER DIRECT WRITING TO FABRICATE *IN VITRO* BIOENGINEERED SYSTEMS FOR ELUCIDATING CELLULAR DYNAMICS IN BREAST TUMOR AND WOUND MICROENVIRONMENTS

A DISSERTATION

SUBMITTED ON THE SEVENTHEENTH DAY OF JANUARY 2023

TO THE DEPARTMENT OF BIOMEDICAL ENGINEERING
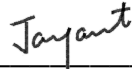
IN PARTIAL FULFILLMENT OF THE REQUIREMENTS

OF THE SCHOOL OF SCIENCE AND ENGINEERING

OF TULANE UNIVERSITY

FOR THE DEGREE

OF DOCTOR OF PHILOSOPHY

BY

_____
JAYANT SAKSENA

APPROVED: _____
DOUGLAS B. CHRISEY, Ph.D.
Director

_____
MATTHEW E. BUROW, Ph.D.

_____
DONALD P. GAVER, Ph.D.

_____
EDWARD W. KARP, MBA

Acknowledgements

As I write this dissertation and reflect on my PhD journey, it is difficult to overstate the amount of gratitude I feel towards my advisor, Prof. Douglas Chrisey, and the Biomedical Engineering Department at Tulane University for their unwavering patience and support. This has truly been a once-in-a-lifetime opportunity and I could not have asked for a better environment to train and grow as a scientist and engineer.

I would especially like to thank Prof. Chrisey, whose brilliantly sharp critiques encouraged me to not only maintain rigor in my research but to also constantly challenge my thinking and broaden my perspective as a bioengineer. His high expectations pushed me to develop attributes essential for a successful career as a scientist, and provided me with experiences that enabled me to mature into an independent scholar. Throughout the turmoil of the COVID-19 pandemic and Hurricane Ida, his support was unerring – for which I am eternally grateful. I will always cherish our discussions, during which we shared our excitement and

passion about biomedical research, and I was also fortunate to receive some insightful career and life advice.

I would also like to thank Prof. Matthew Burow and his lab members for being receptive to my ideas as without their collaboration, none of this work would have been possible. Burrow Lab members – past and present – have assisted me in procuring cells and reagents, and have offered vitally important feedback that has shaped my projects. For this, I thank them individually – Prof. Burow, Van Hoang, Hope Burks, Margarite Matossian, Maryl Wright, Madlin Alzoubi, Khoa "Andy" Nguyen, and Katherine Hebert. A special mention goes to the lab manager Steven Elliot, whose input and assistance in facilitating my day-to-day research tasks has been absolutely indispensable.

I thank my dissertation committee members – Profs. Douglas Chrisey, Matthew Burow, Donald Gaver and Edward Karp – for this opportunity to explore novel biological questions and test my hypotheses, as well as for their feedback, patience and support. My committee members' perspectives have been crucial in terms of interpreting my results and formulating approaches for translating the technologies I developed beyond the laboratory.

Table of Contents

List of Figures

List of Tables

1 Background

1.1 Additive laser direct write processing: Matrix assisted pulsed laser evaporation bioprinting

Bioprinting – which involves the adaptation of additive manufacturing (of which three-dimensional printing is the most important example) technologies to print cells and biological materials in order to create functional biological constructs – is widely expected to revolutionize medicine and biomedical research. There exist various kinds of bioprinting techniques – broadly categorized as extrusion, droplet/inkjet and laser based – each with its own advantages, limitations and applications [1] .

Extrusion based bioprinting is the most common bioprinting technique and relies on pressure to transfer bioinks onto the receiving substrate [1]. While able to print cells at high densities and transfer large volumes, extrusion based bioprinting offers low resolution, little control in patterning cells, poor cell viability and functionality and requires shear thinning bioinks [2].

Inkjet bioprinting relies on one or a combination of localized heat or electrostatic energy, acoustic or piezoelectric forces, and magnetically regulated microvalves to deliver volume-controlled droplets of material to specified

locations [1]. While capable of higher resolution than extrusion-based technologies, suffers from drawbacks associated with nozzle-based techniques – such as frequent nozzle clogging and unable to print high cell densities – as well as lower cell viability due to cytotoxicity during the crosslinking process [2].

Laser direct write bioprinting, also known as matrix-assisted pulsed laser evaporation bioprinting, has the unique ability of mimicking the complexity of human tissue at the cellular scale, thereby giving us the control to pattern cells at high resolution, and to control cell-cell interaction and potentially "build" a tissue piece-by-piece rather than simply growing it. It has further advantages in terms of automation, reproducibility and high throughput [3] [4] [5].

Laser direct write bioprinting utilizes an 8ns pulsed excimer UV-C (193nm) laser beam focused on a print ribbon (term derived from analogy to typewriters). The ribbon is typically made of quartz, and is optically transparent for both UV (to allow transmission of the laser beam for printing) and visible (to allow for real-time imaging of the cells) wavelengths. The ribbon is coated on the underside with bioink, which contains the cells to be printed. The cells are suspended in a sacrificial matrix layer, typically a low viscosity biopolymer such as a hydrogel. Although initially, Matrigel was used as the ribbon matrix, gelatin has been demonstrated to be a cheaper and more effective alternative [5] [6] [7]. The gelatin layer acts as an absorption medium which not only results in forward transfer of cell-laden droplets but also protects cells from the adverse effects of

2

laser radiation as it facilitates the conversion of electromagnetic energy to mechanical energy [3]. According to the Beer-Lambert law, the penetration depth of UV-C radiation in a sufficiently concentrated hydrogel is <<10um as UV-C radiation is primarily absorbed by macromolecules [8] and the laser radiation never comes into direct contact with the cells. The laser direct write cell printing process can be thought of as a "contactless typewriter" for cells and is schematically depicted in Figure 1-1.
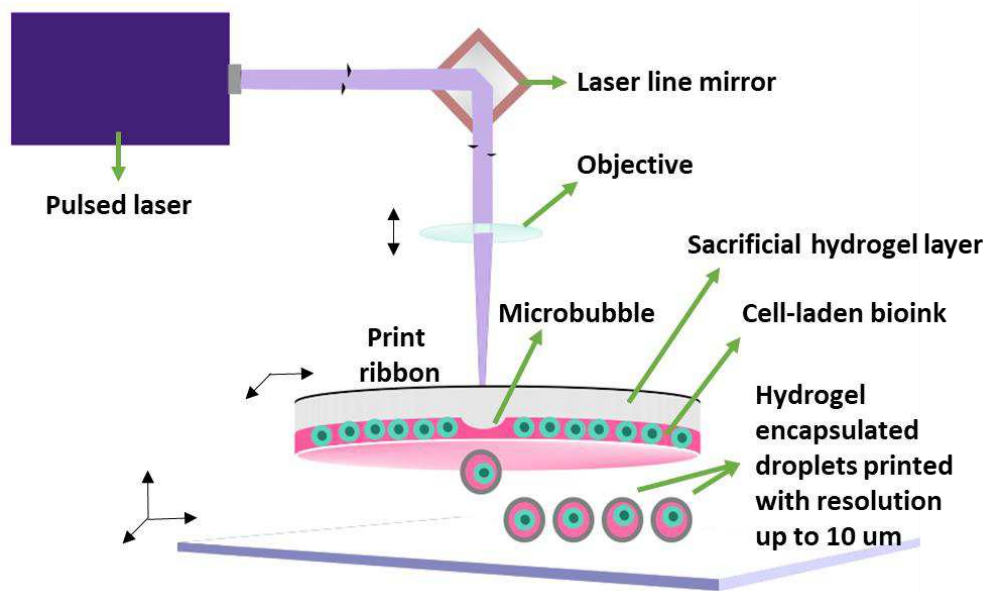
Figure 1-1 Laser direct write bioprinting process (image not to scale)

As the laser beam is focused on the ribbon-hydrogel interface, it causes superheating of the water vapor in the hydrogel, which results in the formation

3

of a cavitation microbubble due to the phenomenon of "phase explosion". This cavitation bubble expands and collapses rapidly, generating a short-lived shockwave the results in the pressure pulse that propels the cell-laden droplet onto the substrate. For nanosecond laser pulses, the forward transfer process occurs on the microsecond timescale. The phases of laser induced forward transfer are depicted in Figure 1-2, Figure 1-3 and Figure 1-4 [3].
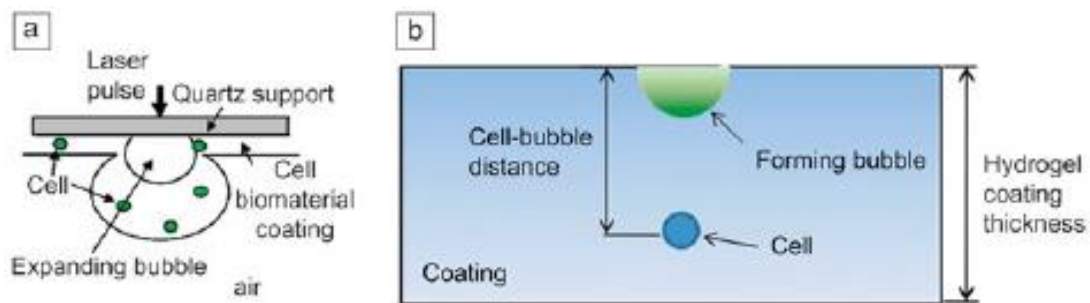
Figure 1-2 Cavitation bubble formation and expansion [3]

As the cell-laden droplet is being transferred towards the substrate, the hydrogel encapsulates the cells, cushioning them from shear stress when the droplet lands on the harder substrate [3]. This results in laser direct write bioprinting being extremely gentle on the cells, resulting in high post-printing cell viability.

The substrate and ribbon are mounted on motorized CAD/CAM stages which can be programmed to move in any pattern, allowing for cells to be patterned in complex, user-defined geometries.
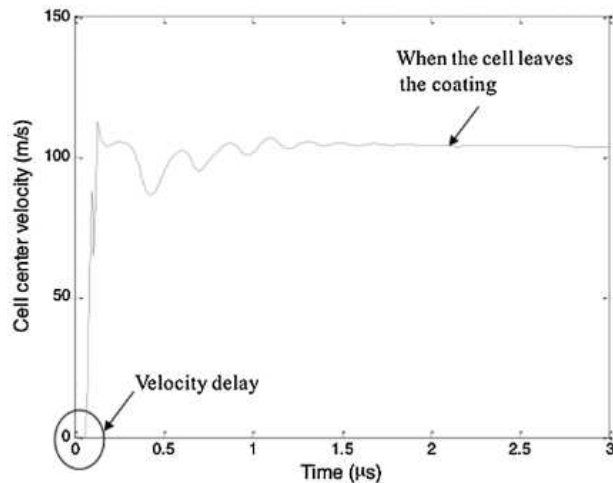
Figure 1-3 Short-lived shockwave that propels cell-laden droplet forward [3]

Laser induced forward transfer only occurs when the laser fluence exceeds the threshold ablation fluence of the hydrogel layer that is coated on the ribbon. At sub-threshold fluence, there is no forward transfer. On the other hand, if fluence is much higher than the threshold, the ejected droplet rapidly deforms transversely resulting in a divergent plume. If any cells were contained in the droplet, they would get scattered instead of printed and will likely be nonviable. However, if the fluence slightly exceeds the ablation threshold of the hydrogel, a columnar jet is produced. In this "jetting regime", the printed spot closely

5

resembles the laser spot size [9]. This allows for tight control over the number of cells printed and with a small enough laser spot size, single cell resolution can be achieved. Since the columnar jet is short lived, it is important to have the substrate surface extremely close to the ribbon (<500um, ideally <100um) and thus the substrate and ribbon stages are mounted on motorized Z-stages to allow for this adjustment.
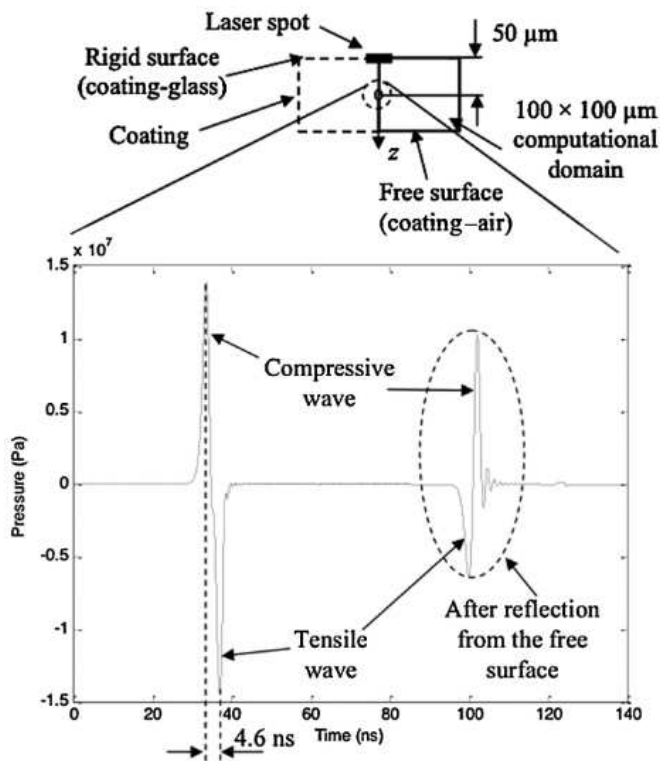
Figure 1-4 Pressure pulse that results in droplet transfer to the substrate [3]

6

Hence, due to its precision, gentleness on cells, automation and reproducibility, laser direct write bioprinting enables patterning of cells at high resolution, which can allow for the fabrication of constructs to elucidate cell-cell interactions in disparate diseases. Going forward, it has the potential to fabricate complex vascularized tissues voxel-by-voxel in a bottom-up manner with high fidelity.

1.2 Subtractive laser direct write processing: CAD/CAM photoablation

Nanosecond pulsed ArF excimer lasers are among the best laser type for performing photoablation of biological substrates as they tend to etch in a very clean and exact manner with minimal appearance of thermal damage such as coagulation [8]. This is why they are widely used for corneal refractive surgeries, with laser-assisted *in situ* keratomileusis (LASIK) being the most widely be performed.

Hence, if the laser is focused directly on the substrate instead of the ribbon in the laser direct write system, owing to the CAD/CAM capability of the substrate stage, photoablation and etching of a biological substrate (including cells and tissues) reproducibly and predictably in any user-defined geometry is possible.

Absorption of high-energy UV photons
⇓
Promotion to repulsive excited states
⇓
Dissociation
⇓
Ejection of fragments (no necrosis)
⇓
Ablation
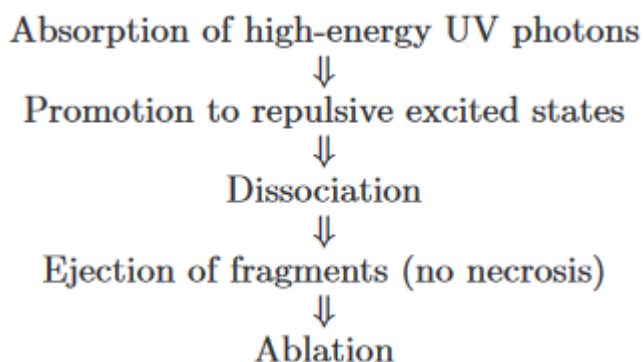
Figure 1-5 Principles of UV laser photoablation of biological substrates [8]

The ablation depth, i.e. the depth of tissue removal per pulse, is determined by the pulse energy up to a certain saturation limit, while the geometry of the ablation pattern itself is defined by the spatial parameters of the laser beam – making the process highly precise, predictable and reproducible. Areas adjacent to the laser path remain undamaged, making it ideal to ablate tissues and cell layers [8].

UV laser photoablation relies on overcoming the bond energy of carbon-carbon bonds in organic polymeric molecules, which comprise major structural elements of cells and tissues. Upon absorbing the UV photon, molecules are thus transitioned into the excited state based on the Frank-Condon principle and are amenable to dissociation at the very next vibrational state. The

dissociated photoproducts are normally ejected as single atoms and stable monomeric fragments, resulting in ablation [8]. This process is summarized in Figure 1-5.

Hence, the laser direct write system has the dual capability of accomplishing not just high-resolution printing (additive processing) but also highly precise photoablation (subtractive processing) of cells and tissues.

The following chapters discuss building a next-generation laser direct platform and utilizing it for both additive and subtractive processing applications, that are then biologically validated by performing assays that lead to elucidation of cell-cell interactions in the breast tumor and dermal wound microenvironments.

2 Specific Aims

Aim 1: Re-engineer the laser direct write system

<u>Sub aim 1(a)</u>: Diagnose issues and restore excimer laser functionality

<u>Sub aim 1(b)</u>: Enhance laser output energy to be conducive for processing of biological materials

<u>Sub aim 1(c)</u>: Configure control systems for all components of the laser direct write instrument

Aim 2: Utilize additive processing capability of laser direct write to bioprint the breast tumor microenvironment

<u>Sub aim 2(a)</u>: Bioprint heterocellular cancer-stromal arrays to study cell-cell interactions

<u>Sub aim 2(b)</u>: Bioprint human macrophages

Aim 3: Utilize subtractive processing capability of laser direct write to develop CAD/CAM wound healing assays

<u>Sub aim 3(a)</u>: Elucidate the role of geometry and glycemic conditions in dermal wound healing

Sub aim 3(b): Decoupling contributions of proliferation and migration in wound healing assays

Sub aim 3(c): Investigate the influence of stromal crosstalk on breast cancer metastasis

Sub aim 3(d): Investigate the influence of adipose crosstalk on breast cancer metastasis

Sub aim 3(e): Study the effect of EGF & TNF-α on cutaneous wound healing

3 Re-Engineering the Laser Direct Platform

3.1 System design requirements

In order to perform laser direct bioprinting and photoablation, several system design requirements needed to be met, which are discussed below.

First, the laser output energy needs to be high enough, such that after beam propagation to the work surface, the fluence (energy density) should exceed the ablation threshold of the hydrogel or cell layer for a range of spot sizes. A high enough laser output energy would also allow for higher resolution adjustment of fluences within a given (above threshold) range for optimization.

Second, the fluence needs to be tightly controlled at the work surface. For this, the laser spot size needs to be controlled using an automated variable aperture. In order to tightly control the laser beam energy and energy density, the laser parameters that influence output power need to be precisely controlled and monitored. Interfacing the laser and computer with a data acquisition (DAQ) card is hence required.

Third, the laser beam needs to be focused on the desired plane – the ribbon-hydrogel interface for bioprinting and the cell layer for photoablation. Hence,

both the substrate and the focusing objectives need to be mounted on motorized Z-stages.

Fourth, in order to print or ablate user-defined geometrical patterns, CAD/CAM (computer-aided design/manufacturing) functionality is required. Hence, the substrate and ribbon must be mounted on programmable computer-controlled XY stages.

Finally, all components need to be synchronized in a seamless workflow to allow for efficient operation and successful implementation of multistep bioprinting and photoablation protocols. This requires software configuration of all relevant components, ensuring that any driver conflicts and compatibility or legacy issues are eliminated.

3.2 System design

A suitable design for the next-generation laser direct write platform satisfying the above requirements is depicted in Figure 3-1. The list of components and their characteristics is summarized in Table 3-1.
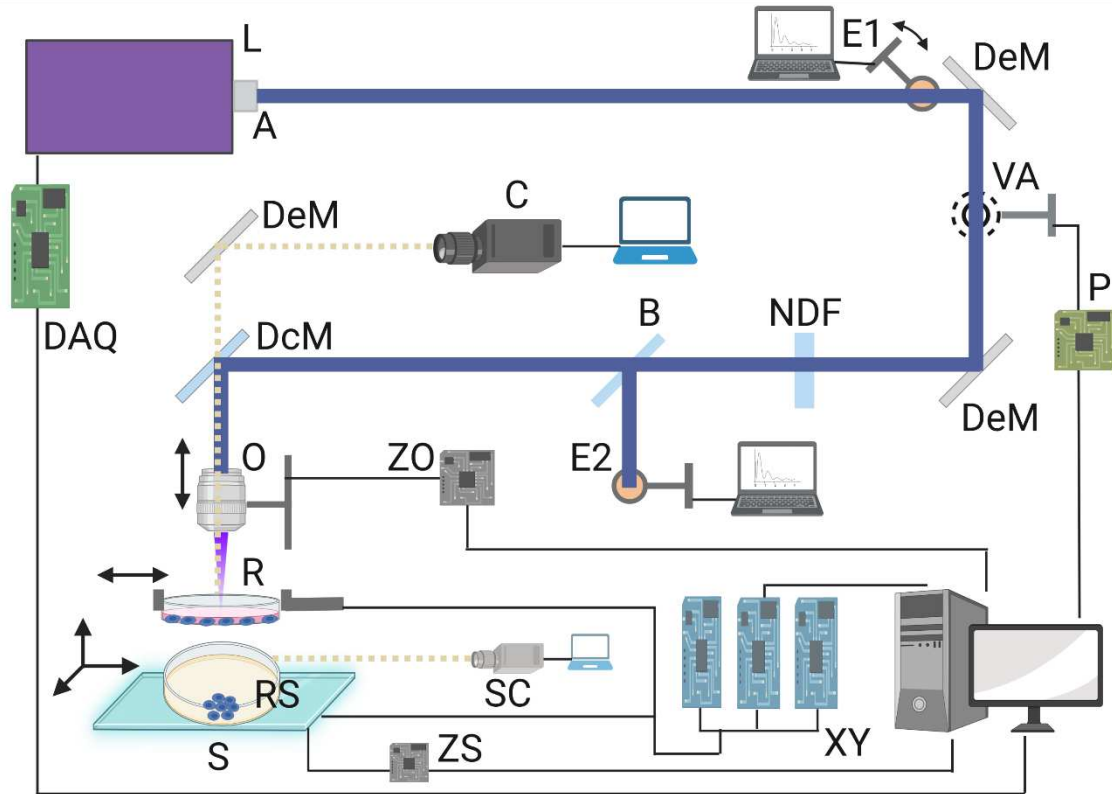
Figure 3-1 Laser direct write system schematic (symbols explained in table)

Table 3-1 Laser direct write system components, characteristics and functions

Symbol	Component	Characteristic/Function
L	Excimer laser	ArF gain medium, UV-C 193nm, 8ns pulse width
A	Laser aperture	Blocks part of beam to make it circular (as discharge between electrodes results in oblong beam)

DAQ	Data acquisition card	Interfaces laser electronics with computer, allows for precise control and monitoring of laser parameters
E1	In line energy meter	Measures laser energy just out of the laser at a distance of 50cm
DeM	Dieletric mirror	Highly reflective for UV-C (for laser) or visible light (for camera), turn the laser beam
VA	Variable aperture (iris)	Computer controlled
P	Piezoelectric controller	Interfaces iris with computer
NDF	Neutral density filter	Defined absorbance for UV-C, reduces laser beam energy by a highly defined amount, increases resolution for adjustment of fluence
B	Beamspliiter	Splits laser beam 90:10 and directs 10% into *in situ* energy meter
E2	*In situ* energy meter	Continuously monitors laser energy while printing and ablating; receives 10% of energy of the laser beam that has traveled 125cm

DcM	Dichroic mirror	High pass reflector, allows higher wavelengths (visible light) to pass through but has high reflectance for lower wavelength (UV laser beam)
O	5x objective	Focuses the laser beam
S	Substrate stage	Serves as platform for receiving or ablative substrate
R	Print ribbon	Made of quartz to be optically transparent to both UV and visible wavelengths; coated on underside with hydrogel and cells for bioprinting
RS	Receiving substrate dish	Substrate dish for bioprinting (or, with the ribbon removed, photoablation)
ZO	Objective Z-controller	Computer controlled micron resolution motion of objective
ZS	Substrate Z-controller	Computer controlled micron resolution motion of substrate stage

XY	Substrate XY controllers	Computer controlled and programmable motion with micron resolution to allow precise CAD/CAM functionality for printing and ablation
C	Telescopic camera	*In situ* camera to monitor bioprinting or photoablation in real time, optically aligned with laser and objective to simultaneously focus with the laser beam
SC	Side view camera	To ensure proximity of ribbon and substrate stage for jetting regime while bioprinting

3.3 Incident laser energy testing

The laser bream energy was tested at three locations: straight out of the laser at a distance of 50cm using the in-line, after passing through the iris and traveling a total of 125cm out of the laser using the *in situ* energy meter, and at work surface with the laser beam focused and having propagated 175cm out

of the laser using an externally mounted energy meter (Figure 3-2, Figure 3-3). The fluence was calculated at the surface after characterizing the spot size.

Since the distances traveled by the laser beam to reach the respective energy meters is fixed, there exists a defined relationship between the respective readings for a given configuration of the variable aperture and the neutral density filter, due to the inverse square law for UV radiation. This allows for accurate estimation of energy (and consequently, fluence) at the work surface and straight out of the laser by simply monitoring the *in situ* energy meter readings once the relationship has been characterized and established.

Laser energy was characterized over 10k pulses at 20Hz (minimum output pulse frequency of the excimer laser) and 100Hz (used for photoablation).
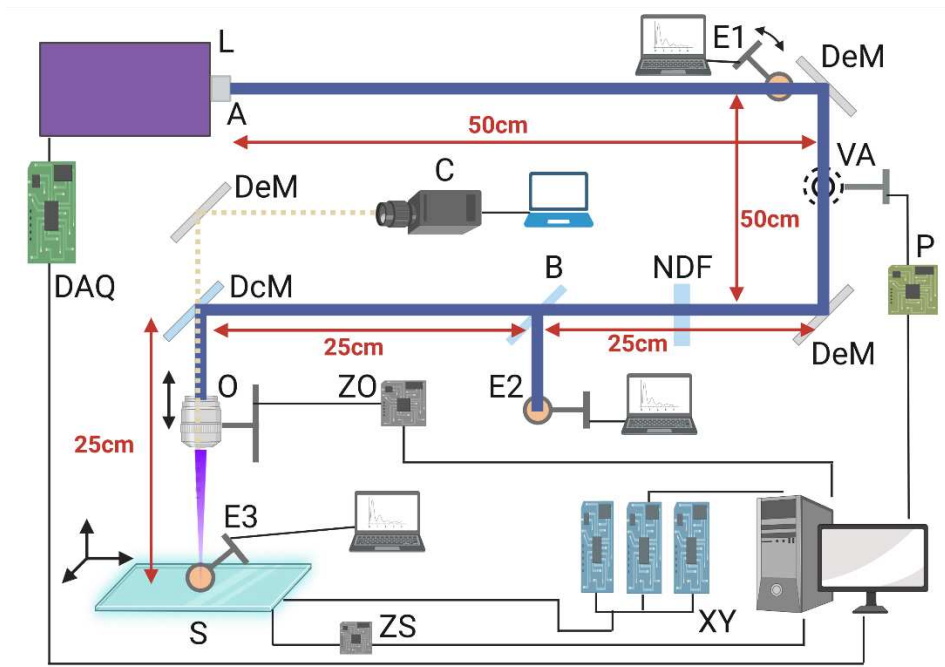
Figure 3-2 Laser energy testing

Figure 3-3 Laser energy meters (clockwise from top left): in line, work surface, in situ

3.4   Restoring laser functionality

The first step was to repair the excimer laser and make it functional. The laser was disassembled and issues with its electronics were diagnosed. The short circuited DC converter (power supply) board connector was replaced.   The laser's main control board was then reconfigured for new pin assignments to interface with the DAQ card (Figure 3-4). Proper safety precautions were followed at all times because the laser operates a very high voltage of 15kV and uses corrosive fluorine gas.

Once the laser functionality was restored, its output energy was found to be almost negligible and insufficient for bioprinting or photoablation.
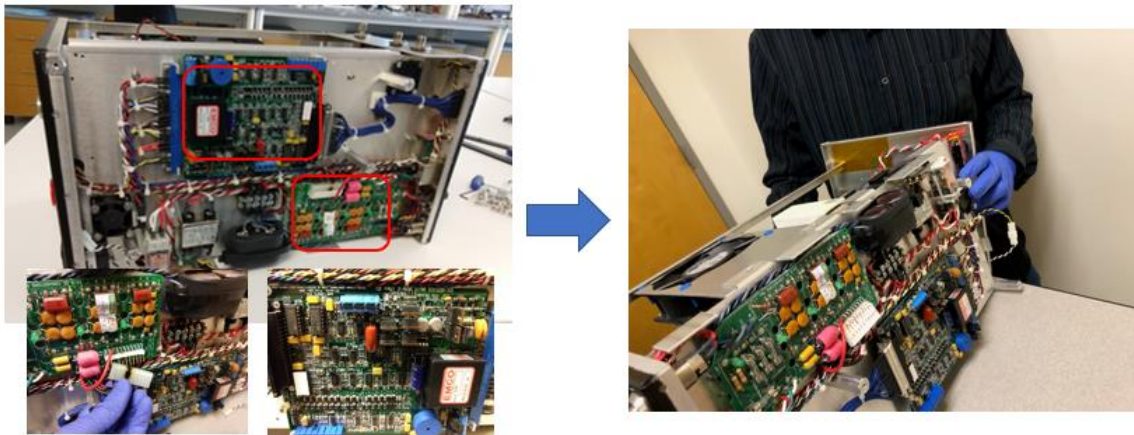
Figure 3-4 Repairing the excimer laser to restore functionality

3.5 Excimer laser principles

The next step was to enhance the laser energy output substantially from the nJ range to ~10mJ at full power (15kV discharge voltage) for bioprinting and photoablation. In order to do this, the Physics principles of excimer laser operation needed to be examined.

LASER is an acronym for light amplification by stimulated emission of radiation. The gain medium is externally pumped (in the lab laser, using a transverse gas discharge) to achieve population inversion to its excited state with excited Ar-F "dimers" (hence the name "excimer laser", although the correct technical term is "exciplex" laser since the excited state consists of an Ar-F excited complex). In this excited state, an incident photon matching the transition energy causes emission of another photon of the same energy (and hence the same frequency, according to Planck's Equation), polarization, phase and direction. This is known as stimulated emission (Figure 3-5). Due to the design of the reflectors in the resonator cavity, this occurs repeatedly in a chain reaction, resulting in a stimulated emission of a highly coherent laser beam (Figure 3-6).
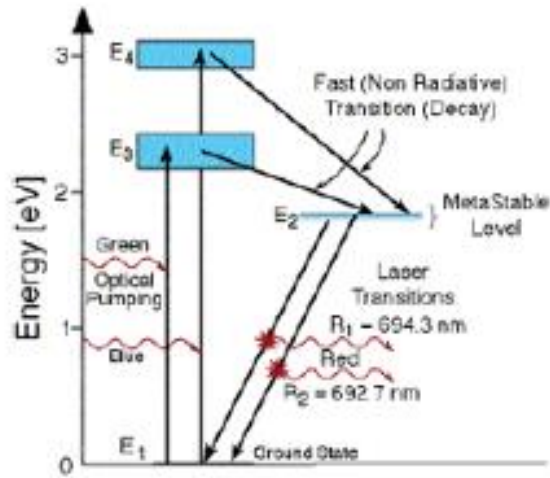
Figure 3-5 Stimulated emission [10]
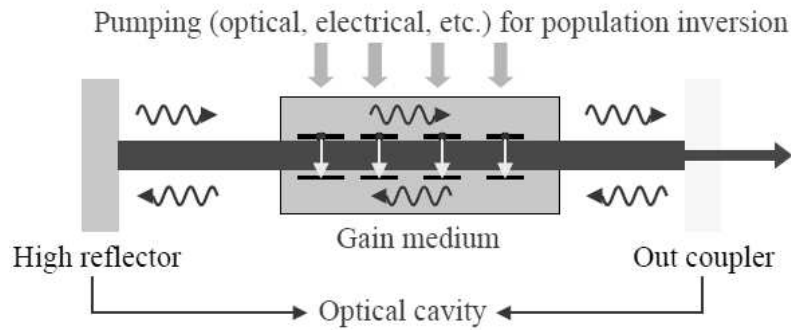
Figure 3-6 Laser resonator design [10]
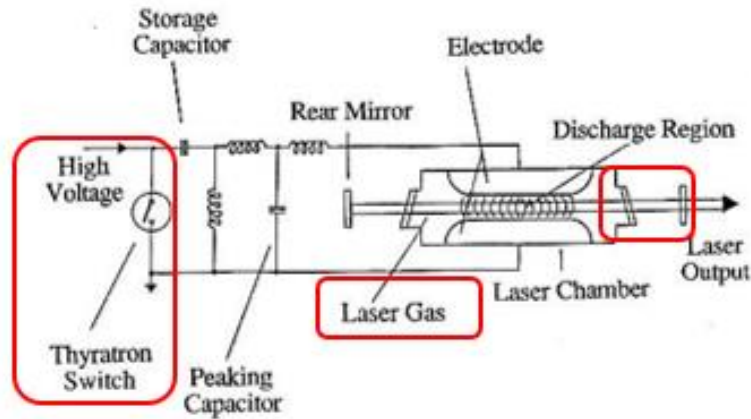
Figure 3-7 Gas laser operation [10] – red boxes added for clarity

Figure 3-7 shows key internal components in a gas laser that affect the energy of pulsed lasers. The thyratron is a high frequency, high voltage switch responsible for pulsing the laser and its dysfunction can deplete the energy output of pulsed lasers. The laser beam output aperture blocks part of the oblong electrode discharge and hence reduces output energy. Wear on the resonator optics i.e. the end coupler/high reflector and the out coupler/partial reflector can decrease laser energy. Passivation of electrodes by corrosive fluorine gas deplete laser output energy as well. Finally, the design of the resonator cavity affects the laser energy output. Since the latter two would involve a complete rebuild of the laser, the first four were targeted for repair and replacement.

3.6   Re-engineering the excimer laser to increase energy output

In order to increase laser energy, repairs/upgrades of internal laser components were carried out in two phases.

In phase 1, the thyratron was replaced. This led to the laser energy output increasing from the nJ range into the mJ range (Figure 3-8).

In phase 2, three repairs were made. First the circular laser aperture was removed. Since there already is another variable aperture installed downstream, there was no need to further block laser output energy at the source. Moreover, the aperture was found to be misaligned with the laser discharge as evidenced by the burn mark (Figure 3-9), and was hence blocking out a large portion of the beam.

Second, the worn output coupler was replaced. Finally, an internal solenoid gas valve was discovered to be leaking slightly and was preventing complete evacuation of the laser chamber during gas refills to replenish exhausted gas. Fluorine in the laser premix (which consists of Argon and Fluorine with Neon as the carrier gas) gets consumed as it reacts with materials inside the laser cavity including the electrodes and if the used gas isn't evacuated completely, laser energy output would decline. Hence, a manual external gas valve was installed (Figure 3-10).
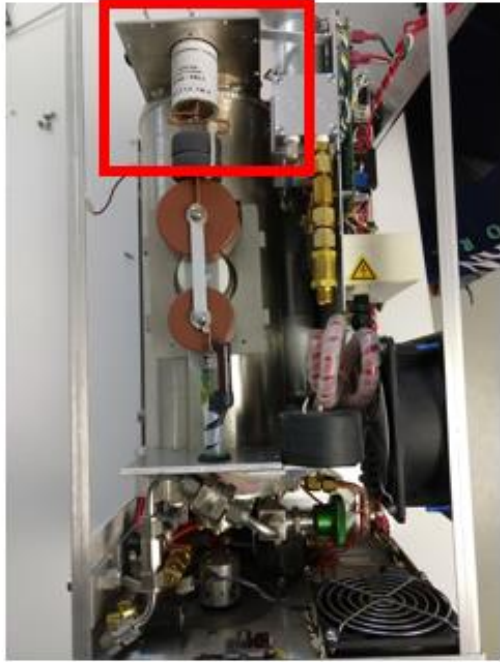
Figure 3-8 Laser thyratron replaced

Figure 3-9 Misaligned laser aperture removed

Figure 3-10 External manual valve installed

After phase 2, maximum power laser output energy of ~12mJ was achieved. The energy readings were averaged over 10k pulses at two different repetition rates 20Hz (the lowest operational pulse frequency) and 100Hz (the pulse frequency used for photoablation). The trend of increasing energy with each phase of repair, measured at all three locations as discussed previously, is depicted in Figure 3-11 and Figure 3-12. One of the outstanding characteristics of an ArF excimer laser is the high pulse-to-pulse consistency once warmed up to optimal operating temperature, and a standard deviation <0.5% in all cases was evidence of proper functionality being restored.
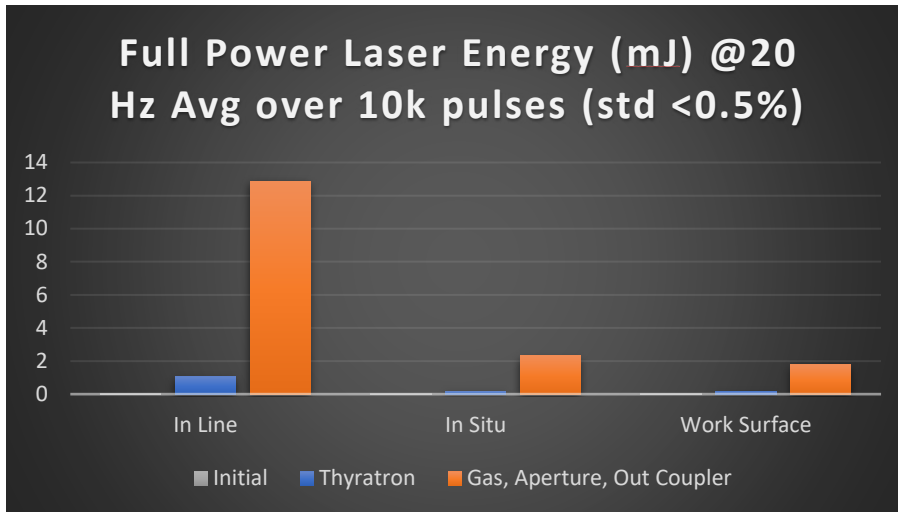
Figure 3-11 Laser output energy at 20Hz increase with the repair of internal components. Standard deviation in all cases < 0.5%
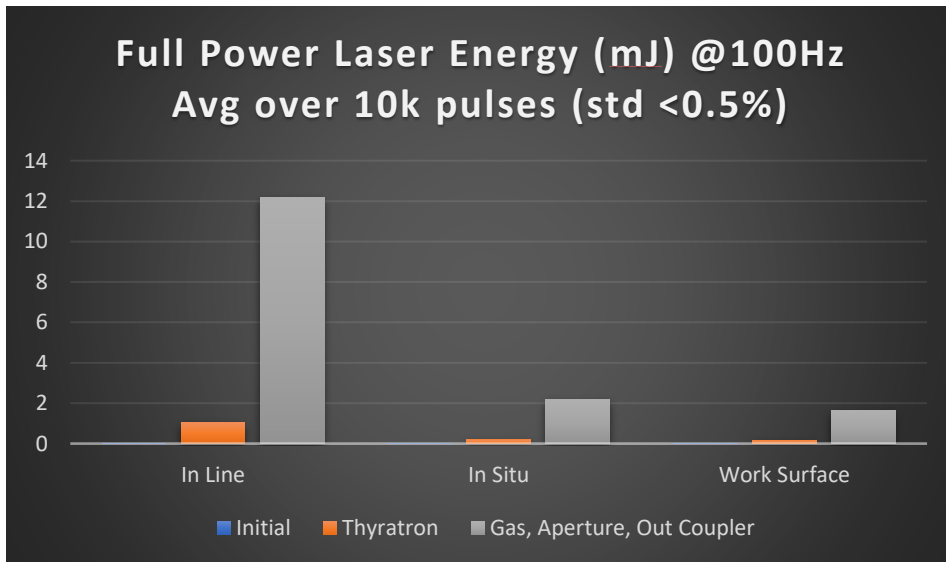
Figure 3-12 Laser output energy at 100Hz increase with the repair of internal components. Standard deviation in all cases < 0.5%

3.7 Configuring the laser control system

The DAQ card which interfaces the laser electronics with the computer needed to be replaced. As previously mentioned, the pin configurations on the laser control board were matched with the new DAQ card. The DAQ card needs to be hardwired into the computer motherboard. However, due to an obsolete PCI bus and form factor of the DAQ card, it required an external assembly with a secure connection to avoid a malfunction that could potentially be fatal for the computer or the laser.

To accomplish this, a case was designed and 3D printed using electrostatic discharge resistant thermoplastic to ensure tight contacts with connectors to the laser and computer (Figure 3-13). In order to avoid overheating and dust accumulation, the case was designed to be air-cooled (Figure 3-14). Also, support pillars inside the case were strategically designed so that the regions of the DAQ card, essentially a printed circuit board, that rested on the pillars did not contain any circuitry, only the support material (Figure 3-15). A 3D printer was built for the lab in the process and upgraded with enhanced firmware, novel bed leveling algorithms and increased bed adhesion, thereby addressing common issues with 3D printers (Figure 3-16).

Next, the DAQ card drivers were configured on the computer and the source code complied to match the DAQ pin assignments. The laser control software was integrated in LabView.

Finally, the laser parameters were calibrated (Figure 3-17). All parameter files were backed up for one-click repair for future users.

Note that the laser control system was configured prior to re-engineering the laser's internal components for increasing output energy, as monitoring of the laser output was only possible with computerized control. The energy section was included before this one for the sake of continuity from the previous section.
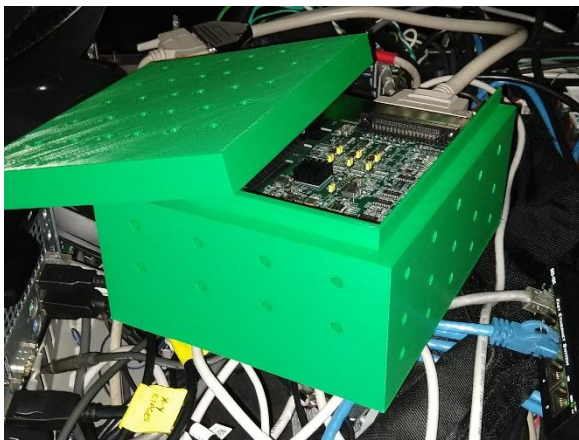
Figure 3-13 3D printed external laser DAQ card assembly
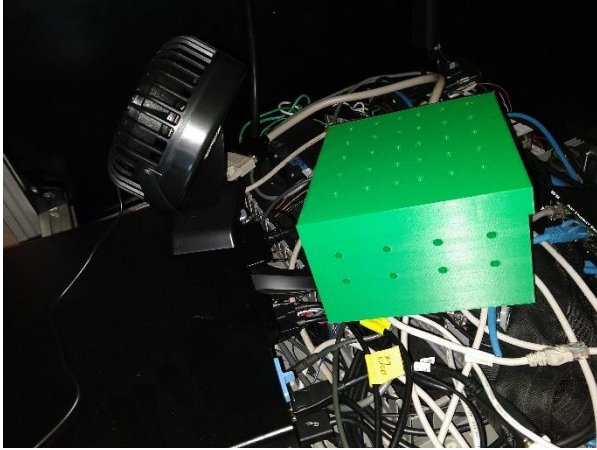
Figure 3-14 Air cooled 3D printed external laser DAQ card assembly

Figure 3-15 Strategically designed support pillars in 3D printed external laser DAQ card assembly
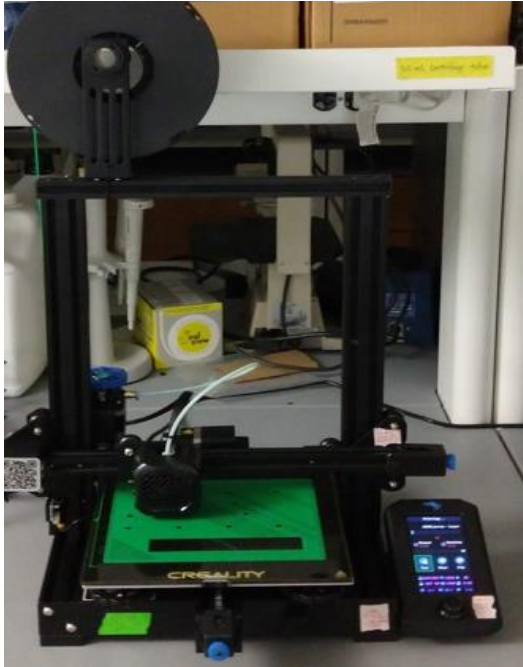
Figure 3-16 A 3D printer was built for the lab with enhanced firmware, novel bed leveling algorithms and increased bed adhesion

3.8 Re-engineering control systems for laser direct write components

Once the laser itself was fully functional and calibrated, the next stage involved re-engineering the control systems for the other laser direct write platform components.

Figure 3-17 Laser parameters calibrated

3.8.1 XY motion stages

The XY controllers for the ribbon and substrate stages were configured in a primary-secondary shift register type configuration for CAD/CAM capability. Four controllers, each controlling one axis of one stage were set up for the

primary/driver/master to interface with the computer via USB and synchronize with the other controllers via ethernet (Figure 3-18). Next, since the recent firmware was incompatible with the hardware, an old computer was used to flash and reset to factory default before programming in a compatible version of the controller firmware (Figure 3-22). Conflicts were reconciled to calibrate hardware, firmware, drivers and source code. Then, both axes of the ribbon and substrate stage were mapped with the controllers, giving the system true CAD/CAM functionality where codes could be written, compiled into G-code (machine language) and pre-programmed into the controllers for later execution synchronized with laser pulsing – for bioprinting and photoablation applications. All parameter files were backed up for one-click restoration for future users.

Figure 3-18 CAD/CAM X-Y substrate and ribbon stage motion controllers
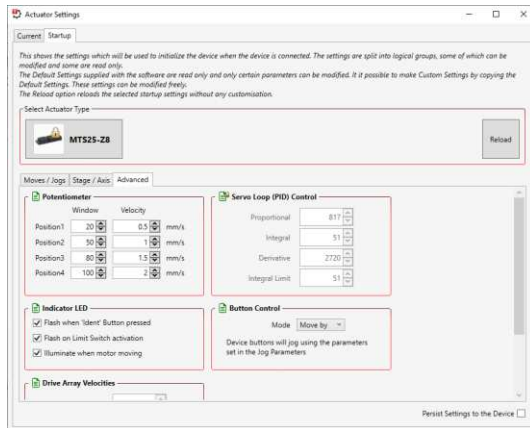
Figure 3-19 Z-stage actuator configuration and calibration

3.8.2 Z-stages

The substrate and objective Z-stage actuators were configured and calibrated (Figure 3-19). Since the Z-stage controller drivers often created software conflicts, a secondary computer was used to control motion in the z-direction.

3.8.3 Energy meters

The energy meters were also connected to the secondary computer that controls z-motion because of the propensity of their drivers to cause software conflicts. Since the *in situ* energy meter receives 10% of the laser energy from the beamsplitter and considering the inverse square attenuation in air, the

34

energy at the work surface was characterized using an external energy meter, its relationship with the *in situ* meter noted and configured the math channels such that the displayed energy represents the energy at the work surface and not simply the amount of laser energy that the *in situ* meter receives.

3.8.4 Variable aperture

The piezoelectric controller for the motorized iris was configured and calibrated (Figure 3-20). Since there were legacy issues due to old hardware, it could not be connected to either the primary or the secondary computer. Hence, it was connected to an older computer that controls the microscope located next to the laser direct write instrument as a temporary workaround until a new piezoelectric controller compatible with modern computer hardware can be purchased and configured.
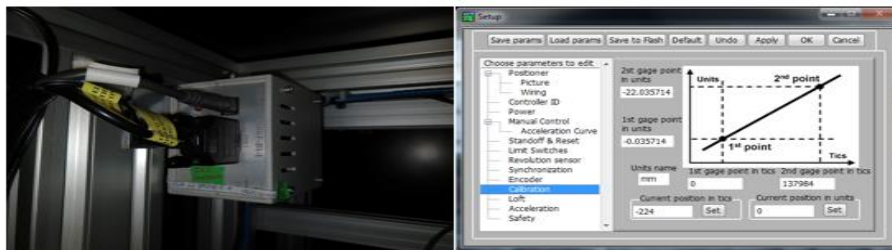
Figure 3-20 Configuration and calibration of the motorized iris piezoelectric controller

3.8.5 Side-view camera

Finally, a side-view microscopic camera was installed to ensure proximity of the print ribbon and receiving substrate for printing cell patterns with high fidelity in the jetting regime by controlling the number of cells printed using the laser spot size dictated by the computer-driven variable aperture. A 3D-printed screwed holder was designed to affix it inside the printing chamber (Figure 3-21). This adds to the already unique capability of real-time imaging that laser direct write system offers during bioprinting and photoablation. To avoid software conflict between the cameras, the side-view camera is connected to the primary computer via USB as the *in situ* telescopic camera is connected via ethernet.
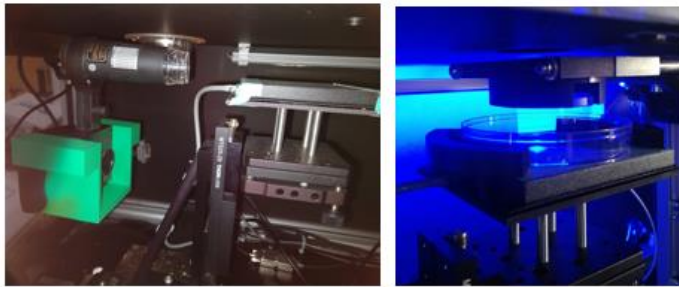
Figure 3-21 Side view camera to ensure proximity between print ribbon and receiving substrate

3.8.6 Actual wiring, testing & backup
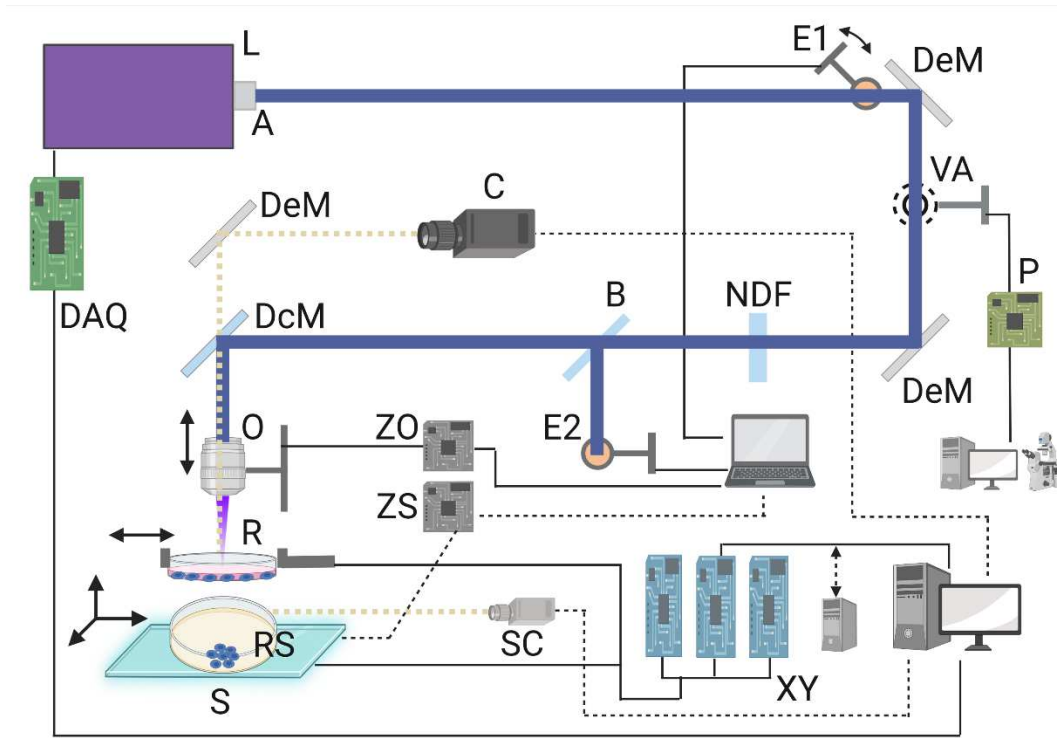
Figure 3-22 Laser direct write system – actual wiring

Lastly, the actual wiring and control of the system in its current configuration is clarified in Figure 3-22 and the actual setup depicted in Figure 3-23. Driver configurations, source codes and calibration parameters for all components were backed up for easy restoration. Moreover, this next-generation laser direct write system was "stress tested" by disconnecting cables, causing abrupt loss

of power to a component and corruption of calibration parameters – which would have caused a plethora of lasting issues in the previous generation system – and robust, reliable functionality was confirmed.

Figure 3-23 Convenient placement of the two additional computers required to control the Z-stages and energy meters (laptop) and the variable aperture (microscope computer)

4 Bioprinting Heterocellular Breast Cancer-Stromal Arrays

4.1 Introduction

The most enriched cell types in the breast tumor microenvironment are breast cancer cells, cancer-associated fibroblasts and tumor-associated macrophages and both the stromal and immune components play a key role in breast cancer growth, invasion and metastasis [11]. In order to build physiologically relevant *in vitro* models of the breast tumor microenvironment and recapitulate metastatic cell dynamics, it is not only important to incorporate multiple cell types but also pattern them in appropriate geometries to facilitate cell-cell interactions. Laser direct write bioprinting is a high resolution, gentle and reproducible cell printing technique that could serve as a valuable tool to fabricate heterocellular breast tumor microenvironments *in vitro* as it is a cell type independent technique conducive to viably patterning cells with high densities to facilitate juxtacrine signaling [3] [4]. Herein, laser direct write based cell printing methods were developed to print heterocellular arrays of human triple negative breast cancer cells and human fibroblasts with both homotypic and heterotypic spots.

4.2 Hypothesis

Laser direct write bioprinting is conducive to viably printing human breast cancer and stromal cells individually and simultaneously in user-defined geometries.

4.3 Results And Discussion

A novel optimized protocol for laser direct write bioprinting for viably patterning cells in a scaffold-free and contactless manner was successfully developed and the workflow was subsequently adapted for printing homotypic and heterotypic heterocellular arrays.

4.3.1 Laser direct cell printing protocol: General framework

The laser direct write cell printing protocol can be divided into six distinct stages, most of which need to be carried out simultaneously and hence are temporally overlapping. These stages are as follows: (a) Pre-transfer cell culture; (b) Substrate preparation; (c) Laser direct write system preparation; (d) Ribbon preparation; (e) Laser direct write printing process; and (f) Post-transfer cell culture. Figure 4-1 depicts the temporal interaction of these stages.
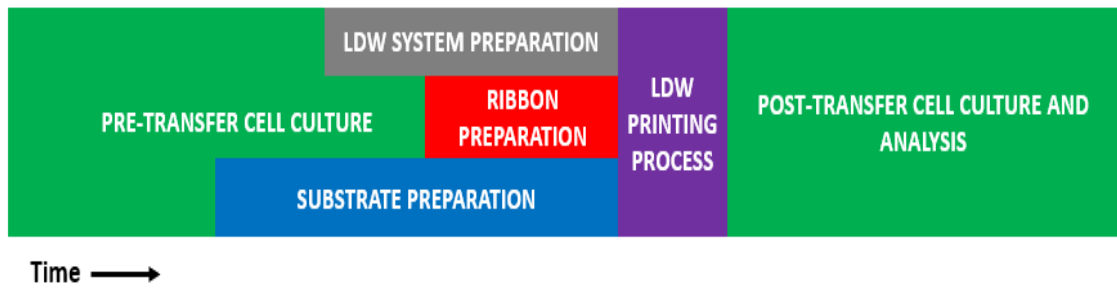
Figure 4-1 The temporal interplay of overlapping stages in the laser direct write bioprinting protocol. Preparation of the receiving substrate and the laser direct write system has to be done in advance of ribbon fabrication and the printing session. Pre- and post-transfer cell culture methods depend upon the cell types being printed.

Pre-transfer cell culture:

The cells to be printed are generally cultured according to standardized culture protocols established previously, unless further optimization is required to maximize cell viability in preparation for printing. Standard mammalian cell culture involves cells cultured at appropriate densities submerged in media supplemented with 10% serum at 37C with 5% CO_2 and 95% relative humidity. If further optimization is required, parameters such as the culturing density, and media formulation as well as the procedures for cell detachment and media replenishment are systematically modified and cell viability tested.

Substrate preparation:

The objectives of preparing the receiving substrate dish are twofold. First, cell attachment to the substrate post-printing needs to be maximized in order to preserve the fidelity of the printed pattern. Second, the shear stress on the cells as a result of the droplet landing on a hard plastic surface needs to be minimized.

Although tissue culture dishes are plasma treated for enabling cell attachment, adherent mammalian cells can normally take a few hours to overnight to form secure focal adhesions that are strong enough to resist the shear stress that ensues as a result of pipetting in of media. Once the cells are printed using laser direct write, it is important to gently add media (in a dropwise manner to minimize shear) as soon as possible without disrupting the printed pattern – both to nourish the cells to preserve maximal viability as well as to shorten the bioprinting workflow. Clearly, waiting for hours is not feasible and the cell culture surface needs to be further treated with an attachment factor that would work for a variety of cell types.

Hence, the receiving substrate was coated with poly-L-lysine prior to printing cells. Poly-L-Lysine (PLL) is a nonspecific attachment factor that readily adsorbs to tissue culture polystyrene and increases the number of positively charged cell binding sites. This promotes cell adhesion by enhancing electrostatic interaction between negatively charged ions of the cell membrane

and the tissue culture surface. High molecular weight PLL (>70kDa) was used not only because it would offer more attachment sites per molecule but also because lower molecular weight PLL can be toxic to certain cells.

While the standard protocol for coating substrates with PLL involves leaving the dish with PLL solution at room temperature for 5 minutes before pipetting out and drying for 2 hours, it was found to be inadequate. Hence, 0.1mg/mL of PLL solution was incubated at 37C for 2 hours to maximize absorption before pipetting the solution out and leaving the dish to partly covered under sterile conditions overnight. Due to an overnight step, the PLL treatment of the receiving substrate dish needs to carried out in advance of the day that cell printing is planned.

In order to minimize the shear stress on the cells during droplet transfer onto a hard surface at high speed, a softer coating of an adequate thickness is necessary. This coating should not interfere with cell adhesion and ideally enhance it, should not alter cell functionality post-printing and should not add complex synthesis steps to the printing protocol.

Gelatin is an inexpensive hydrogel that satisfies all of the aforementioned characteristics and was hence chosen. It contains the arginine-glycine-aspartic acid (RGD) sequence, which promotes stable cell attachment via integrin mediation. Gelatin hydrogel has a melting point lower than 37C and the hydrogel layer will subsequently dissolve when incubated, bringing the

patterned cells directly into contact with the PLL-treated surface. Further, synthesizing the hydrogel simply involves dissolving in water at 60C.

Prior to cell printing, the PLL-treated substrate was spin-coated with a 100um thick layer of 10% gelatin solution in basal cell culture media (most commonly DMEM but dependent upon cell type) at 400rpm. The dish was then refrigerated for 4 minutes to allow the gelatin to solidify. Next, cold basal media (at 4C) was rinsed across the coated gelatin and fully aspirated, as any wetness would cause the printed cells to float away. The presence of basal media in the hydrogel increases the nutrient supply to the printed cells, which must survive and attach securely enough before any additional media can be dispensed. Finally, the treated and coated substate dish was incubated at 37C for at least 30 minutes before printing to ensure an optimal receiving surface.

Laser direct write system preparation:

Preparing the laser

In order to be able to print cells using matrix assisted pulsed laser evaporation, laser fluence must be tightly controlled from pulse-to-pulse at a value to match the jetting threshold for of 20% gelatin ($0.4J/cm^2$) to ensure a columnar jet during forward transfer, which requires the laser output to be optimized and the beam profile characterized.

As discussed previously, the ArF "excimer" (technically exciplex) laser has been re-engineered to increase its maximum output energy to more than 10mJ. Since the gaseous laser gain medium in its activated state consists of excited Ar-F excited complexes, operating the laser results in deterioration of laser output over time as the fluorine gas is consumed by passivation of the electrodes and reactions with other materials inside the laser chamber. Hence, to maintain pulse-to-pulse consistency of laser energy output, fresh gas refills were performed before each printing session. Since our laser is a transversely excited atmospheric (TEA) laser designed to operate at very high atmospheric pressures, the laser gas pressure was optimally set at 3950 Torr (or 5.2 atm). In order to conserve laser gas, partial refills were performed if the output laser energy whenever possible.

Lasers need to warm up before they can output consistent pulse-to-pulse power. The warming up procedure involves turning on the heating element and firing the laser at multiple repetition rates (including the maximum rate that the laser is capable of) over a large number of pulses at full power until the electrode and gas temperature reach their optimum values. In the case of our ArF exciplex laser, setting the heating element to 32C and dialing up the discharge voltage to its maximum of 15kV, and subsequently firing 2000 pulses at 20Hz and 5000 pulses at 100Hz – was sufficient to reach optimal operating temperatures and achieve high pulse-to-pulse consistency in terms of output

energy. Once a gas refill was complete, the laser was warmed up before measuring the laser energy. If the energy was insufficient, further gas refills were performed and the energy checked.

The laser direct write system is equipped with components to regulate the laser beam profile – such as a variable aperture and a neutral density filter. The motorized variable aperture or iris which modifies the laser beam profile and alters the laser spot size incident on the print ribbon. Since laser fluence is the energy density defined as energy per unit area, altering the laser spot size changes the fluence at the print surface even if laser energy is unchanged. Moreover, in the columnar jetting regime, since the transferred cell droplet or voxel closely resembles the dimensions of the focused incident laser spot, the iris, along with the cell density on the ribbon, controls the number of cells that are printed. Also, as the energy distribution profile of the laser beam incident on the work surface has been shown to be near-Gaussian (Figure 4-2), blocking a part of the laser beam concentrically does reduce the laser energy reaching the print ribbon, especially at smaller spot sizes, and thus may require compensation by adjusting of laser discharge voltage. This adjustment needs to be made after the desired cell spot sizes have been determined but before commencing the printing process. The laser spot size incident on the work surface is characterized by coating a glass slide with a thin layer of permanent marker ink, focusing the laser beam on the substrate, pulsing the laser until the

ink is ablated and then measuring the size of the ablated spot under a microscope (Figure 4-3). The focused spot size measurements typically have a tolerance of 3%.
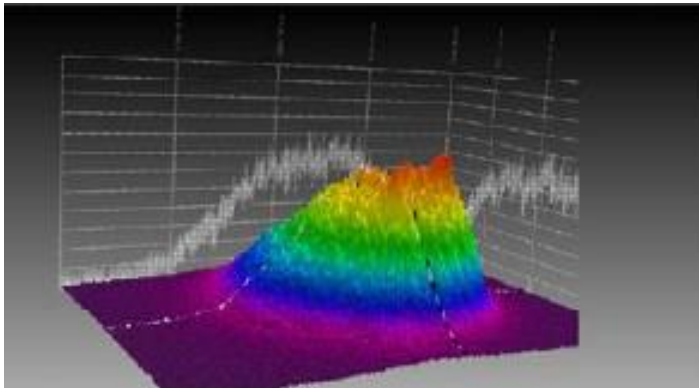
Figure 4-2 Laser beam energy distribution profile over 1000 pulses at full laser power (discharge voltage 15kV)
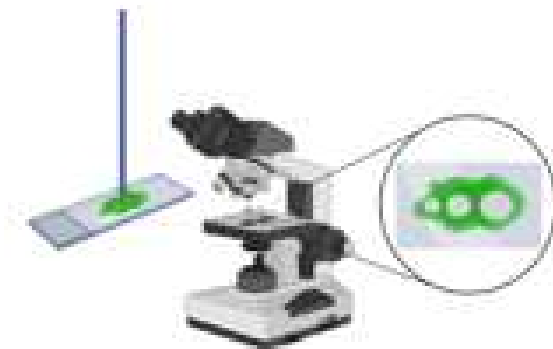
Figure 4-3 Characterization of the laser spot size

Figure 4-4 shows a sample characteristic curve of the variation of the incident laser spot size when the laser beam is focused on the work surface. This was measured by positioning an external energy meter on the substrate stage aligned with the laser beam path and connecting it to an external computer for readout. Evidently, the focused spot size has a nonlinear variation with respect to the preprogrammed aperture configurations of the motorized iris. Figure 4-5 depicts the variation in fluence at maximum laser power with respect to the preprogrammed iris apertures. The nonlinearity as well as shifting direct and inverse relationship of fluence as the aperture size is varied, is due to the laser beam energy distribution profile being nearly-Gaussian and the outer part of the spatial energy distribution being blocked by the iris.
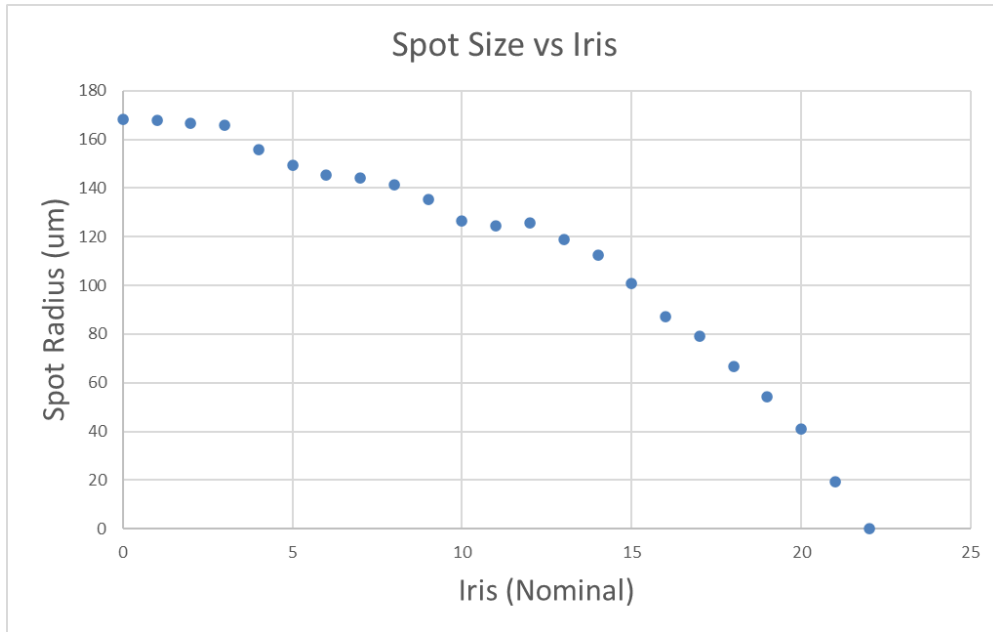
Figure 4-4 Sample laser spot size characteristic curve with the current setup. The motorized iris has predetermined nominal values with 0 being fully open and 22 being fully closed. Tolerance = 3%
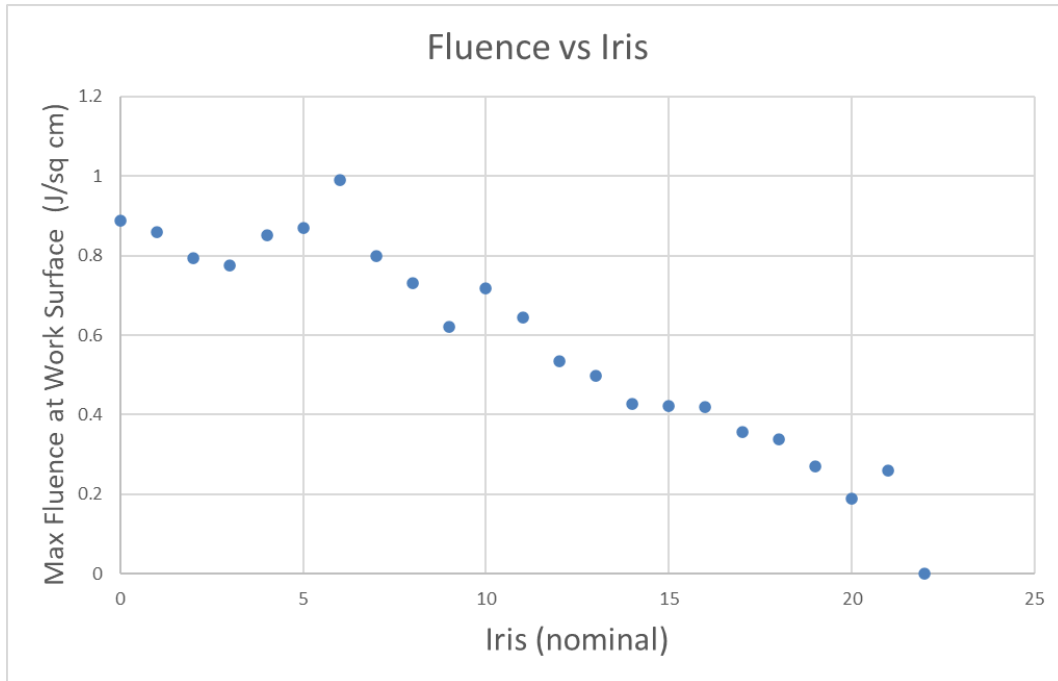
Figure 4-5 Sample fluence characteristic curve at maximum laser power with the current setup. The motorized iris has predetermined nominal values with 0 being fully open and 22 being fully closed.

The sample fluence and spot size characteristic curve bring up a couple of interesting points. First, given the $0.4J/cm^2$ jetting threshold of 20% gelatin, the system is currently limited to printing cell spots of at least 130um in diameter. For larger spots, simply lowering the laser discharge voltage suffices to reduce the incident fluence to slightly above threshold. Since the system is operating with an aged albeit re-engineered laser, installing a newer laser or upgrading the more expensive components of the current laser such as the electrodes and resonator, or augmenting the chamber with additional components such as

a powerful external vacuum pump for complete evacuation of exhausted gas and a cryoprocessor to eliminate ablated metal particles inside the cavity, will increase the laser energy and push the maximum fluence at smaller spot sizes above the gelatin jetting threshold. This, in turn, will allow for printing of smaller cell voxels and consequently, single cells.

Second, for finer control of laser fluence at the work surface, additional neutral density filters can be used in the beam path. Neutral density filters (NDF) are absorptive optics with a defined transmittance given a wavelength of radiation (such as 10%, 25% or 32%). At spot sizes where the incident fluence on the work surface is much higher than the gelatin jetting threshold, using an NDF would allow the user to coarsely control the laser discharge voltage yet finely tune the laser fluence at the cell-loaded hydrogel - ribbon interface, thereby optimizing the forward transfer.
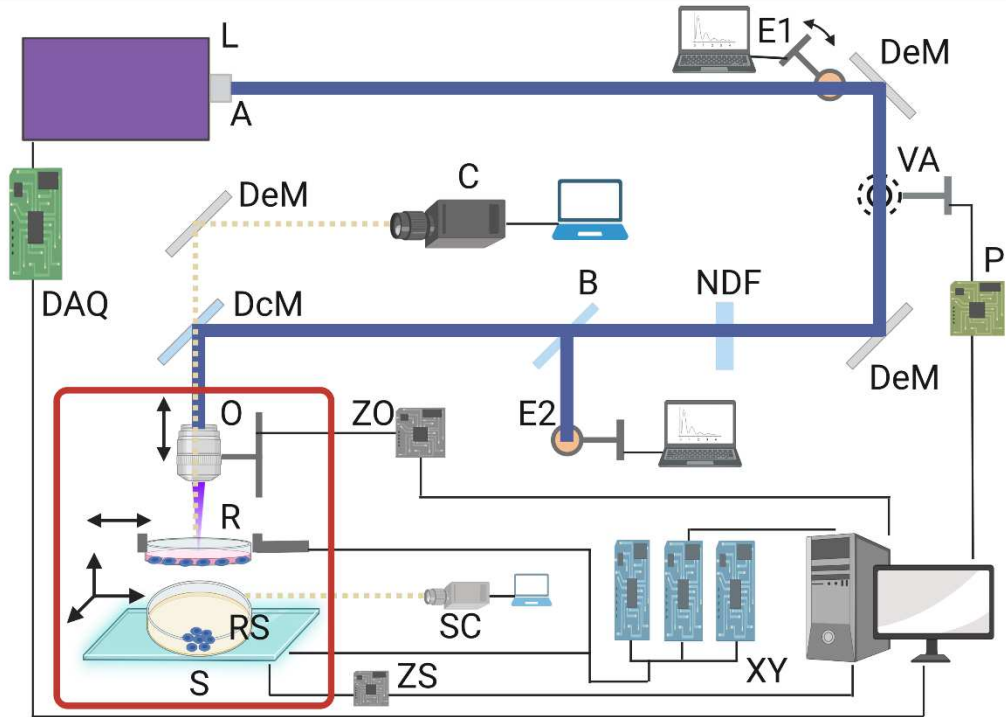
Figure 4-6 Schematic of the laser direct writing cell printing setup [RS: receiving substrate; R: ribbon]

By following the abovementioned steps, pulse-to-pulse energy variability with a tolerance (defined to be the standard deviation as a percentage of mean) of <0.3% was achieved for the concerned cell droplet dimensions.

Finally, the laser fluence was actively monitored throughout the printing process. Since the *in situ* energy meter receives 10% of the laser energy from the beamsplitter and the laser beam has to travel a further 50cm between the beamsplitter and the work surface (as depicted in Figure 4-6), there exists a defined mathematical relationship between the respective readings. Taking

simultaneous observations for both energy meters at various spot sizes allowed for the determination of the scaling factor, which was then applied to the *in situ* energy meter readings during the printing process to calculate the fluence at the ribbon interface.

Preparing the translational stage

Once the laser output was optimized, characterized and being actively monitored, the XY CAD/CAM substrate stage was programmed to sequentially move to locations where cells needed to be printed. The motion control code was composed, complied into G-code and programmed into the controllers. This allows for the user to focus their attention on choosing the cells to print on the ribbon during the printing session.

Rectangular arrays of cell spots were programmed to be patterned on the substrate. While the CAD/CAM functionality allows for patterning cells in any given geometry, even a simple rectangular array with cells printed at defined locations serves as proof of principle for the ability to localize cells on the substrate or groups of cells with high fidelity.

Ribbon preparation:

The print ribbon is a quartz disc, which is transparent to 193nm UV-C radiation and is coated on the underside with a sacrificial layer of hydrogel and then overlaid with a layer of cell suspension prior to mounting in the bioprinter. When the laser beam is focused on the quartz-hydrogel interface, it causes the water in the hydrogel to superheat and cavitate to create a vapor pocket, which rapidly collapses to produce a short lived shockwave that propels the droplet towards the substrate. The shockwave significantly attenuates before reaching the cell suspension layer, and hence minimizes shear stress on the cells. Also, since according to Beer-Lambert's Law the penetration depth of UV-C radiation in a sufficiently concentrated hydrogel is <<10um as UV-C radiation is primarily absorbed by macromolecules). Hence, as long as the hydrogel layer of a thickness 10um or greater is present, UV-C radiation never comes into direct contact with the cells. This is important to avoid phototoxicity, as DNA strongly absorbs UV-C radiation and denatures in response to it. Moreover, as the droplet with cells is being formed, it gets coated with a thin layer of hydrogel, which serves to further cushion the cells as they land on the (hydrogel coated) substrate. Minimizing shear stress on the stress during droplet ejection and landing combined with preventing UV-C phototoxicity ensures that matrix assisted pulsed laser evaporation bioprinting is extremely gentle on the cells and results in high post-printing cell viability. [4] [3]

The criteria for sacrificial hydrogel of choice are similar to the hydrogel coating on the substrate with a couple of additional requirements. It should not interfere with cell adhesion to substrate (and ideally enhance it), should not add a complex synthesis step to an already multi-step protocol and should be concentrated enough to not only strongly absorb UV-C radiation but also to be able to provide cushioning upon the droplet landing.

Gelatin was again considered the hydrogel of choice but used at a higher concentration of 20% on the ribbon. The ribbon was sterilized and the side to be coated was warmed to ensure an even coating of gelatin. It was then spin coated with a 50um thick layer of 20% gelatin at 2000rpm.

Next, the gelatin coated ribbon was seeded with cell suspension and dried sufficiently to ensure that no liquid drips off or pools when the ribbon is inverted, which would interfere with the forward transfer. Steps were also taken to ensure the gelatin layer was soft enough to be conducive to laser induced forward transfer as well as for partially embedding cells to provide protection from shear stress but viscous enough to not flow with the motion of the ribbon stage. Upon optimization, the following protocol was developed.
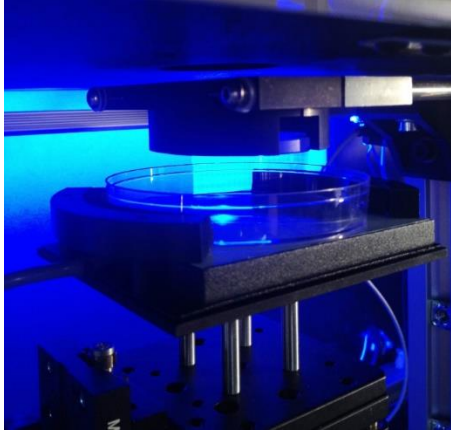
Figure 4-7 Print ribbon inverted and mounted on the CAD/CAM ribbon stage, aligned with the receiving substrate

The gelatin coated ribbon was incubated at 37C for at least 3 minutes prior to seeding cells. The cells were detached from their flasks using standardized procedures, dissociated into single-cell suspension, resuspended at a density of 500k-1M cells/mL and seeded onto the ribbon. Then, the seeded ribbon was incubated for at least 7 minutes to allow cells to embed into the gelatin. Next, the ribbon was tilted at an acute angle in all directions and excess media was dabbed off with a lint-free disposable wipe. Subsequently, the ribbon was incubated at room temperature in a sterile hood for precisely 3-4 minutes to partially resolidify the gelatin and make it sufficiently viscous. Finally, the ribbon was inverted and mounted on the ribbon stage inside the printing chamber, aligning it with the receiving substrate (Figure 4-7).

Printing:

Once the substrate and ribbon were fabricated and mounted inside the printing chamber, they were aligned such that the ribbon was positioned above the location of the first spot of the rectangular array programmed into the controller. The laser beam was focused on the interface between the ribbon and gelatin coating by moving the 5x objective in the Z-direction. This was accomplished by focusing the *in situ* telescopic camera image at the interface. The camera as well as its light source are optically aligned with the laser beam and are focused by the same objective lens (Figure 4-6). The dichroic mirror is a long pass reflector and transmits longer wavelengths while reflecting shorter wavelengths. It reflects the laser beam down into the objective but allows visible light to pass through into the camera generating an on-screen video feed. Hence, when the ribbon-hydrogel interface is focused on the screen with the cells visible (Figure 4-8), it indicates that the laser beam is focused on the same plane as well.
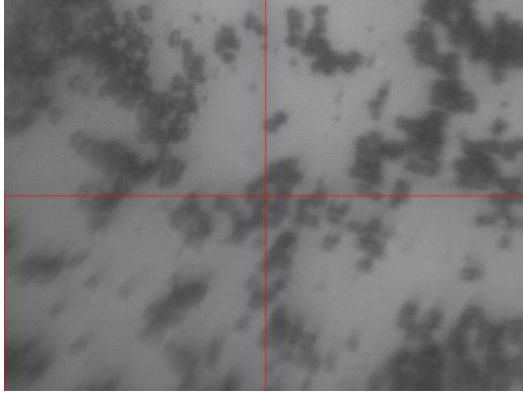
Figure 4-8 Real time camera image when laser is focused on the ribbon-hydrogel interface, with the seeded cells visible at magnification 5x. Cross hairs indicate the point where the laser beam would be centered as it is fired to print the cells.
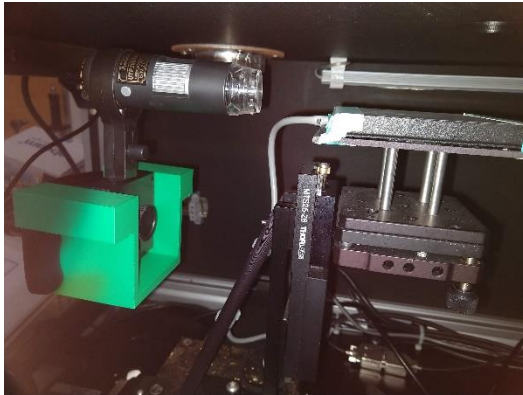
Figure 4-9 Side view microscopic camera for assessing the Z distance between ribbon and substrate

Now, in order to ensure a columnar jet, which is necessary for maintaining the fidelity of the printed cell spots closely matching the focused spot size of the laser beam, the gap between the lowest surface of the ribbon and the

58

uppermost surface of the receiving substrate needs to be around 100um or less. A larger gap leads to the jet dispersing into a plume and disrupting the intended cell pattern, as well as killing most of the cells. Hence, the substrate and the ribbon need to be brought as close as possible to each other without touching (which would simply stamp the cells on the ribbon rather than patterning them in the preprogrammed array). This was accomplished by utilizing the side view microscopic camera (Figure 4-9) and incrementally raising the substrate stage using the motorized the Z-stage, initially in jog steps of 500um and then in jog steps of 50um as the substrate approaches the ribbon.
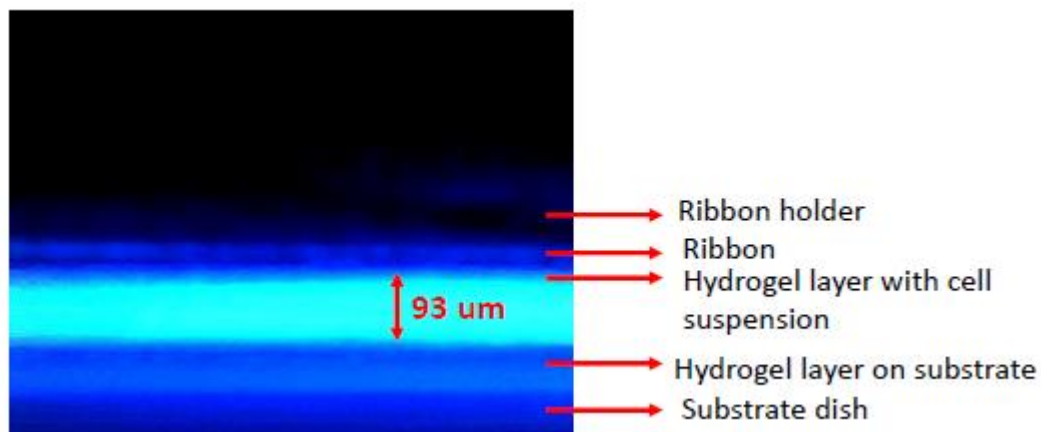
Figure 4-10 Side view microscopic camera image taken at 10x depicting a gap < 100um between the ribbon and substrate in preparation for printing

Figure 4-10 depicts an example side view at 10x magnification of the ribbon and substrate positioned as close as possible to each other without their surfaces touching in anticipation of a cell printing session. The image, taken against a blue backlight allowed for visual distinction between the opaque ribbon holder, a small part of the transparent ribbon beyond the ribbon holder, the thin hydrogel layer on the ribbon holder with the embedded cells, the hydrogel coating on the substrate and the substrate dish bottom. A measured distance between the hydrogel layers of the ribbon and the substrate of less than 100um was found to be highly indicative of high probability of a successful forward transfer.

Once the ribbon and substrate are close together and the ribbon is positioned over the first spot of the preprogrammed array, the cells to be printed were selected using the on-screen video feed of the ribbon generated by the *in situ* telescopic camera (Figure 4-8). The ribbon was moved in 10-50um increments in the XY plane until a desired spot was reached. The spot was selected based upon the objective of the print. If a high cell density in the printed pattern was required, an area of high cell density on the ribbon was selected, and vice versa. Regions on the ribbon that showed 3D clumping of cells were avoided, as attempting to print those regions would not only lead to less control over the number of cells transferred but also impede cell viability and adhesion if the cell aggregate was broken up by shear during transfer or landing. It is important to

note that laser direct write bioprinting is adaptable for printing 3D cell aggregates and organoids using an appropriately large spot size and a suitably prepared receiving substrate. This will be discussed briefly in a following chapter. However, when using a small laser spot size and a substrate optimized for enhancing adhesion of dissociated cells, it is best to target dissociated cells on the ribbon for successful prints. Other regions on the ribbon that were avoided include those that appeared "excessively wet", where there appeared to be flow of liquid as the ribbon was translated, and those that appeared "excessively dry", where the hydrogel started to look opaque. Regions that are too wet or too dry prevent forward transfer. In addition, excessively wet regions lead to air bubble formation in the hydrogel which decreases cell viability in neighboring areas and excessively dry regions lead to dehydration of cells, which even if they could be printed would not be viable. Once an appropriate spot was selected, the laser pulse was fired to accomplish forward transfer.

Upon successfully printing a cell spot – this can be visually observed on the real time camera image in multiple ways e.g. the complete disappearance of targeted cells from the ribbon, a shadow appearing while focused on the ribbon plane, or by briefly focusing the objective on the substrate place (the latter two are enabled by the substrate stage being equipped with a backlight as depicted in Figure 4-6) – the substrate stage was translated to the next spot in the preprogrammed array, an suitable spot was located on the ribbon and the laser

fired. This was repeated until the array was complete. Finally, the substrate stage was lowered, the lid immediately replaced on the dish and the dish transferred into the cell culture incubator.

Post-transfer cell culture:

Post-transfer cell culture protocols for printed arrays were developed to optimize cell adhesion and viability. As soon as the printed cells were transferred into the incubator, the gelatin coating on the substrate (as well as the encapsulating gelatin from the ribbon) would begin to melt, and the printed cells would sink onto substrate dish surface. Since this surface was treated with high molecular weight PLL to promote adhesion, the negatively charged ions on the cell membrane will electrostatically interact would the positively charged cell binding sites on the substrate and the cells would start attaching, and forming nascent focal adhesions [12]. The RGD peptide sequence present in the surrounding gelatin would further promote focal adhesions via integrin mediation.

Only once the cells have attached sufficiently securely to the substrate, will dispensing the media avoid disrupting the printed pattern due to shear stress. In the meantime, the residual media present in the gelatin layers (having been used as a solvent for the substrate coating and as part of the cell suspension

62

seeded on the ribbon) would nourish the cells with nutrients to keep them viable.

A post-print incubation time of 15 minutes was found to be sufficient for most cell types to attach to PLL treated surfaces in the presence of gelatin. Subsequently, warmed full growth media was gently pipetted in a dropwise manner and the dish carefully placed back in the incubator to culture undisturbed overnight. Finally, on the following day, the printed cell arrays were rinsed to remove any debris and unattached cells, imaged and characterized.

4.3.2 Adaptation for printing breast cancer cells and fibroblasts

The general framework for laser direct write bioprinting was established, as detailed in the previous section. While this technique is cell type independent, the varying characteristics of cell types often require modifications of certain aspects of the generalized protocol.

Here, the aimed was to print human triple negative breast cancer (TNBC) cells and fibroblasts in heterocellular arrays. Since these cell types tend to be relatively robust *in vitro*, only one modification was necessary. During the pre-transfer culture and ribbon fabrication stages, cancer cells demonstrated greater viability when detached using a dilute solution of a calcium/magnesium chelating agent (2.9mM EDTA) while fibroblasts displayed higher viability when

a proteolytic agent (trypsin) was used in addition to the chelating agent. This was understandable because fibroblasts have a propensity to secrete and lay down large amounts of collagen-rich ECM, and a chelating agent alone is insufficient to cleave the structural proteins. Using a chelating agent alone results in complete reliance on mechanical agitation for fragmentation of the ECM with embedded cells, which leads to lower viability. For cells that do not secrete large quantities of ECM, using a calcium/magnesium chelating agent – which sequesters the divalent cations, thereby inhibiting integrin-ligand binding – is a gentler method which improves cell viability.

4.3.3 Adaptation for printing heterocellular arrays

Since the generalized protocol involved printing a single-cell type in a homotypic array, further modifications were essential to be able to print multiple cell types within the same array. The capability to print heterocellular arrays is desirable because it provides us with a platform to study cell-cell interactions. For instance, breast cancer cells interact with the surrounding stromal cells in the tumor microenvironment and are known to reprogram them into cancer associated fibroblasts, which in turn have been shown to enhance tumor growth and metastasis [13]. Fabricating heterocellular arrays would allow for

investigation of such interactions and the resultant cellular dynamics at high resolution and throughput.
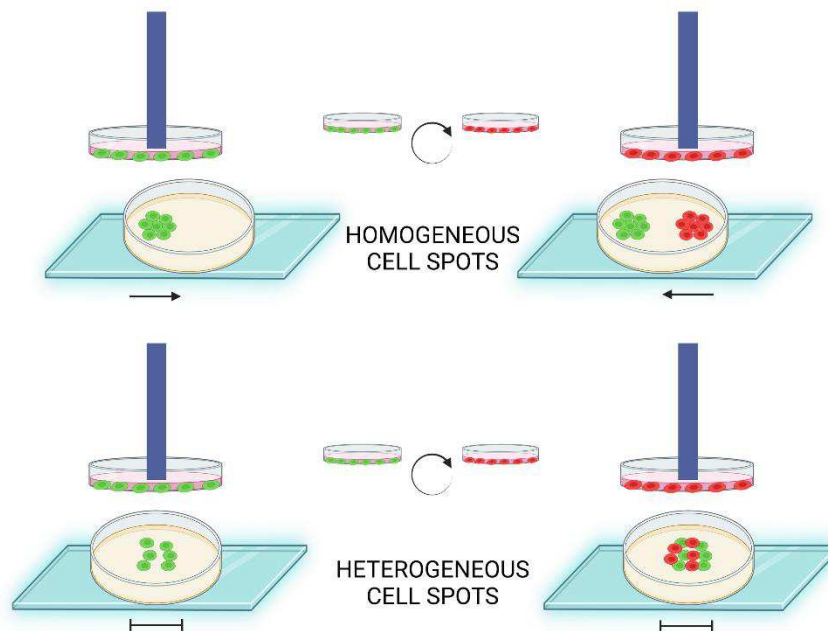
Figure 4-11 Laser direct write printing of heterocellular arrays with homotypic and heterotypic spots. Multiple print ribbons were fabricated simultaneously and switched in the midst of the printing process while the substrate remained fixed.

The generalized protocol is amenable to be adapted to print heterocellular arrays using fluorescently labeled cells. Ideally, such cells would be transfected with a fluorescent reporter gene, which would enable tracking them over several generations of daughter cells but simply labeling cells with a fluorescent dye prior to printing suffices for shorter-term assays spanning fewer cell

65

divisions. Since the UV laser radiation never comes directly into contact with the cells, photobleaching of the fluorophores is not a concern.

For printing multiple cell types – in this case human breast cancer cells and fibroblasts labeled with – multiple print ribbons were fabricated simultaneously, each seeded with one cell type, and switched mid-print without disturbing the substrate. Heterocellular arrays to study cell-cell interactions can comprise homotypic or heterotypic cell spots. Homotypic cell spots entail alternating spots of breast cancer cells and fibroblasts whereas heterotypic cell spot entail a co-localization of breast cancer cells and fibroblasts within the same spot.

Homotypic heterocellular arrays:

Printing heterocellular arrays with homotypic spots involved generating a motion control code that translated the substrate to all the spots of one cell type first and then repeated the motion sequence for the other cell types to be printed, based on their respective desired locations within the array. In the present example, human breast cancer cells and fibroblasts were patterned in the same array, with an equal number of spots of each cell type. Once the motion control code was programmed into the controller, the ribbon with one cell type was loaded, the laser beam was focused on the ribbon interface, the substrate was raised to be within 100um of the ribbon without touching and the

spots were printed by choosing the appropriate regions on the ribbon. Once all the spots of the first cell type were printed, the substrate stage was first translated in the XY plane to the next array spot (for the other cell type) and then lowered (Z direction), the ribbon stage was translated away from the substrate in the X direction and the ribbon was switched. A 3D printed clip was used to keep the substrate dish immobilized on the substrate stage throughout this process. Once the new ribbon was loaded, the ribbon stage was repositioned back in the path of the laser beam and aligned with the substrate and the substrate stage was gradually raised to be within 100um of the ribbon. Next, the laser beam was refocused on the new ribbon, an appropriate region chosen and cells printed in the designated spots of the array by executing the motion control sequence for the substrate. This procedure is illustrated in Figure 4-11.

While changing the ribbon mid-print adds a manual step to the workflow as well as increases the time that the cells spend outside the incubator suspended on the ribbon and having multiple ribbons simultaneously drying out limits the size of arrays that can be printed with this protocol, fabricating multiple ribbons each seeded with one cell type was found to be advantageous compared with trying to seed multiple cell types on one print ribbon. Since the *in situ* telescopic camera is only capable of brightfield imaging, it is not possible to distinguish different cell types on the ribbon. Attempting to seed multiple cell types on

67

different regions of the same ribbon can not only lead to confusion during the printing process but the ribbon drying and mounting procedures also increase the chance of cell types mixing on the ribbon due to coalescing of the suspensions. Moreover, if multiple cell types are seeded on ribbon regions small enough to fully mitigate the coalescing issue, it limits the selection of areas that can be targeted for successful prints of viable cells. Hence, separate ribbons each with one cell type were used.

In order to ameliorate this drawback, an automated ribbon changing approach can be pursued in the future. A new ribbon motorized ribbon holder assembly could be constructed with a design similar to the objective turrets in advanced microscopes or CD changers. Simultaneously fabricated ribbons could be loaded in one go and selected using a control system mid-print depending upon the cell type to be transferred.

Heterotypic heterocellular arrays:

Printing heterogenous heterocellular arrays, with multiple cell types co-localized in each spot, involves executing the motion control code multiple times, once for each cell type, and switching ribbons once a cell type has been deposited onto all spots of the array. In the present example, human breast cancer cells and fibroblasts are patterned in co-localized spots in an array, with

roughly the same density of each cell type within a spot. Once the motion control code was programmed into the controller, the ribbon seeded with the first cell type was mounted, the substrate was raised to be within 100um of the ribbon, the laser beam was focused on the ribbon interface, appropriate regions were chosen, and cells were printed onto all of the designated spots by executing the executing the motion control code. Next, the substrate stage was first translated back to the first spot of the array and then lowered (with the substrate affixed in place using a 3D printed clip), the ribbon stage was translated in the X direction, the ribbons were switched, the ribbon stage was realigned with the laser beam path and substrate, and the substrate was raised to be within 100um of the new ribbon. The laser beam was then refocused on the ribbon interface, appropriate regions were chosen and the cell droplets were printed "stacked" on top of the previously printed spots by re-executing the motion control code. This procedure is illustrated in Figure 4-11.

Similar to printing homotypic heterocellular arrays, changing the ribbon mid-print adds a manual step to the workflow, increases the amount of time the cells spend outside the incubator and limits the size of the arrays that can be printed due to ribbons simultaneously drying out. Additionally, stacking droplets on top of previously printed droplets exposes the first cell type to additional jolts of shear stress from the subsequent droplets landing and could potentially decrease cell viability.

However, this approach was found to be advantageous compared to simply seeding the ribbon with a co-culture and then printing using the general protocol. The cell type printed first – whether that be breast cancer cells or fibroblasts – remained viable in co-localized spots, and the order of stacking did not influence cell viability. Moreover, since the *in situ* camera and setup is not conducive to fluorescent imaging, it is impossible to distinguish between the two cell types on a co-cultured ribbon and it is consequently impossible to identify a region containing both cell types. Despite efforts to manually homogenize the cell suspension and maintain the concentration of both cell types to be as close as possible, printed spots frequently lacked the presence of one cell type or another. Obtaining an array with heterotypic cell spots required several attempts. On the other hand, stacking deposited droplets led to the presence of both cell types in all spots of most printed arrays.

The drawbacks in terms of limitations of array size and tediousness of the workflow can be addressed by implementing an automated ribbon changing assembly with a turret design in the future, wherein simultaneously fabricated ribbons can be loaded and used interchangeably for patterning cells in any user defined geometry.

4.3.4 LDW printed cancer-stromal cell arrays
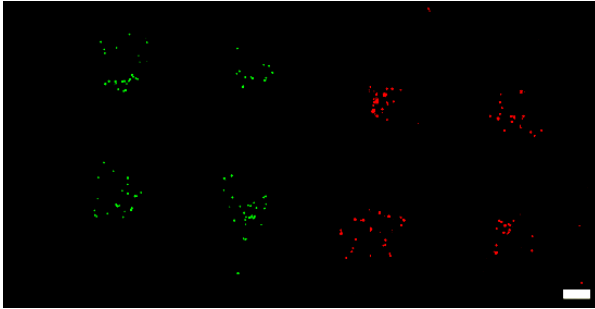
Figure 4-12 Human BJ fibroblasts (green) and MDA-MB 231 (red) triple negative breast cancer cells patterned as homotypic spots in a 4x2 heterocellular array using laser direct write bioprinting. Scale bar = 200um
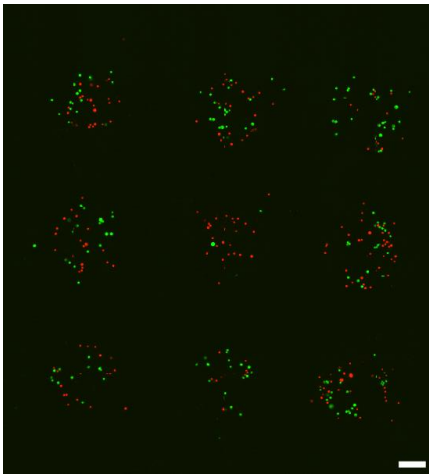
Figure 4-13 Human BJ fibroblasts (green) and MDA-MB 231 (red) triple negative breast cancer cells patterned as heterotypic colocalized spots in a 3x3 heterocellular array using laser direct write bioprinting. Scale bar = 200um

Heterocellular arrays composed of human triple negative breast cancers cells (MDA-MB 231) and fibroblasts (BJ) were printed using laser direct write. Breast cancer cells were labeled with red fluorescent dye and fibroblasts were labeled with green fluorescent dye prior to printing and the cell density on the ribbon was 1M cells/mL. Figure 4-12 shows a representative image of homotypic breast cancer and fibroblast spots printed in a 4x2 array. Figure 4-13 shows a representative image of heterotypic breast cancer and fibroblast spots printed in a 3x3 array. The scale bar in both cases is 200um.

Both images were acquired 24 hours post printing, after rinsing the dishes with media to remove any unattached nonviable cells or debris once the patterned cells had been allowed to attach overnight. Hence, continued attachment of both cell types indicated viability. Further, as the arrays were printed with a focused laser spot size of 300um in the columnar jetting regime, the cells were also observed to have migrated beyond the boundaries of the printed spots. This mirrors the behavior of MDA-MB 231 breast cancer cells and BJ fibroblasts (both highly migratory cell types) on adherent substrates *in vitro*, where they are commonly seen to migrate individually and collectively away from regions of higher cell density. Table 4-1 and Figure 4-14 summarize their migratory behaviors homotypic and heterotypic heterocellular arrays, expressed as the percentage of the number of cells of each type to have shown a net migration

beyond the boundary of the laser transferred spot within 95% confidence intervals.

Table 4-1 Migratory behavior of breast cancer cells and fibroblasts printed in heterocellular arrays with homotypic and heterotypic cell spots (n=9 for heterotypic spots, n=4 for homotypic spots)

Heterocellular Array & Cell Type	% cells migrated beyond 300um printed spot boundary after 24h (mean ± 95% CI)
Homotypic spots (cumulative)	35% ± 15
Breast cancer cell spots	49% ± 16
Fibroblast spots	21% ± 15
Heterotypic spots (cumulative)	46% ± 7
Breast cancer cells in heterotypic spots	56% ± 10
Fibroblasts in heterotypic spots	33% ± 8

Cells printed in both homotypic and heterotypic colocalized spots displayed net migration beyond the printed spot. In general, a higher percentage of breast cancer cells had migrated beyond the spot boundary compared to fibroblasts after 24 hours post-print, a finding that aligns with observations in previous

studies which show that cancer cells migrate approximately twice as fast as fibroblasts on adherent substrates [14] [15].

In conclusion, the capability of laser direct write to successfully print multiple cell types in user-defined geometries would allow for perturbation and study of cell-cell interactions and cell dynamics in healthy and diseased microenvironments at high resolution going forward.
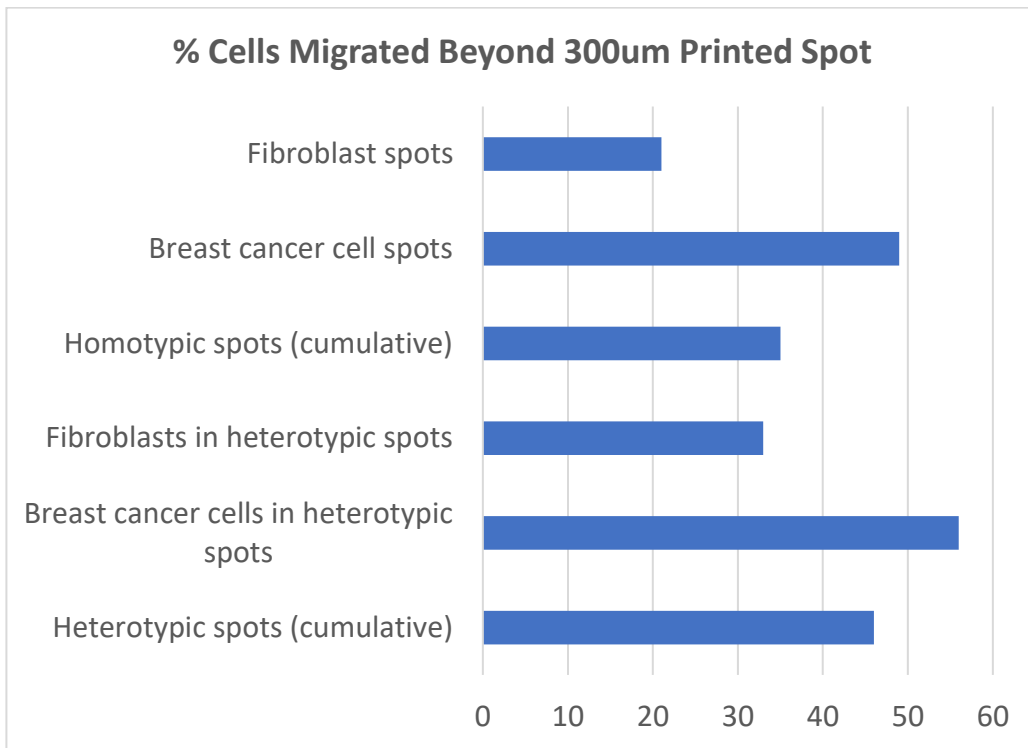
Figure 4-14 Migratory behavior of breast cancer cells and fibroblasts printed in heterocellular arrays with homotypic and heterotypic cell spots (n=9 for heterotypic spots, n=4 for homotypic spots)

4.4 Materials and Methods

Laser spot size characterization

A glass slide was coated with permanent marker ink and loaded on the substrate stage. The laser was focused on the slide and fired to ablate the ink. The slide was then imaged under a microscope and the spot size characterized.

Pre-transfer cell culture

MDA-MB 231 human triple negative breast cancer cells and BJ human fibroblasts (ATCC, Manassas VA) were cultured in DMEM supplemented with 10% FBS, 1% HEPES, 1% L-glutamine, 1% sodium pyruvate, 1% essential amino acids, 1% nonessential amino acids, 1% antibiotic-antimycotic and 0.012% insulin (all reagents from Thermo Fisher Scientific, Waltham MA; FBS from Cytiva, Marlborough MA) at 37C with 5% CO_2 and 95% RH.

Substrate preparation

2mL 0.1mg/mL of high molecular weight (>70kDa) poly-L-lysine (MP Biomedicals, Santa Ana CA) solution in PBS (Thermo Fisher Scientific, Waltham MA) was pipetted on dish and entire surface was coated. The dish

was incubated for at least 2hrs to allow PLL to adsorb onto surface. The solution was pipetted out and the dish left to dry overnight inside a sterile cell culture hood.

The dish was then spin coated with 10% gelatin (Sigma Aldrich, St Louis MO) in basal media at 400rpm and refrigerated for 4 minutes to solidify. Next, it was gently rinsed with cold (4C) DMEM across the gelatin and liquid aspirated. It was then incubated for at least 30 minutes prior to printing cells.

Ribbon preparation

The print ribbon was sterilized with 70% ethanol and the side to be coated was warmed for 10s on a sterile surface of 60C hotplate. It was then spin coated with 20% gelatin in PBS at 2000prm. The ribbon was incubated for at least 3 minutes prior to seeding cells.

The cells were detached from flasks with 2.9mM EDTA (Sigma Aldrich, St Louis MO) in PBS or 0.25% trypsin in 0.53mM EDTA (Thermo Fisher Scientific, Waltham MA). The detachment solution was quenched with fresh media and centrifuged to purge. Cells were resuspended in warmed media and triturated to homogenize into single cell suspension of density between 500k-1M cells/mL.

500uL of cell suspension was seeded onto coated by pipetting in center and gently tilting ribbon in all directions for an even coat. The ribbon was then incubated for at least 7 minutes. Then it was tilted and excess media gently dabbed using a lint free wipe. Next, the ribbon was allowed to dry in the hood for 3-4 minutes before commencing printing.

If printing multiple cell types, the cells were fluorescently labeled with CellTracker dyes (Thermo Fisher Scientific, Waltham MA) and multiple ribbons were prepared with one ribbon per cell type.

Printing process

The laser was warmed up by firing 2000 pulses at 20Hz and then 5000 pulses at 100Hz with maximum voltage applied to the electrodes (15kV). The motorized iris was adjusted to desired spot size. Next, adjust electrode voltage for a fluence of 0.4J/cm^2 at the ribbon.

The motion control code for the desired printing pattern was programmed into the motion controller.

All motorized stages were homed. The ribbon was loaded into holder with coated side facing downwards. The substrate dish was mounted on the substrate platform. The substrate stage was moved in place into the laser beam path. The z-position of objective was adjusted to focus *in situ* camera on

substrate surface to choose desired starting spot. Now, the ribbon stage was moved in place into the laser beam path. The objective was adjusted to focus on the ribbon-hydrogel interface with cells clearly visible. Raise the substrate in 50um increments until <500um from the ribbon coating with the help of side view camera. Then the ribbon was moved in the x-y plane in 10-50um to located a desired region to print cells.

Laser pulses were fired to print the cells and repeated at different regions of the ribbon until a successful print was achieved. The motion control code was executed and substrate was moved to the next location where cells needed to be printed. A desirable region was located on the ribbon and the laser fired pulses fired again. Once successful printing had been achieved for the entire array, the substrate dish was lowered, its lid replaced and immediately transferred into the incubator.

If printing multiple cell types within the same array, switched ribbons after printing one cell type by lowering substrate stage, homing the ribbon stage and replacing the ribbon in the holder before realigning the ribbon, raising the substrate and printing cells as described above.

Post-transfer cell culture

Once the array was printed, dish was incubated without adding media for 15 minutes. Then, warmed media was pipetted in gently, proceeding in a dropwise manner and switching to a P200 pipette when close to the printed cell array. Finally, dish was incubated undisturbed overnight before imaging.

Statistical analysis

Cell migration data were reported with 95% confidence intervals around the mean. For heterotypic spots, n=9 and for homotypic spots, n=4 per cell type. Statistical analyses were performed in R.

Illustrations

Illustrations were created using BioRender.

5 Bioprinting Human Macrophages

5.1 Introduction

The most enriched cell types in the breast tumor microenvironment are breast cancer cells, cancer-associated fibroblasts and tumor-associated macrophages and both the stromal and immune components play a key role in breast cancer growth, invasion and metastasis [11]. In order to build physiologically relevant *in vitro* models of the breast tumor microenvironment and recapitulate metastatic cell dynamics, it is necessary to incorporate the most abundant cell types. Most tissue engineering and bioprinting techniques, however, tend to neglect including the immune component, presumably because human immune cells can be challenging to work with *in vitro.* Laser direct write bioprinting is a high resolution, gentle and customizable cell printing technique conducive to printing a variety of cell types [3] [4]. In the previous section, a generalized protocol was developed to print multiple cell types. Herein, various adaptations were made to develop a novel protocol to viably bioprint human macrophages with high fidelity.

5.2 Hypothesis

Laser direct write bioprinting is conducive to printing sensitive, weakly adhesive human immune cells in user-defined geometries.

5.3 Results and Discussion

A generalized protocol for laser direct write bioprinting of cells was developed in the previous chapter and adapted to print breast cancer cells and fibroblasts – two highly enriched cell types in the breast tumor microenvironment. However, there is another cell type that is also enriched in the breast tumor microenvironment, namely the tumor associated macrophage, which has been shown to play a key role in breast cancer metastasis [16] [17]. Most current bioprinting and biofabrication strategies fail to incorporate the immune component in tissue engineered constructs, including those aiming to recapitulate the tumor microenvironment. This is presumably due to the fact that human immune cells tend to be delicate or challenging to work with *in vitro*. Hence, considering the gentleness and versatility of the laser direct write bioprinting technique as well as the importance of immune cells in tumor (and tissue) microenvironments, the general protocol was adapted to develop a

novel method to print human macrophages. This technique should pave the way for bioprinting more physiologically relevant, immunocompetent tissue constructs.

5.3.1 Adaptation of laser direct write cell printing protocol for THP-1 macrophages

THP-1 cells have been extensively utilized to study human macrophage functions and signaling pathways. In their undifferentiated state, THP-1 monocytes are non-adherent suspension cells but become adherent when differentiated into macrophages. Differentiated THP-1 macrophages are weakly adhesive as they form small focal adhesion complexes with fine actin networks [18] as well as delicate *in vitro*, and hence required specific adaptations to the printing protocol which relies on cell adhesion for maintaining fidelity of the patterned cells on the substrate. The modifications to the respective stages are described below.

Pre-transfer cell culture modifications:

Culture media modification:

THP-1 monocytes and macrophages are normally cultured in RPMI supplemented with 10% FBS, 1% L-glutamine, 1% sodium pyruvate and 1% antibiotic-antimycotic. The standard media recipe was found to result in high levels of macrophage apoptosis, particularly when cells were subject to the stressors associated with the printing process. Hence, a modified media formulation was used, with the standard media recipe further supplemented with 1% HEPES, 25mM glucose and 0.012% insulin, as well as replacing antibiotic-antimycotic with 1% penicillin-streptomycin. Also, since standard media frequently led to cell death due to loss of adhesion of the weakly attached macrophages, it was supplemented with 1% MEM non-essential amino acids.

The HEPES acts as a buffer to maintain the pH of the media, as these cells are more sensitive than most to pH changes [19]. Since standard RPMI has a relatively low concentration of glucose, additional glucose was added to provide metabolic support, as monocytes/macrophages tend to be highly metabolically active [20]. Alternatively, the concentration of sodium pyruvate could be increased as it too is an easily accessible carbohydrate source and plays roles in amino acid metabolism and initiation of the Kreb's cycle. Supplementation with insulin served to reduce macrophage apoptosis. The role of insulin in inhibiting macrophage apoptosis has been established in previous studies [21].

The antimycotic appears to be toxic to this cell type, and eliminating it from the media reduced cell death. Finally, since differentiated THP-1 macrophages are weakly adherent due to their smaller focal adhesion complexes with fine actin filaments, the media during and after differentiation was supplemented with non-essential amino acids to support the formation of stronger focal adhesions, which comprise in large part of polymerized actin (a globular protein composed of 375 amino acids with tight binding sites that mediate binding with other actin monomers to form polymerized filaments). Previous studies have also shown enhancement of macrophage adhesion by addition of non-essential amino acids [22].

Differentiation protocol modification:

The standard method for differentiating THP-1 monocytes into macrophages involves treating the cells with 150nM of phorbol 12-myristate 13-acetate (PMA) for 24 hours [23]. However, this was found to not only be inefficient, with the majority of cells remaining undifferentiated (and consequently nonadherent), but also harsh on the cells leading to cytotoxicity and loss of viability when macrophages were manipulated using the gentle techniques in the days following the differentiation treatment. Hence, the protocol was modified to differentiate THP-1 monocytes in a more gradual and gentler manner by treating with 40nM PMA for 72 hours. The differentiation media, as previously

mentioned, was also supplemented with nonessential amino acids to support formation of actin filaments and adhesion. This was followed by a "rest period" of 120 hours wherein the PMA treatment was withdrawn and the macrophages were left to incubate undisturbed in adherent flasks/dishes. This was found to increase the differentiation efficiency resulting in larger number of adherent cells and more stable macrophages for printing. Since terminally differentiated THP-1 macrophages do not proliferate, overconfluence was not a concern during the rest period.

Substrate preparation modifications:

As previously discussed, in order to increase the number of electrostatic binding sites on the receiving substrate, the surface was treated with high molecular weight PLL and spin coated with a 100um thick layer of 10% gelatin in basal media to cushion the landing droplets from shear stress (as well as support attachment of printed cells). While that was sufficient to facilitate attachment and survival of robust, strongly adherent cell types such breast cancer cells and fibroblasts, the procedure required adaptation for printing the more delicate and weakly adhesive THP-1 macrophages.

The substrate dish was spin coated with 100um thick layer of 15% gelatin in RPMI instead of 10% to provide stronger attachment cues to the printed cells.

While a higher concentration such as 20% would provide even stronger attachment cues, it also increases the stiffness thereby reducing the cushioning effect, leading to loss of viability with cells subject to increased shear stress. Further, after the spin coated gelatin layer was solidified by refrigerating for 4 minutes, it was rinsed with cold (4C) complete macrophage media instead of simply the basal media as before. This ensures the presence of more nutrients to nourish the cells in the post-print incubation period before dispensation of additional media – specifically, the supplements incorporated into the modified formulation such as insulin and amino acids that promote macrophage viability and attachment. Moreover, the presence of serum in complete media serves to further facilitate cell adhesion.

Finally, it was important to also consider characteristics of the cell type beyond robustness and adhesiveness. When the receiving substrate surface was treated with PLL, minimal adhesion of printed THP-1 macrophages was observed. The reason for this effect, upon consulting the literature, was determined to be the secretion of high levels of a variety of proteases by activated macrophages, in preparation for one of their primary functions i.e., phagocytosis [24]. It is conceivable that the differentiated macrophages were stimulated by the stressors of the printing process to become activated. Hence, the substrate surface was treated with poly-D-lysine (PDL) instead of the L-enantiomer. Different enantiomers of the same molecule, while possessing the

same chemical formula, can often have differing biological activity due to their "mirror image" chemical structure, and PDL is thus more resistant to degradation by cellular proteases while still providing electrostatic adhesive cues as strong as PLL [25]. Switching to PDL treatment resulted in increased macrophage adhesion post-transfer.

Ribbon preparation modifications:

Only one modification was necessary to ensure increased THP-1 macrophage viability during the ribbon fabrication process. Instead of a harsh proteolytic agent such as trypsin, Accutase – an enzymatic agent formulated to be extremely gentle to cells – was used to detach the macrophages to seed on the ribbon. It was also helpful to use media with a higher serum concentration such as 15-20% to neutralize the cell detachment solution before resuspending and seeding onto the gelatin coated ribbon.

Post-transfer cell culture modifications:

Once the THP-1 macrophage spots were deposited, the receiving dish was subsequently incubated for 25 minutes undisturbed. The additional incubation time compared to the protocol for cancer cells and fibroblasts helped enhance macrophage adhesion. Next, cold macrophage media at 4C was gently

dispensed in a dropwise manner using a P200 pipette in regions closest to the printed array. Adding cold media instead of warmed media (as per the general protocol) was advantageous because it solidified the gelatin layer and prevented the cells from dispersing from the shear stress of the dispensed media. THP-1 macrophages were found to tolerate the sudden temperature difference without losing viability. Finally, the substrate dish was left undisturbed for a further 15 minutes inside a sterile hood after pipetting in the media, before being carefully transferred to the incubator.

5.3.2 LDW printed human THP-1 macrophages

Although macrophages are also migratory cells, they typically only display significant net migration in response to directional stimuli [26] [27] [28]. This is unlike the behavior of, say triple negative breast cancer cells, which migrate aggressively away from regions of high cancer cell density even in the absence of any other stimulus. The receiving substrate was uniformly coated with PDL or PLL and gelatin, and no external chemotactical, haptotactical or durotactical stimuli were applied. Thus, the macrophages were expected to be largely confined to their printed spots when imaged after 24 hours. This offered an opportunity to validate the ability of laser direct write to pattern cells, even weakly adhesive ones such as THP-1 macrophages, with high fidelity – in

addition to demonstrating the ability to bioprint sensitive human immune cells. Bioprinting cells with high fidelity would allow for tight control of the number of cells of a given type that are transferred as well as enable recapitulation of complex native tissue microarchitectures *in vitro* – both of which play key roles in cell and tissue function.

In order to test the cell patterning fidelity of the laser direct write technique, 2x3 arrays of THP-1 macrophages were printed, with 6 different laser spot sizes between 100 and 300um. The laser spot sizes were characterized and the corresponding variable aperture coordinates noted. The laser fluence at the ribbon interface was kept constant at $0.4J/cm^2$ by adjusting the discharge voltage for each spot size to print the cells (Figure 5-1).

The cells were printed and cultured overnight according to the protocol described above with a ribbon cell density of 1M cells/mL. The substrate dish was then rinsed with media to remove any unattached nonviable cells and debris, and imaged 24 hours post-print, with a representative image depicted in Figure 5-2 (scale bar = 100um). The printed macrophages in all spots displayed a flat, spread out shape suggesting attachment to the substrate surface. The elongated morphology observed in the printed spots also resembles human macrophage morphology when cultured on an adherent substrate *in vitro* [29]. Moreover, continued adhesion to the substrate also indicates that the macrophages, despite their sensitive nature, remained viable

post-printing. This would pave the way for bioprinting immunocompetent tissue constructs by addressing the gap of the missing immune component in conventional bioprinting and biofabrication approaches.
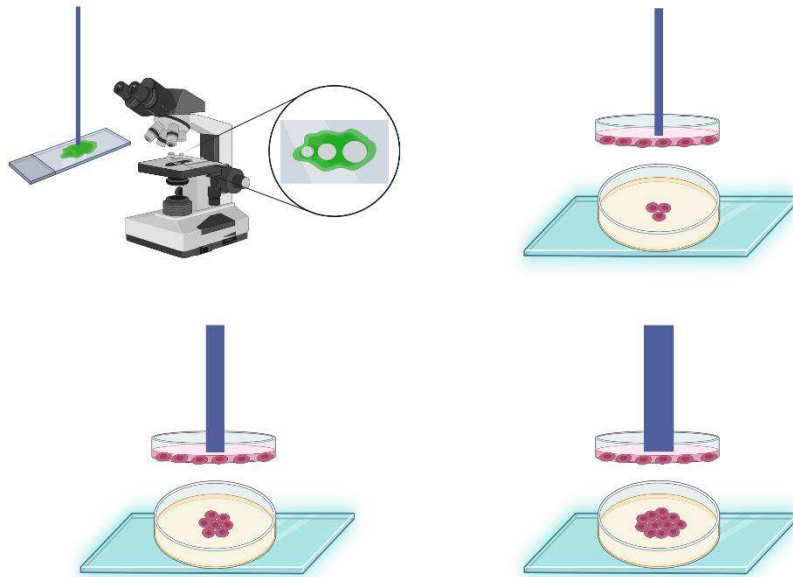
Figure 5-1 Characterization of the laser spot size and printing differently sized spots of THP-1 macrophages by keeping laser fluence at the ribbon interface constant.

The printed macrophage spot sizes were measured and plotted on the ordinate against the characterized focused laser spot sizes on the abscissa (Figure 5-3). If the printed spot sizes perfectly matched the laser spot sizes, this curve would be a straight line with a slope of 1. A linear regression analysis was performed, and the estimated slope was found to be 1.216 ± 0.166 (95% confidence

intervals, adjusted R^2 = 0.96). This indicates that the printed macrophage spots were, on average, just 1.2x the size of the respective laser spots, which – considering the high goodness of fit of the linear model – indicates that the printed spots did indeed closely resemble the focused laser spot size. This demonstrates the capability of the laser direct write platform to pattern cells, even sensitive and weakly adhesive ones, with high fidelity. Being able to print cells with high fidelity would allow for perturbation and study of cell-cell interactions and cellular dynamics with high precision in tissue microenvironments.

Hence, to conclude, laser direct write bioprinting should serve as an attractive technique to fabricate immunocompetent tissue constructs with highly defined geometries going forward.
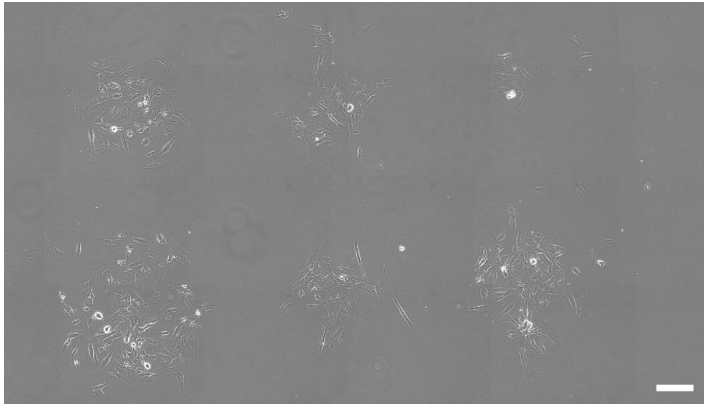
Figure 5-2 2x3 array of THP-1 macrophages printed using laser direct write, with 6 different spot sizes. Scale bar = 100um
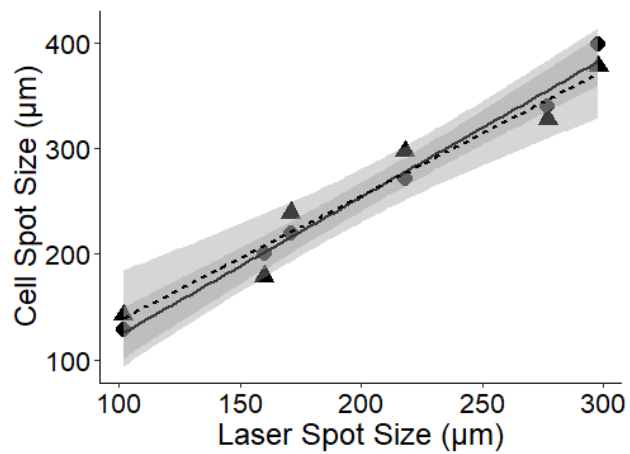
Figure 5-3 Laser direct write printed THP-1 macrophage spot sizes vs focused laser spot size. Linear regression analysis with shaded regions indicating 95% CI's (Slope = 1.2, adjusted R^2 = 0.96).

5.4   Materials and Methods

Cells were printed according to the protocol described in the previous chapter with the following adaptations for printing THP-1 macrophages.

Pre-transfer cell culture

THP-1 monocytes (ATCC, Manassas VA) were cultured in RPMI with 10% FBS, 1% L-glutamine, 1% pyruvate, 1% HEPES, 25mM glucose, 0.012% insulin and 1% penicillin-streptomycin. THP-1 macrophages were further supplemented with 1% MEM nonessential amino acids. (All reagents from Thermo Fisher Scientific, Waltham MA; FBS from Cytiva, Marlborough MA).

Monocytes were differentiated into macrophages by treating with 40mM phorbol 12-myristate 13-acetate (Bio-Techne, Minneapolis MN) and 1% nonessential amino acids for 72 hours followed by a rest period of 120 hours in macrophage media.

Ribbon preparation

Macrophages were detached using Accutase (BD Biosciences, Franklin Lakes NJ).

Substrate preparation

Substrate dishes were treated with high molecular weight (>70kDA) poly-D-lysine (MP Biomedicals, Santa Ana CA) instead of poly-L-lysine. Dish was then spin coated with 15% gelatin (Sigma Aldrich, St Louis MO) in RPMI. Then cold (4C) complete medium was washed instead of only basal medium.

Post-transfer cell culture

Immediately after printing, substrate dish was incubated for 25 minutes (instead of 15). Next cold (4C) media was gently pipetted in. The dish was left undisturbed in the cell culture hood for a further 10 minutes before being transferred into the incubator.

Statistical analysis

Linear regression analysis was performed to assess the relationship between the printed macrophage spot sizes and the characterized laser spot sizes.

Data were reported with 95% confidence intervals around the mean.

Experiments were conducted in duplicate. Statistical analyses were

performed in R.

Illustrations

Illustrations were created using BioRender.

6 Role of Symmetry in Diabetic Wound Healing

6.1 Introduction

Conventional wound healing assays offer little control over the geometry of the wounds created in cell layers and are hence unable to evaluate the influence of symmetry on cutaneous wound healing. Those that do offer control over wound geometry are cell exclusion assays that involve placing stoppers and growing cell layers around them, and hence do not trigger the wound healing response by injuring the cell layer. Herein, a novel laser direct write photoablation technique was developed that is able to precisely ablated wounds in any user-defined geometry. The laser photoablated wounds were then utilized to develop a novel to elucidate the roles of symmetry and glycemic conditions in dermal wound healing, and how these variables may interact in diabetic patients.

6.2 Hypotheses

Laser direct write photoablation is conducive to creating wounds of desired geometries with high precision in cell layers.

Additionally, based on clinical observations on cutaneous wounds [30] [31] [32], the following biological hypotheses were tested using a novel laser photoablation based wound healing assay:

- Symmetric wounds heal significantly faster than asymmetric wounds.

- Wounds in euglycemic conditions heal significantly faster compared to those in hyperglycemic conditions.

6.3 Results

A novel *in vitro* CAD/CAM laser photoablated wound healing assay was developed to examine the influence of symmetry on cutaneous wound healing, taking advantage of the precise control over geometry offered by the laser direct write processing technique. In addition, the influence of glycemic conditions was examined by modifying the culture conditions. This assay enabled the analysis of the interaction of symmetry and glycemic conditions on wound healing rates.

In comparison to traditional wound healing assays, this assay is highly advantageous. Traditional assays generally do offer much control over the geometry of the wounds created and hence cannot be used to study the influence of factors such as shape or symmetry on healing. The conventional

techniques that do offer control over wound geometry involve stoppers placed in dishes and cells grown around them, which do not injure the cell layer and consequently do not trigger the wound healing response.

6.3.1 Study design

Skin is composed of three major layers – the epidermis, the dermis and the hypodermis (listed in increasing order of depth). Human dermal fibroblasts were chosen as the cell type for this study instead of epidermal keratinocytes because deeper wounds – which involve injury to the dermis and not just the epidermis – are generally considered to be clinically significant for diabetic patients. Previous studies have shown that the culture conditions determine the wound healing behavior of cutaneous cells *in vitro*, rather than the source [32]. It was demonstrated that when skin cells harvested from diabetic patients and healthy patients and cultured in hyperglycemic and euglycemic conditions, cells cultured under normal glucose concentrations closed wounds faster compared to cells cultured under diabetic glucose concentrations. There was no significant difference between wound closure rates of cells from diabetic and healthy patients within a given glycemic condition. Hence, BJ CRL-2522 human dermal fibroblasts were used to simulate both conditions in this study.

Table 6-1 Experimental groups for laser photoablated cutaneous wound healing assay to study the influence of symmetry and glycemic conditions

Wound Geometry / Glycemic Condition	Symmetric (Square)	Asymmetric (Irregular)
Euglycemic (11mM)	Large ($9mm^2$) wound	Large ($9mm^2$) wound
	Small ($1mm^2$) wound	Small ($1mm^2$) wound
Hyperglycemic (50mM)	Large ($9mm^2$) wound	Large ($9mm^2$) wound
	Small ($1mm^2$) wound	Small ($1mm^2$) wound

Aligned with previous studies, euglycemic conditions were defined as 11mM and hyperglycemic conditions as 50mM [32] [33]. Media changes were done with the same frequency across all groups.

In order to ensure that any observed effects were not an artifact of a particular wound dimension, the wound healing assay was performed for wounds of two different sizes – $1mm^2$ and $9mm^2$. The experimental design for the respective control and treatment groups is summarized in Table 6-1.

Each wound was independent i.e., one wound per dish. All experiments were performed in triplicate (n = 3). Since large wounds would obviously take longer than small wounds to heal, the dataset was partitioned into two, two-factor datasets based on wound size, to avoid the size confounded other effects.

Statistical analyses were performed using two-way ANOVA and Bonferroni corrected p < 0.05 was considered significant (i.e. significance level α = 95%). The p-value was adjusted accordingly if significant interactions were present between the variables. Effect sizes were expressed as generalized eta squared (GES) values with 95% confidence intervals.

Photoablated wounds were imaged every 12 hours. Wounds were considered fully healed when confluence was attained in the wound area and there was no change in the morphology of the cell layer on two consecutive readings, and then the first of those two readings was considered as the healed timepoint.

6.3.2 Development of optimized motion control codes for laser photoablation of wounds with symmetric and asymmetric geometries

Two wound geometries of equal areas were designed – one highly symmetric and the other asymmetric. The symmetric shape was chosen to be a square with 8 symmetries (4 line reflections and 4 rotations in right angle multiples) and the other wound shape was created to lack any symmetry, reflective or rotational. The areas of the shapes were ensured to be as similar as feasible – for both wound sizes ($1mm^2$ and $9mm^2$ respectively) – to ensure a reasonable comparison for elucidating the role of symmetry.

First, the laser spot profile was characterized as previously described. An iris configuration resulting in a focused laser spot size of 300um was chosen for photoablation of wounds to ensure precise ablation but also minimize the time that the cells spend without media in the laser ablation chamber. Next, in order to develop the control codes for CAD/CAM motion in the X-Y plane, the sketched wound shapes were overlaid with a grid with unit cell equal to the focused laser spot size. Then translational codes programming the ablative path of the focused laser spot relative to the substrate were written with the number and length of passes determined by the overlaid gridlines. These codes were subsequently compiled into G-code and programmed into the controller.

Upon conducting preliminary experiments, it was determined that a meandering pattern for focused laser spot across the substrate was optimal for ablating precise wounds in cell layers. Moreover, it was found that overlapping adjacent meandering focused laser spot paths by 50% resulted in the highest fidelity between the intended wounds geometries and the actual photoablated wound geometries in cell layers, leaving no un-ablated cells within the wound area.

Figure 6-1 summarizes the entire process of generating optimized motion control codes for symmetric square and asymmetric irregular wounds in of the same areas (and two different sizes of each wound geometry) in cell layers, where d represents the characterized focused laser spot size (chosen to be 300um for this study).

101
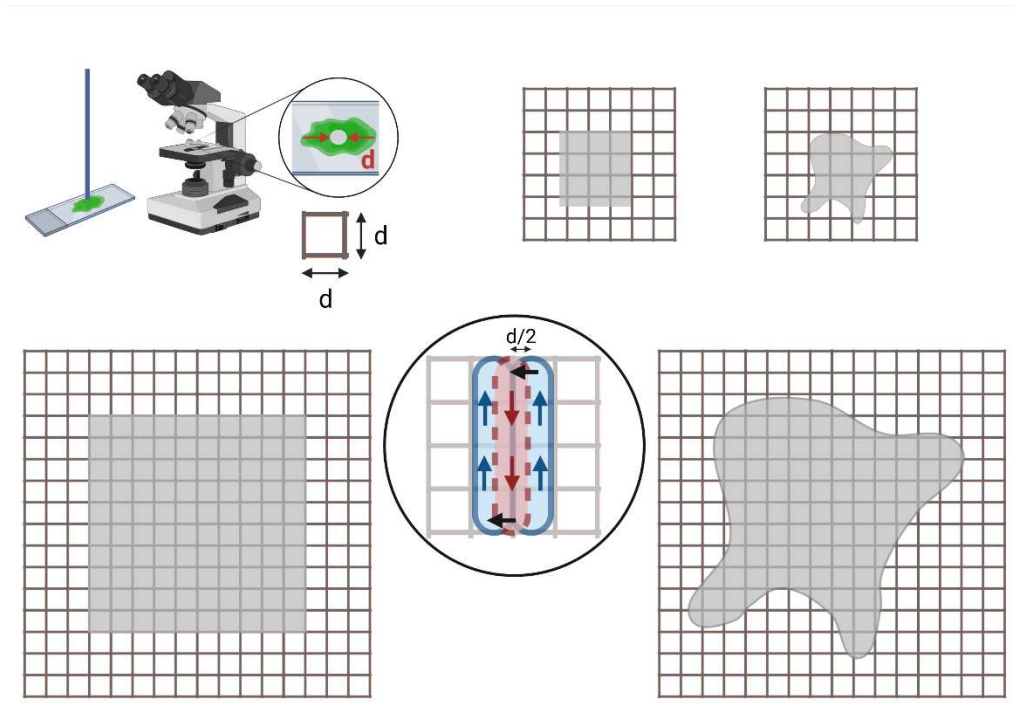
Figure 6-1 Generation of motion control codes for laser photoablation of symmetric and asymmetric wounds of identical areas in cell layers. The characterized focused laser spot size, d, becomes the unit cell of the grid overlay, according to which the codes were written for ablating wounds of two sizes. A meandering ablative laser spot path with 50% overlap (i.e. d/2) was optimal for precise photoablation and high wound fidelity. d = 300um

The laser parameters for photoablation were then optimized. Preliminary experiments showed that a laser pulse repetition rate of 100Hz and a focused laser spot velocity of 1mm/s was optimal for ablating wounds in cell layers. The threshold photoablation fluence was found to be between 0.31-0.34 J/cm^2 and varied slightly between batches of cells. Hence, "test petri dishes" containing

cells from the same batch and passage number were cultured in identical conditions alongside the petri dishes containing cells to be ablated, and prior to performing any photoablation of the wounds to be assayed, the threshold fluence was determined using the test dishes by incrementally increasing the laser discharge voltage with the laser pulsing at 100Hz and the 300um spot moving at 1mm/s.

6.3.3 Laser direct write photoablation protocol

Cell culture and imaging:

BJ CRL-2522 human dermal fibroblasts were cultured at 37C with 5% CO_2 and 95% RH in RPMI supplemented with 10% FBS, 1% HEPES, 1% L-glutamine, 1% sodium pyruvate and 1% antibiotic-antimycotic. This formulation has 11mM glucose, which was used for euglycemic conditions and was increased by adding D-glucose to make concentration up to 50mM to simulate hyperglycemic conditions. The cells were not serum starved for this assay because unlike traditional wound healing assays, the goal was not to assess cell migration alone but rather the process of wound closure as a whole.

Dermal fibroblasts were grown to confluence in their respective glycemic conditions before ablation. For each batch of cells to be ablated, a test dish with cells from the same batch and passage number were cultured under identical

conditions to facilitate determination of the threshold photoablation fluence. The photoablated wounds were cultured in their respective media formulations and imaged every 12 hours.

Laser direct write system preparation:

The laser gas was refilled and the laser was warmed up to optimal operating temperature as previously described, in order to achieve high pulse to pulse consistency of outputted energy. The laser spot size was characterized as previously described and the variable aperture set to result in a 300um focused spot size. The laser energy was continuously monitored throughout the ablation process with the *in situ* energy meter.

The motion control codes were composed into G-code (machine language) and programmed into the controller. Figure 6-2 illustrates the laser direct write photoablation setup.
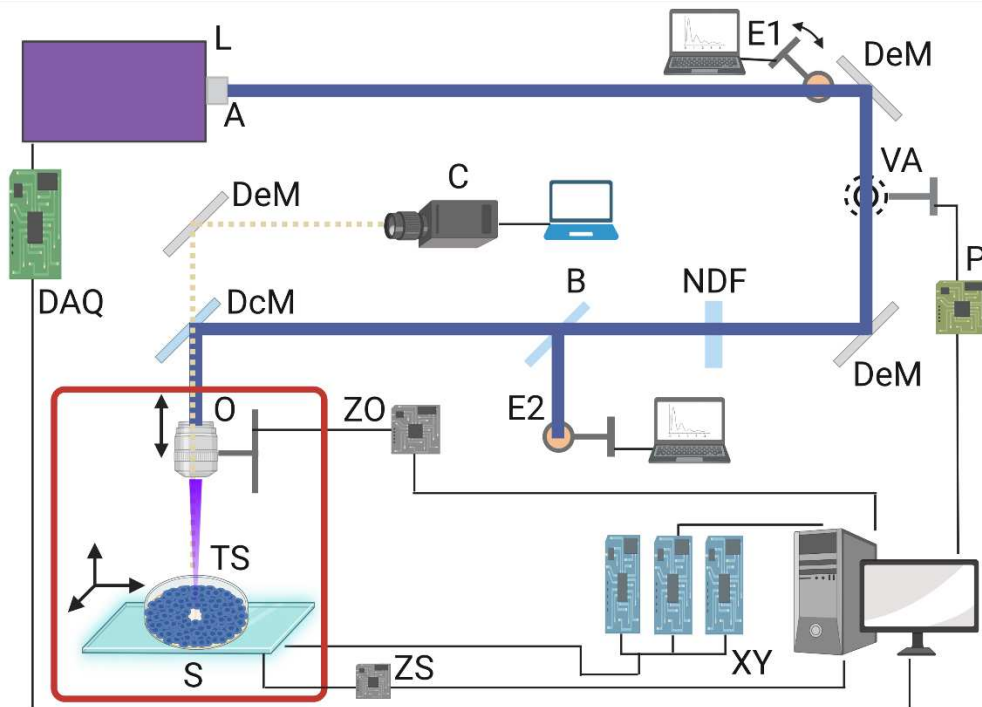
Figure 6-2 The laser direct write photoablation setup (TS: test substrate dish)

Photoablation process:

Once the laser direct write system was fully prepared, the media was aspirated from the test dish containing the confluent dermal fibroblast layer to be ablated using vacuum suction by gently tilting the dish. The thin layer of residual media that remained on the surface of the cell layer serves a dual purpose. Firstly, it keeps the cell layer hydrated and nourished during the ablation process, thereby maintaining viability of the non-ablated cells. Secondly, the thin film of liquid actually facilitates the photoablation of cells with high fidelity by achieving targeted lysis of the adherent cells [34]. Studies have shown that when a

nanosecond pulsed laser beam of adequate fluence is delivered to adhered cells covered with a thin film of liquid, a laser-induced plasma is formed which is immediately followed by the emission of a pressure shock wave and a cavitation bubble formation, expansion and collapse – all on a microsecond scale. Cell injury occurs as a result of both direct vaporization by the plasma as well the mechanical stresses associated with the cavitation bubble expansion and collapse. In fact, it has been shown that laser-induced cell lysis of adherent cells is most precise in terms of spatial confinement when the laser beam with fluence slightly above the ablation threshold is focused about at the surface of the liquid thin film covering the cells rather than on the plane of the cell layer itself.

The test dish was then mounted on the substrate stage (with the 3D printed clip to affix it in place) and the substrate stage was then raised until the laser beam was focused on the surface of thin media film covering the cell layer. As previously described, due to the optical alignment of the *in situ* camera with the laser beam, focusing the camera at the liquid interface resulting in the laser beam focusing on that plane too.

Next, the preprogrammed motion control code was executed synchronized with the laser pulsing. The laser discharge voltage was initially set to achieve a fluence at the work surface of 0.31 J/cm^2 and if insufficient to initiate photoablation, the discharge voltage was increased gradually until ablation

started occurring, as observed in real time using the *in situ* camera's video feed. Once ablation was achieved in the test dish, the laser discharge voltage and consequently the fluence was kept constant.

Media was then aspirated from the assay dish, which was mounted, laser beam focused at the liquid interface and the preprogrammed motion control code executed to photoablate the desired wound. Finally, media was replaced and the dish transferred to the incubator.

6.3.4   Photoablated wound characteristics

The wounds were photoablated in human dermal fibroblast layers in triplicate – for each wound geometry, size and glycemic condition – for an adequately powered study. Upon generation of the wounds, they were characterized to ensure that their dimensions matched the intended ones that formed the basis of the motion control codes. All small wounds with intended areas of 1mm^2 – *both symmetric and asymmetric* – had areas within a tolerance of 0.8%. Similarly, all large wounds with intended areas of 9mm^2 – *both symmetric and asymmetric* – had areas within a tolerance of 3%. This not only indicates the high fidelity that can be achieved using laser direct write photoablation of cells but also validates the comparison between symmetric and asymmetric wounds.

Representative images of wounds with both symmetric and asymmetric geometries are depicted in Figure 6-3 and Figure 6-4.
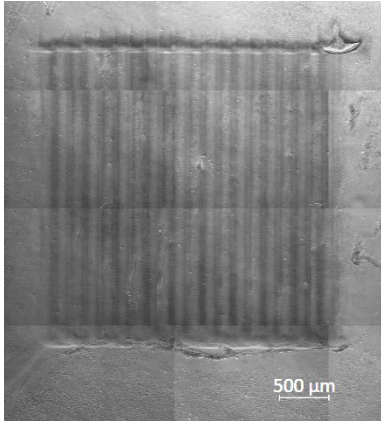
Figure 6-3 Laser direct write photoablated large symmetric wound in a dermal fibroblast layer. Scale bar = 500um
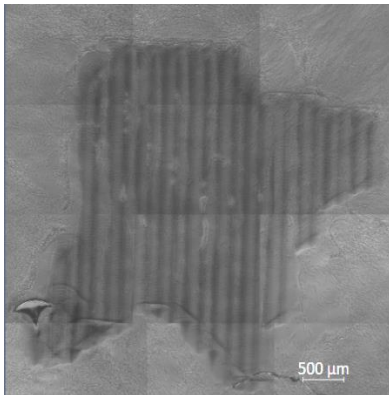
Figure 6-4 Laser photoablated large asymmetric wound in a dermal fibroblast layer. Scale bar = 500um

The wounded fibroblast layers were cultured in euglycemic and hyperglycemic conditions and imaged every 12 hours until complete wound closure. Wound healing times and wound healing rates in all experimental groups were recorded.

Large wounds healed slower than small wounds almost uniformly by a factor

of: $\dfrac{1}{3} * \sqrt{\dfrac{large\ wound\ area}{small\ wound\ area}}$

Larger wounds healing slower is not only a trivial finding but the above nonlinear scaling factor could also confound the effects of other variables. Hence, the three-factor dataset was partitioned by size into two-factor datasets with wound geometry and glycemic conditions considered as the independent variables for hypothesis testing comparisons using two-way ANOVA.

6.3.5 Large wound healing times comparison

Wound healing times for large symmetric and asymmetric wounds in euglycemic and hyperglycemic conditions were recorded. The data were homoscedastic, as determined by Levene's test (p=0.627). The influence of symmetry and glycemic conditions on large dermal wound healing times was analyzed using two-way ANOVA. Both symmetry and glycemic condition were found to have significant effects on large wound healing times (p=0.000163 and

0.000000143 respectively). No significant interaction between the variables was found (p=0.412). Tukey's test with Bonferroni corrected α was performed for pairwise comparisons.
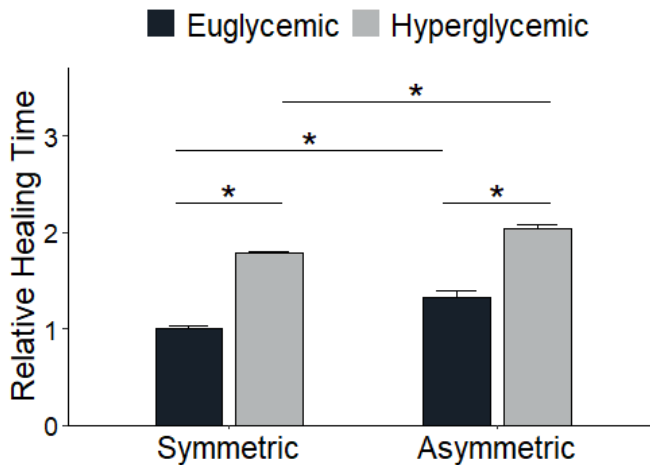
Figure 6-5 Influence of symmetry and glycemic conditions on large dermal wound healing times. * p<0.05; error bars represent standard error of the mean

Asymmetric large wounds healed significantly slower than symmetric large wounds – both in euglycemic (p=0.0032) and hyperglycemic (p=0.0149) conditions. Further, large wounds in hyperglycemic conditions closed significantly slower than those in euglycemic conditions – this was observed for both symmetric (p=0.000007) and asymmetric (p=0.000015) geometries. These effects are illustrated in Figure 6-5.

To ascertain which factor had the stronger effect, the effect sizes were determined using the respective 95% CI GES values. It was found that for large dermal wounds, glycemic condition had a 2.4x stronger influence on healing times.

6.3.6 Small wound healing times comparison

Wound healing times for small symmetric and asymmetric wounds in euglycemic and hyperglycemic conditions were recorded. The data were homoscedastic, as determined by Levene's test (p=0.859). The influence of symmetry and glycemic conditions on small dermal wound healing times was analyzed using two-way ANOVA. Both symmetry and glycemic condition were found to have significant effects on small wound healing times (p=0.0000098 and 0.000182 respectively). No significant interaction between the variables was found (p=0.141). Tukey's test with Bonferroni corrected α was performed for pairwise comparisons.
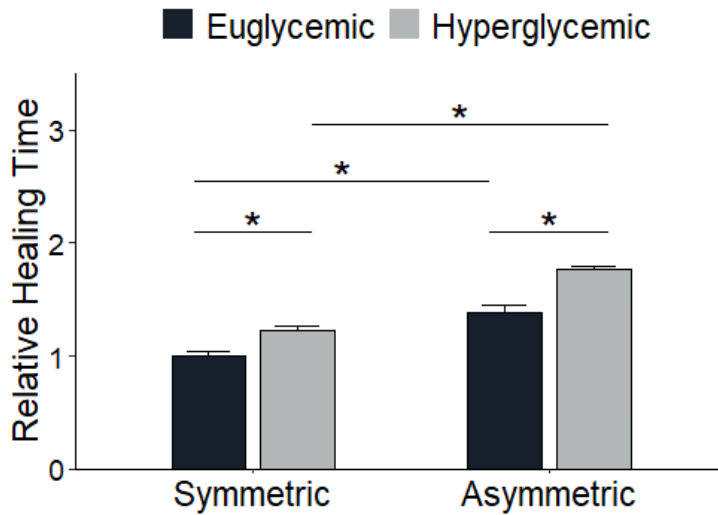
*Figure 6-6 Influence of symmetry and glycemic conditions on small dermal wound healing times. * p<0.05; error bars represent standard error of the mean*

Asymmetric small wounds healed significantly slower than symmetric small wounds – both in euglycemic (p=0.00187) and hyperglycemic (p=0.000187) conditions. Further, small wounds in hyperglycemic conditions closed significantly slower than those in euglycemic conditions – this was observed for both symmetric (p=0.0347) and asymmetric (p=0.00187) geometries. These effects are illustrated in Figure 6-6.

To ascertain which factor had the stronger effect, the effect sizes were determined using the respective 95% CI GES values. It was found that for small dermal wounds, symmetry had a 1.5x stronger influence on healing times –

which is in contrast with large wounds where glycemic conditions had the stronger influence.

6.3.7 Large wound healing rates comparison

Wound healing rates for large symmetric and asymmetric wounds in euglycemic and hyperglycemic conditions were calculated using the healing times and the respective wound areas. The data were homoscedastic, as determined by Levene's test (p=0.486). The influence of symmetry and glycemic conditions on large dermal wound healing rates was analyzed using two-way ANOVA. Both symmetry and glycemic condition were found to have significant effects on large wound healing rates (p=0.00019 and 0.000000128 respectively). However, a significant interaction between the variables was found (p=0.005). Hence, a simple main effects analysis was performed, followed by simple pairwise comparisons using estimated marginal means. This was done twice, first with data grouped by glycemic conditions and then with data grouped by symmetry – in order to parse out the significant effects. Significance was established at an adjusted p-value < 0.025.
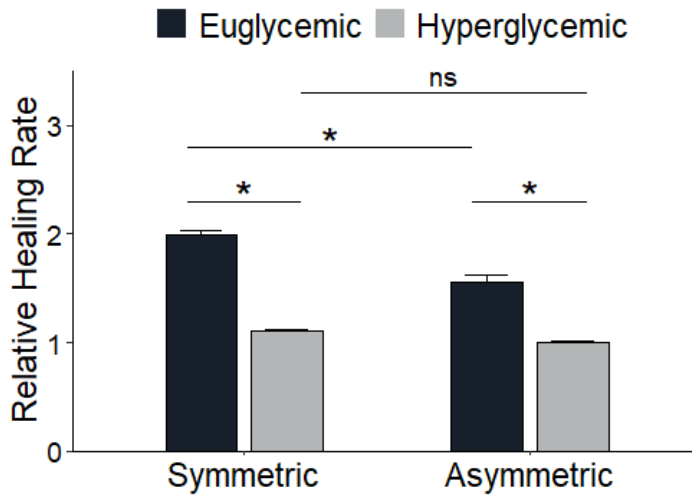
Figure 6-7 Influence of symmetry and glycemic conditions on large dermal wound healing rates. * p<0.025; error bars represent standard error of the mean

Wound symmetry had a significant effect on healing rates of large wounds in euglycemic conditions, with significantly lower healing rates associated with asymmetric wounds (adjusted p=0.00008) but not in hyperglycemic conditions (adjusted p=0.104). On the other hand, glycemic conditions had a significant effect on healing rates of large wounds regardless of symmetry (p=0.0000004 and 0.000013 for symmetric and asymmetric wounds respectively), with significantly lower healing rates associated with hyperglycemia. These effects are illustrated in Figure 6-7.

6.3.8 Small wound healing rates comparison

Wound healing rates for small symmetric and asymmetric wounds in euglycemic and hyperglycemic conditions were calculated using the healing times and the respective wound areas. The data were homoscedastic, as determined by Levene's test ($p=0.556$). The influence of symmetry and glycemic conditions on small dermal wound healing rates was analyzed using two-way ANOVA. Both symmetry and glycemic condition were found to have significant effects on small wound healing times ($p=0.00000294$ and 0.000039 respectively). No significant interaction between the variables was found ($p=0.589$). Tukey's test with Bonferroni corrected α was performed for pairwise comparisons.

Symmetric small wounds had significantly higher healing rates compared to asymmetric small wounds, in both euglycemic ($p=0.00013$) and hyperglycemic ($p=0.00025$) conditions. Further, small wounds in hyperglycemic conditions had significantly lower healing rates – this was observed for both symmetric ($p=0.00126$) and asymmetric ($p=0.00301$) geometries.

To ascertain which factor had the stronger effect, the effect sizes were determined using the respective 95% CI GES values. It was found that for small dermal wounds, symmetry had a 1.4x stronger influence on healing rates.
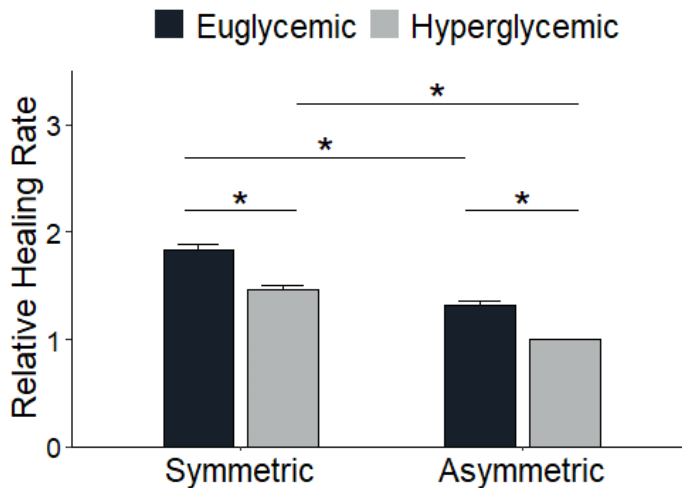
Figure 6-8 Influence of symmetry and glycemic conditions on small dermal wound healing times; error bars represent standard error of the mean

6.4 Discussion

A novel laser direct write photoablation based wound healing technique was developed to create wounds of any given geometry in cell layers. This technique was utilized to perform novel assays to elucidate the simultaneous influence of wound geometry and glycemic conditions on dermal wound healing, which recapitulated clinical observations that inspired the hypotheses for this study. Symmetric dermal wounds displayed higher healing rates compared to asymmetric wounds, even after controlling for glycemic conditions and wounds in euglycemic conditions healed faster than those in hyperglycemic conditions regardless of geometry.

116

Additionally, by repeating the assay for two different wound sizes, it was demonstrated that for smaller wounds, symmetry dominates over glycemic condition whereas for larger wounds, glycemic condition dominates over wound geometry. It would be interesting to study if this phenomenon is observed *in vivo* or in the clinic. If so, it could potentially serve as a benchmark for future wound healing studies and allow for testing therapeutic interventions. Such insights would not have been possible with *in vitro* wound healing assays that offer little control wound geometry.

Other future work could include developing a predictive model of wound healing for diabetic patients based on mapping of their wound geometry and creating that geometry *in vitro*. Perhaps the dependance of wound healing rates on symmetry could be used to improve clinical interventions such as stitching and suturing patterns for serious wounds.

In the nearer term, translating this assay to a 3D multilayered skin model would be interesting. Given the dependence of wound healing rates on geometry, incorporating biomechanical variables such extracellular matrix stiffness would be pertinent. Finally, a laser photoablated wound on a chip model comprising physiologic cues and vascular fluid flow would be a compelling next step, as it would also allow for testing of localized therapies to accelerate wound healing.

6.5   Materials and Methods

Laser spot size characterization

A glass slide was coated with permanent marker ink and loaded on the substrate stage. The laser was focused on the slide and fired to ablate the ink. The slide was then imaged under a microscope and the spot size characterized.

Cell culture

BJ CRL-2522 human dermal fibroblasts (ATCC, Manassas VA) were cultured in RPMI supplemented with 10% FBS, 1% HEPES, 1% L-glutamine, 1% sodium pyruvate and 1% antibiotic-antimycotic. Hyperglycemic conditions were simulated by increasing D-glucose concentration to 50mM. (All reagents from Thermo Fisher Scientific, Waltham MA; FBS from Cytiva, Marlborough MA).

Motion control codes for laser ablation paths

Symmetric (square) and asymmetric wound geometries were designed in two sizes with area of 1mm^2 and 9mm^2. The sketches were overlaid with a grid with unit cell of the characterized laser spot size, 300um. Laser spot paths were

created in a meandering pattern with 50% overlap between adjacent paths. The motion control codes for these paths were compiled into G-code and programmed into the laser direct write CAD/CAM controller.

Laser photoablation of wounds

The laser was warmed up by firing 2000 pulses at 20Hz and then 5000 pulses at 100Hz with maximum voltage applied to the electrodes (15kV). The discharge voltage was adjusted to attain a fluence of $0.31J/cm^2$ for a spot size of 300um.

Media was aspirated from the test dish and the dish was placed on the substrate stage. The substrate stage was raised to focus the laser beam on the interface of the thin film of media. The motion control code was executed synchronized with the laser pulsing. If photoablation did not start occurring, the laser discharge voltage was increased in small increments until it did, the threshold ablation fluence was noted. The substrate stage was lowered and the test dish removed. Next, the above procedure was repeated for the assay dish, with the laser fluence set slightly above the ablation threshold for the respective cell layers. Upon completion, the substrate was lowered and the assay dish dismounted. The media was then replenished and the dish transferred to the incubator.

Symmetric and asymmetric wounds of both sizes, to be cultured in euglycemic and hyperglycemic conditions were photoablated, with one wound per dish.

Imaging and characterization

Photoablated wounds were imaged every 12 hours. At the first timepoint, wound areas were measured and recorded. Wounds were considered fully healed when confluence was attained in the wound area and there was no change in the morphology of the cell layer on two consecutive readings, and then the first of those two readings was considered as the healed timepoint. The wound closure rate was calculated based on the time taken to fully heal and the initial wound area.

Statistical analysis

Each wound was independent i.e., one wound per dish. All experiments were performed in triplicate (n = 3). Since large wounds would obviously take longer than small wounds to heal, the dataset was partitioned into two, two-factor datasets based on wound size, to avoid the size confounding the other effects. Statistical analyses were performed using two-way ANOVA and Bonferroni corrected $p < 0.05$ was considered significant (i.e. significance level α = 95%). The p-value was adjusted accordingly using simple main effects analysis

(grouped both ways) if significant interactions were present between the variables. Pairwise comparisons were performed using Tukey's test with Bonferroni correction when there were no interactions between variables, and using estimated marginal means for simple main effects pairwise analysis when the variables were found to interact. Effect sizes were expressed as generalized eta squared (GES) values with 95% confidence intervals. All analyses were performed in R.

Illustrations

Illustrations were created using BioRender.

7 Decoupling Proliferation and Migration in Wound Healing Assays

7.1 Introduction

Traditional scratch tests lack standardization due to adequate control over wound geometry. Moreover, they do not account for cell proliferation occurring alongside migration – instead relying on the assumption that negligible proliferation occurs in low serum conditions or over the assay timescale. However, cell proliferation continues to occur at finite rates even in serum-starved conditions and hence needs to be taken into account when evaluating cell migration in scratch assays.

Herein, a novel scratch assay was developed that combined highly precise laser direct write photoablation with a reaction-diffusion based mathematical model solved in compact asymptotic initial conditions to account for cell proliferation. This would allow for decoupling the contributions of cell migration and proliferation to scratch closure and provide more accurate insights into cell motility. This assay was then biologically validated to elucidate the influence of the presence of stromal cells on triple negative breast cancer cell migration and proliferation using patient and patient-derived xenograft cells.

7.2 Hypotheses

Laser direct write photoablation can create an experimental model that is suitable to be combined with a mathematical model in order to decouple the contributions of cell proliferation and migration in wound healing assays for a more accurate assessment of a cell type's migratory characteristics.

The following hypothesis was tested as a proof of concept for biological validation of this technique: Cells harvested from metaplastic triple negative breast cancer patient-derived xenografts would display higher migratory (and proliferative) ability compared to cancer cell lines due to presence of the stromal component.

7.3 Results

Traditional wound healing "scratch tests" lack are the most widely used assays for studying cell migration in adherent cells yet lack standardization or consistency with poor control over scratch geometry. Moreover, they operate on the assumption that wound closure was solely due to cell migration and do not account for cell proliferation, which can occur at finite rates even in serum-starved conditions and can thus also contribute to wound closure. Also, many

cell types require a minimal concentration of serum present in the media to maintain viability, and the same serum growth factors also promote proliferation. While some researchers use mitotic inhibitors such as mitomycin C to artificially inhibit cell proliferation, such agents not only fail to suppress proliferation in several cell types but may also alter the cellular physiology, which could lead to misleading outcomes [35] [36]. Further, mitotic inhibitors often act as chemotherapeutic agents for cancer cells, and their presence while screening drugs to inhibit metastasis could confound results.

A natural solution is to utilize a mathematical model to account for cell proliferation. However, such models typically comprise solutions to differential equation with idealized initial and boundary conditions. Since traditional scratch assays do not offer much control over wound geometries, it is difficult to combine their observations accurately with a theoretical model. Hence, a wound creation technique that offers tight control and high precision is needed to create experimental systems that match the initial and boundary conditions of theoretical models. As previously discussed, laser direct write photoablation generates wounds in cell layers with high fidelity, and is hence conducive to generating experimental model systems whose observations can be suitably interpreted in the context of a mathematical model of cell wound closure.

7.3.1 Mathematical model to decouple cell proliferation and migration

The one dimensional Diffusion Equation was a natural choice to model cells infiltrating a wound of a defined width:

$$\frac{\partial c}{\partial t} = D \frac{\partial^2 c}{\partial x^2}$$

Where c(x,t) is the cell density as a function of position and time, D is the diffusivity

However, to account for cell proliferation a source term needed to be included to the linear diffusion/dispersion term on the right side of the Diffusion Equation, resulting in the Reaction-Diffusion Equation:

$$\frac{\partial c}{\partial t} = D \frac{\partial^2 c}{\partial x^2} + f(c)$$

Given the finite wound width, a logistic population growth expression serves as an appropriate source term. The logistic equation takes the form:

$$f(n) = r(1 - \frac{n}{N})n$$

Where r is the linear reproductive rate, N the overall carrying capacity.

Hence, when adapted to cell proliferation, the Reaction-Diffusion equation becomes the Fisher-Kolmogorov-Petrovsky-Piscoumov equation [37] [38] :

$$\frac{\partial c}{\partial t} = D \frac{\partial^2 c}{\partial x^2} + k(c_o - c)c$$

Where c_o is the confluent cell density, kc_o is the intrinsic growth rate of the cells i.e. the maximum rate at which the cells proliferate.

Given the nature of cell division, with each cell producing two daughter cells, the maximum rate of proliferation according to the cell growth equation:

$$kc_o = \frac{ln2}{t_D}$$

Where t_D is the doubling time.

The solution of the Fisher-KPP equation for initial conditions with compact support asymptote comprises of traveling waves of concentration (in this case, cell density) [37] [38] [39]. The speed of these waves i.e., the rate of wound closure by an injured cell layer is uniform and described by:

$$v = 2\sqrt{c_o kD}$$

Substituting in the cell proliferation rate:

$$v = 2\sqrt{\frac{Dln2}{t_D}}$$

126

Rearranging,

$$D = \frac{v^2 t_D}{4 ln2}$$

Diffusivity has dimensions of length^2/time and is a measure of how efficiently cells disperse from areas of high density (confluent regions) to low density (the wound/scratch). This quantity can hence serve as a good measure for cancer invasiveness and metastasis, as well as cell infiltration into wounds. Importantly, the expression for D also takes into account the contribution of cell proliferation to wound closure when quantifying cell motility. Traditional scratch assays, on the other hand, only look at the rate of wound closure, v.

The fact that this mathematical model relies on the one dimensional traveling wave solution of the Fisher-KPP equation (with the scratch width the dimension in question), leads to a couple of important considerations about designing a suitable experimental model system. First, the traveling wave solution evolves from initial conditions with compact support asymptote, meaning that the function is nonzero only within a closed and bounded space. Hence, the experimental system needs to have scratches of consistently uniform widths for it to be compatible with this mathematical model. Conventional scratch assay techniques do not offer sufficient control to achieve this and laser photoablation is hence advantageous. Second, for the scratches to effectively be considered one-dimensional, their lengths need to be much greater than their widths. The

laser direct write photoablation motion control codes were designed with this in mind.

7.3.2 Study design

To biologically validate this assay, the migratory (and proliferative) characteristics of cells from breast cancer patient-derived xenografts were compared to those of breast cancer patient-derived cell line and a regular TNBC cell line.

To obtain patient-derived xenograft (PDX) cells, sections of a mastectomy specimen from a patient that had triple negative metaplastic breast cancer and was unresponsive to conventional treatment were implanted bilaterally into the mammary fat pads of immunodeficient mice, propagated over multiple passages in different mice, and the tumors subsequently harvested [40]. Cells from the same patient mastectomy were also passaged *in vitro* until a finished monoculture of adherent cancer cells (lacking stromal cells) was achieved, to establish a patient-derived triple negative metaplastic cell line (4IC) [41]. These methods are schematically depicted in Figure 7-1. The standard TNBC cell line MDA MB-231 was also used.
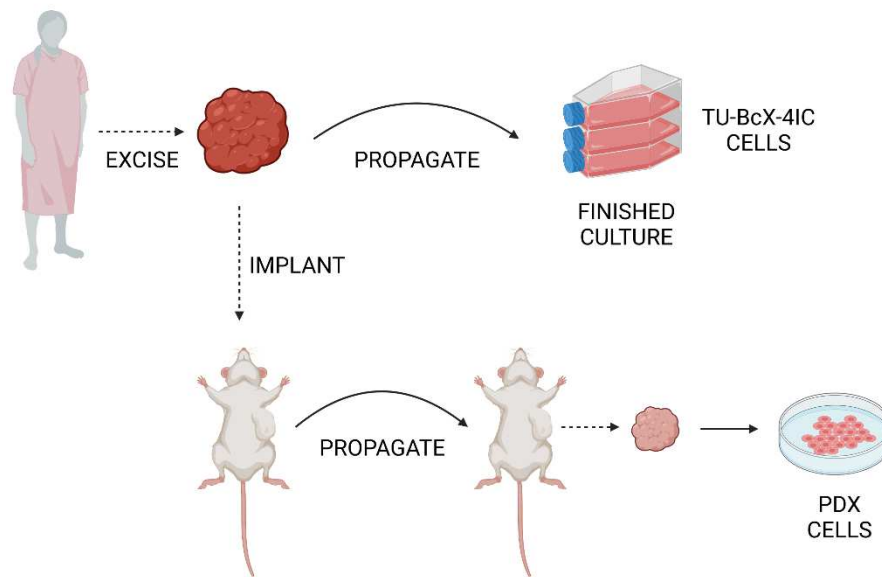
Figure 7-1 Simplified schematic of the process to generate the 4IC cell line and PDX cells using a mastectomy specimen from a patient with treatment-resistant metaplastic triple negative breast cancer

Scratches of two widths (1mm and 2mm) were photoablated in the respective cell layers, to ensure that any observed effects were not artifacts of a specific wound size. Each ablated scratch was independent i.e. one scratch per dish. The experimental groups are summarized in Table 7-1. The ablated scratches were imaged every 12 hours to begin with and then every 6 hours as they approached closure.

Prior to commencing the assays, the minimum serum concentration required to maintain viability for at least 14 days was determined for the respective cell types. The scratch assay durations were less than 5 days in all cases.

Moreover, to avoid any persistent downstream effects of serum factors during the assay, cells were serum starved for 48 hours prior to photoablating the scratches. For cancer cells, 0.5% FBS was sufficient to maintain viability for at least two weeks. Despite cell proliferation being accounted for by the mathematical model, low serum media was used for this assay because factors present in the serum can mask the effects of cancer-stromal signaling.

A test dish with the same batch and passage of cells cultured in identical conditions was used to determine the threshold fluence before photoablating the scratches in the assay dish.

Table 7-1 Experimental groups for laser direct write photoablated scratch assay combined with mathematical modeling to decouple migration and proliferation

Cell Type	Characteristics	Scratch Width
231	Standard triple negative breast cancer cell line	1mm
		2mm
4IC	Patient-derived metaplastic triple negative breast cancer cell line	1mm
		2mm
PDX	Cells harvested from triple negative metaplastic patient derived breast cancer xenografts	1mm
		2mm

This assay has two parts that were conducted in parallel, using the same batch and passage of cells – the scratch assay to determine the wound closure rate and a proliferation experiment to determine the doubling time of the respective cell type. The scratch closure rate and the doubling time were then used to calculate the diffusivity, as described above.

Experiments were conducted in triplicate (n=3). Statistical analyses were performed using one-way ANOVA and Tukey's test with Bonferroni corrected $p < 0.05$ was considered significant (i.e. significance level $\alpha = 95\%$). Effect sizes were expressed as generalized eta squared (GES) values with 95% confidence intervals.

7.3.3 CAD/CAM laser photoablation of scratches with precise geometry

Motion control codes were developed according to the previously described method. Briefly, the focused laser spot size was characterized and the variable aperture set to result in a 300um focused spot. Scratches 1mm and 2mm wide were designed to have their length far exceed their width (by 3-6x) for them to be effectively considered one dimensional to match the Fisher-KPP model. The sketched scratches were overlaid with a grid of 300um unit cell size. A meandering laser path with 50% overlap between adjacent paths was determined and motion control codes written accordingly. The laser pulse rate

for photoablation was 100Hz and the threshold fluence for ablating cell layers was between 0.31-0.34 J/cm^2. Figure 7-2 illustrates this process and Figure 7-3 and depicts the laser photoablation setup.

All three breast cancer cell types were initially cultured in the standard growth media (DMEM with 10% FBS and other supplements), grown to confluence and then serum-starved in Opti-MEM supplemented with 0.5% FBS, 1% HEPES, 1% L-glutamine, 1% pyruvate, 1% essential amino acids, 1% nonessential amino acids, 1% antibiotic-antimycotic and 0.012% insulin for 48 hours prior to ablation of the scratches. Even though cell proliferation was accounted for with the mathematical model, low serum media was used for this assay because factors present in serum can mask interactions between cancer and stromal cells. Media changes were done with the same frequency across all groups.
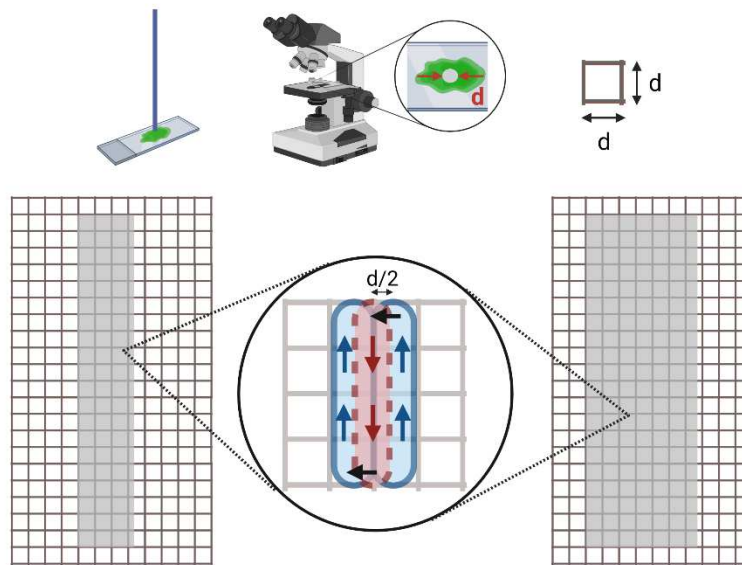
Figure 7-2 Generation of motion control codes for laser photoablation of 1mm and 2mm scratches in cell layers. The characterized focused laser spot size, d, becomes the unit cell of the grid overlay, according to which the codes were written for ablating scratches. A meandering ablative laser spot path with 50% overlap (i.e. d/2) was optimal for precise photoablation and high wound fidelity. d = 300um

To photoablate the scratches, after warming up the laser and setting the laser direct write system parameters, the threshold fluence was determined using the test dish. Next, media was aspirated from the assay dish, laser beam focused on the surface of the media thin film covering the surface of the cell layer, and the scratch ablated by executing the motion control code synchronized with the laser pulsing. Subsequently, the dish was rinsed to remove debris, low serum media was replenished and the dish was transferred to the incubator.
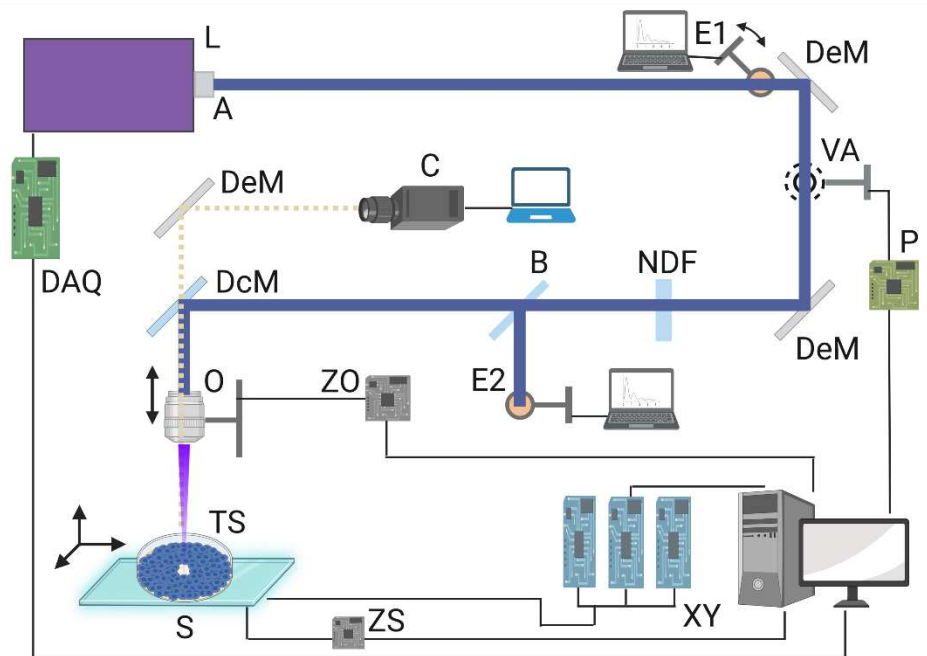
Figure 7-3 The laser direct write photoablation setup (TS: test substrate dish)

1mm and 2mm scratches were photoablated to ensure that any observed effects were not an artifact of a particular wound dimension. The scratches were imaged and their widths were characterized. Widths of scratches of the same intended dimension (1mm or 2mm) were created with a tolerance of 5%. Moreover, even if the cells were fluorescently labeled, the high fidelity and precision offered by the laser direct write photoablation technique due to the highly targeted adherent cell lysis facilitated by the thin media film covering the cell layer – as discussed previously – did not result in photobleaching of cells

adjacent to the laser spot paths. Hence, this ablation technique is compatible

with fluorescently labeled cells. Representative images of 1mm and 2mm wide

scratches in (fluorescently labeled) breast cancer cells are shown in Figure 7-4

and Figure 7-5 (scale bars 500um).
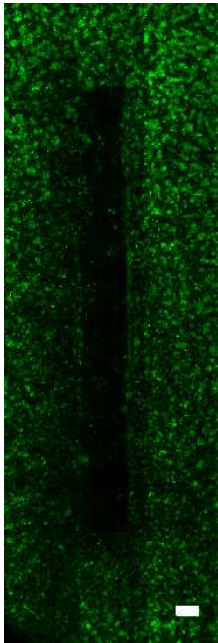
Figure 7-4 Representative image of 1mm wide scratch in a breast cancer cell layer. Scale bar = 500um
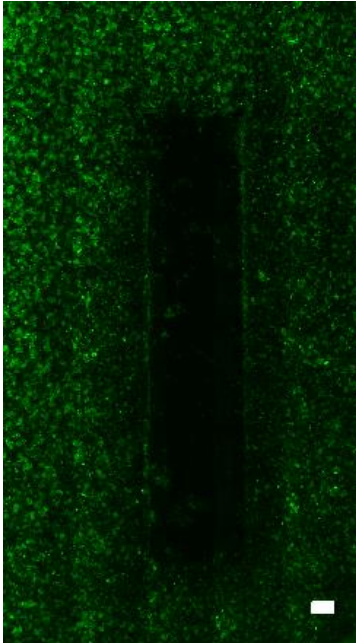
Figure 7-5 Representative image of a 2mm wide scratch in a breast cancer cell layer. Scale bar = 500um

7.3.4 Proliferation assays

Since the expression for calculating diffusivity requires determination of the cell doubling time, proliferation assays were performed in parallel with the scratch assays, using cells from the same batch and passage, and cultured in identical conditions as those that were photoablated.

Approximately 5000-8000 cells were seeded per well in 96 well plates, grown until confluence while being imaged every 12 hours, detached and counted. The time taken to achieve confluence was recorded. Cell counting was done

using an automated cell counter to reduce human error, with trypan blue exclusion of nonviable cells. At least 12 wells per experimental group were seeded to minimize sampling and counting errors.

The doubling time, t_D was determined using the standard cell growth equation:

$$N = N_o e^{Kt}$$

Where N is the final cell count at confluence, N_o is the initial cell count and the intrinsic proliferation rate K is:

$$K = \frac{ln2}{t_D}$$

Once the doubling time was determined, it was combined with the scratch closure rate to calculate diffusivity.

7.3.5 Effect of serum starvation

Conventional scratch assays operate on the basis of the scratch closure occurring entirely due to cell migration. The assumption is that cell proliferation occurs at such negligible rates in serum-starved conditions, that it can be ignored within the timescale of the scratch assay. In order to test this assumption, the proliferation rates of breast cancer cells (from patients, patient-derived xenografts and a standard cell line) were compared in full growth media

and in serum-starved conditions (0.5% FBS) using the method described above. The latter group of cells were serum-starved for at least 48 hours prior to beginning this assay. The data were homoscedastic (Levene's p=0.365,0.330 and 0.564 for 231, 4IC and PDX cells respectively) and were analyzed using unpaired two-tailed t-tests.

The doubling time of 231 cells reduced to 0.23x in low serum conditions (p=0.000445). For 4IC cells, it reduced to was 0.22x (p=0.000244) and for PDX cells, it reduced to 0.59x (p=0.0324). Thus, for each of the cell types, proliferation was significantly slowed in serum-starved conditions compared to full growth media (FG) – as depicted in Figure 7-6, Figure 7-7 and Figure 7-8. However, considering that the absolute values of doubling times for these cell types in FG media ranged from 17-24 hours, cell proliferation not only occurred at a finite rate in serum-starved conditions but doubling times in such conditions ranged from 29-108 hours, which were well within the window of the scratch assays timelines. Hence, ignoring cell proliferation even in serum-starved conditions would lead to misleading conclusions in scratch assays. This attests to the importance of the mathematical model, and by extension, the precise photoablation technique utilized for this study.
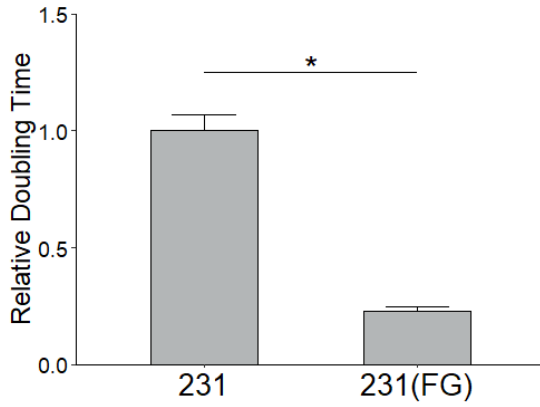
*Figure 7-6 231 cell doubling times in serum-starved vs full growth media conditions. *p<0.05; error bars represent standard error of the mean*
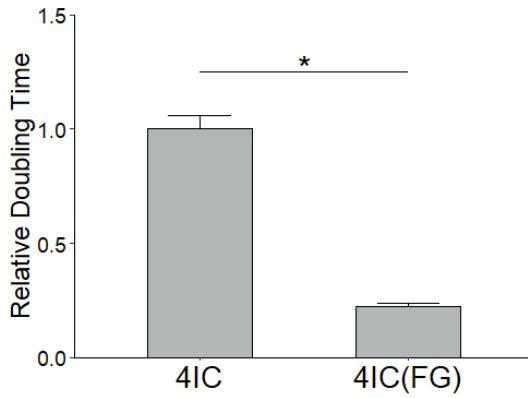
*Figure 7-7 4IC cell doubling times in serum-starved vs full growth media conditions. *p<0.05; error bars represent standard error of the mean*

139
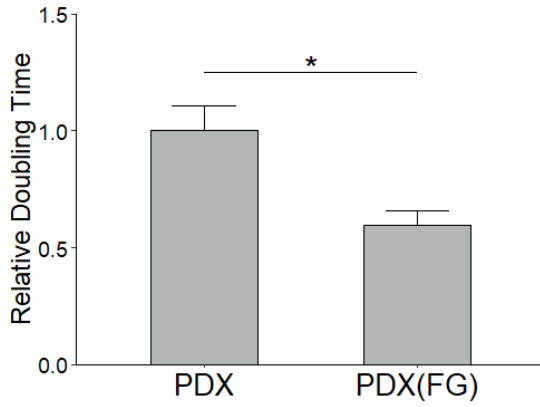
Figure 7-8 PDX cell doubling times in serum-starved vs full growth media conditions. *p<0.05; error bars represent standard error of the mean

7.3.6 Doubling times
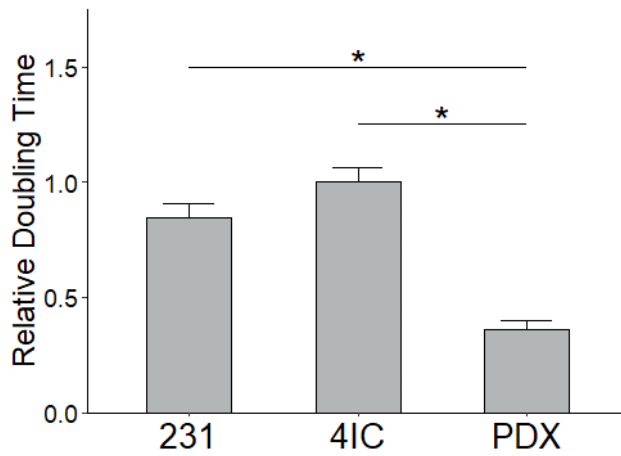
Figure 7-9 Doubling times of 231, 4IC and PDX cells. *p<0.05; error bars represent standard error of the mean

The doubling times of 231, 4IC and PDX cells were compared using one-way ANOVA followed by Tukey's test with Bonferroni correction for pairwise comparisons. The data were homoscedastic (Levene's p=0.907).

In serum-starved conditions, PDX cells proliferated significantly faster than both 231 and 4IC cells (2.35x and 2.77x respectively; p=0.00175 and p=0.000398) – graphically represented in Figure 7-9. This can be attributed to the presence of stromal cells in the PDX cells. It has been shown that mouse stromal cells infiltrate and interact with implanted patient xenografts of triple negative metaplastic breast tumors [40]. Signaling between breast cancer and stromal cells in the tumor microenvironment has been demonstrated to enhance cancer cell proliferation [42].

7.3.7 Diffusivity in photoablated 1mm scratches

Diffusivity was calculated using the rate of closure of 1mm wide scratches and the respective breast cancer cell doubling times. It serves as a measure of cancer cell invasiveness and metastatic potential in the context to the mathematical model.

Diffusivity of the 231, 4IC and PDX cells were compared using one-way ANOVA followed by Tukey's test with Bonferroni correction for pairwise comparisons. Data were homoscedastic (Levene's p=0.176).
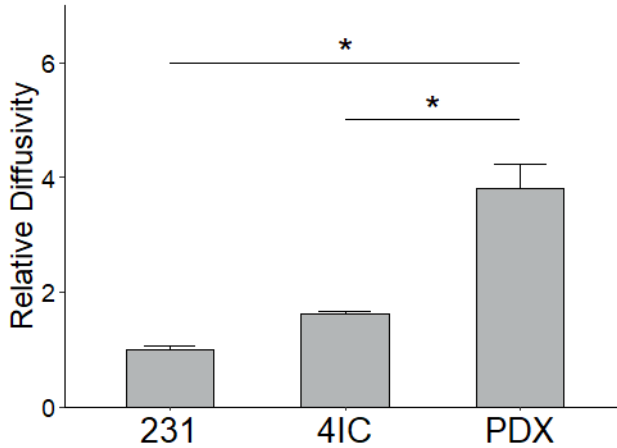
*Figure 7-10 Diffusivity of 231, 4IC and PDX cells in 1mm laser photoablated scratches. *p<0.05; error bars represent standard error of the mean*

Breast cancer cell motility was significantly enhanced in the presence of stromal cells (3.8x more than 231 and 2.36x more than 4IC monocultures, respectively; p=0.000438 and p=0.00168) – graphically represented in Figure 7-10. Crosstalk between breast cancer and stromal cells in the tumor microenvironment has been shown to enhance cancer cell migration and metastasis [42].

7.3.8 Diffusivity in photoablated 2mm scratches

Diffusivity was calculated using the rate of closure of 2mm wide scratches and the respective breast cancer cell doubling times. It serves as a measure of

cancer cell invasiveness and metastatic potential in the context of the mathematical model.

Diffusivity of the 231, 4IC and PDX cells were compared using one-way ANOVA followed by Tukey's test with Bonferroni correction for pairwise comparisons. Data were homoscedastic (Levene's p=0.471).
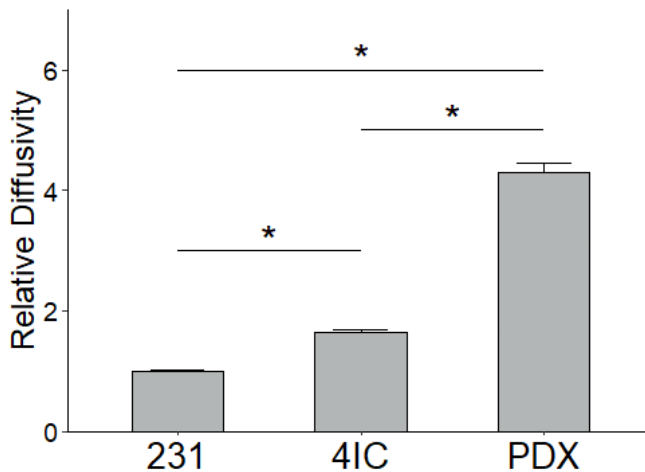
*Figure 7-11 Diffusivity of 231, 4IC and PDX cells in 2mm laser photoablated scratches. *p<0.05; error bars represent standard error of the mean*

The presence of stromal cells significantly enhanced cancer cell diffusivity in both 231 and 4IC cells (4.29x and 2.63x respectively; p = 0.00000115 and p=0.0000033) – graphically represented in Figure 7-11. Since the effects observed in the 1mm side scratch were also observed here, they were not an artifact of the 1mm wound width.

Interestingly, unlike the 1mm scratch, the wider scratch assay also showed increased (1.63x, p=0.0102) motility of 4ICs compared to 231s. This recapitulates *in vivo* animal study as well as clinical observations as metaplastic breast cancer is clinically regarded as being more aggressive and displays increased systemic metastasis compared to non-metaplastic TNBC [40] [43]. Hence, using a wider scratch may reveal cellular characteristics that may be masked in scratches of smaller widths.

7.4 Discussion

A quantitatively rigorous laser photoablated scratch assay was developed that successfully decoupled the influence of breast cancer cell migration and proliferation with and without the presence of stromal cells. The importance of taking into account cell proliferation in wound healing assays was highlighted by the finding that cell proliferation continues to occur even in serum-starved conditions on a timescale similar to the assay duration. Cell diffusivity calculated based on the traveling wave solution of the Fisher-KPP equation is hence an arguably more accurate measure of cell motility than the scratch closure rate.

The assay was biologically validated by testing the hypothesis that stromal signaling enhances breast cancer cell migration and proliferation, a

phenomenon that has been widely reported in literature. Comparing patient-derived xenograft cells, which comprise both cancer and stromal cells, to patient-derived and standard triple negative breast cancer cell lines lacking stromal cells, this assay was able to confirm the hypothesis. Performing this assay with two scratch widths also confirmed that the observed effects were reproducible and not an artifact a particular scratch width.

Future work can include testing the effects of other types of signaling on breast cancer cell metastasis and utilizing other cell types to study different disease states. Therapeutics that target cell motility specifically can also be tested in a more rigorous manner than traditional scratch assays would allow for.

7.5   Materials and Methods

Laser spot size characterization

A glass slide was coated with permanent marker ink and loaded on the substrate stage. The laser was focused on the slide and fired to ablate the ink. The slide was then imaged under a microscope and the spot size characterized.

Cell culture

MDA MB-231 human triple negative breast cancer cells were obtained from ATCC (Manassas, VA).

41C patient-derived metaplastic triple negative breast cancer cells and PDX cells derived from same patient specimen were obtained based on modified versions of previously published protocols by the Burow lab [40] [41]. Briefly, a mastectomy specimen from a 57 year old Caucasian female patient with metastatic breast cancer that was unresponsive to neoadjuvant chemotherapy with combination Adriamycin and cyclophosphamide therapy was procured. The TU-BcX-4IC tumor was dissected and a small tumor explant was plated in a 10 cm petri dish with DMEM supplemented with 10% FBS, 1% HEPES, 1% L-glutamine, 1% pyruvate, 1% essential amino acids, 1% nonessential amino acids, 1% antibiotic-antimycotic and 0.012% insulin (all reagents from Thermo Fisher Scientific, Waltham MA; FBS from Cytiva, Marlborough MA). Cells from the plated tumor were propagated until a finished monoculture of adherent cancer cells, lacking stromal cells, was attained and the TU-BCx-4IC cell line was hence established.

TUBcX-4IC was also propagated in severe combined immunodeficient (SCID)/Beige mice (CB17.cg-PrkdcscidLystbg/ Crl), purchased from Charles River Laboratories (Wilmington, MA) that were 4–6 weeks old weighing approximately 10–18 g. The freshly procured tumor specimen was sectioned in 5 × 5 mm pieces under sterile conditions and encapsulated in a layer of Matrigel (Corning Life Sciences, Tewksbury MA) to improve of engraftment in the mouse. TU-BcX-4IC sections were implanted bilaterally into the mammary fat

pads of female SCID/ Beige mice under general anesthesia (mixture of isoflurane and oxygen). Tumors were measured biweekly using digital calipers. Once the tumor volume reached 1000 mm^3, TU-BcX-4IC was harvested and serially passaged into a new mouse. To passage PDX tumors, mice were euthanized with CO_2 followed by cervical dislocation. Mice were given subcutaneous injections of melocixam (5 mg/kg/day) before surgery. Tumors were removed, dissected into 5 × 5 mm pieces, coated with Matrigel and transplanted bilaterally into another female SCID/Beige mouse under isoflurane anesthesia with oxygen.

Treated tumor explants were harvested after 72 hours. Explants were first minced using a scalpel in a 10cm dish and then enzymatically digested using 0.5mL of 50ug/mL DNase and 1mL of 10mg/mL collagenase type IV on a rotary shaker for 1 hour. Next, the mixture was strained into centrifuge tubes, washing the dish with cold (4C) media and then centrifuged at 1200prm for 6 minutes. The PDX cells were then resuspended in desired concentrations and plated for *in vitro* culture. Before utilizing the cells for experiments, they were allowed to culture for several days, while rinsing with fresh media once a day to remove any suspended mouse red blood cells and attaining a culture of only adherent PDX cells.

All cancer cells were cultured in DMEM supplemented with 10% FBS, 1% HEPES, 1% L-glutamine, 1% pyruvate, 1% essential amino acids, 1%

nonessential amino acids, 1% antibiotic-antimycotic and 0.012% insulin. (All reagents from Thermo Fisher Scientific, Waltham MA; FBS from Cytiva, Marlborough MA).

Cells were serum-starved 48 hours prior to commencing the scratch assays in Opti-MEM supplemented with 0.5% FBS, 1% HEPES, 1% L-glutamine, 1% pyruvate, 1% essential amino acids, 1% nonessential amino acids, 1% antibiotic-antimycotic and 0.012% insulin.

Motion control codes for laser ablation paths

Scratches with widths of 1mm and 2mm and a length of 6mm were sketched out and the sketches were overlaid with a grid with unit cell of the characterized laser spot size, 300um. Laser spot paths were created in a meandering pattern with 50% overlap between adjacent paths. The motion control codes for these paths were compiled into G-code and programmed into the laser direct write CAD/CAM controller.

Laser photoablation of scratches

The laser was warmed up by firing 2000 pulses at 20Hz and then 5000 pulses at 100Hz with maximum voltage applied to the electrodes (15kV). The

discharge voltage was adjusted to attain a fluence of $0.31J/cm^2$ for a spot size of 300um.

Media was aspirated from the test dish and the dish was placed on the substrate stage. The substrate stage was raised to focus the laser beam on the interface of the thin film of media. The motion control code was executed synchronized with the laser pulsing. If photoablation did not start occurring, the laser discharge voltage was increased in small increments until it did, the threshold ablation fluence was noted. The substrate stage was lowered and the test dish removed. Next, the above procedure was repeated for the assay dish, with the laser fluence set slightly above the ablation threshold for the respective cell layers.

1mm and 2mm scratches were photoablated in 231, 4IC and PDX cell layers, with one scratch per dish.

Cell proliferation assays

Approximately 5000-8000 cells were seeded per well in 96 well plates, grown until confluence while being imaged every 12 hours, detached and counted. The time taken to achieve confluence was recorded. Cell counting was done using an automated cell counter to reduce human error, with trypan blue exclusion of nonviable cells. At least 12 wells per experimental group were

seeded to minimize sampling and counting errors. The doubling time was calculated using the standard cell growth equation.

Imaging and characterization

Photoablated scratches were imaged every 12 hours to begin with and then every 6 hours as they approached closure. At the first timepoint, the scratch width was measured and recorded. Scratches were considered fully closed when confluence was attained in the wound area and there was no change in the morphology of the cell layer on two consecutive readings, and then the first of those two readings was considered as the healed timepoint. The scratch closure rate was determined based on closure time and initial width, and was subsequently used to calculate the cellular diffusivity using on the traveling wave solution of the Fisher-KPP equation.

Statistical analysis

Each scratch was independent i.e., one scratch per dish. All experiments were performed in triplicate (n = 3). Statistical analyses were performed using one-way ANOVA and Tukey's test with Bonferroni corrected $p < 0.05$ was considered significant (i.e. significance level α = 95%). Effect sizes were

150

expressed as generalized eta squared (GES) values with 95% confidence
intervals. All analyses were performed in R.

Illustrations

Illustrations were created using BioRender.

8 Influence of Stromal Signaling on Breast Cancer Metastasis

8.1 Introduction

Metaplastic triple negative breast cancer PDX cells displayed significantly higher motility and proliferation compared to the patient-derived metaplastic triple negative breast cancer cell line using a novel and rigorous scratch assay that allowed for delineation of cell migration and proliferation. A natural follow up was thus to do a dedicated study examining the influence of stromal signaling on both metaplastic and non-metaplastic triple negative breast cancer by applying the same assay to co-cultures with human fibroblasts.

Given the plethora of chemoattractants in the tumor microenvironment leading to significant redundancy (with likely more chemoattractants that haven't yet been characterized) [44], elucidating metastatic dynamics of cancer cells in response to crosstalk with other cell types could offer more physiologically relevant insights instead of focusing on a specific chemoattractant.

8.2 Hypothesis

The previous study provided evidence of stromal cells enhancing motility and

proliferation in PDX cells compared to triple negative breast cancer cell lines using a novel laser direct write photoablated scratch assay combined with a mathematical model. Since these findings aligned with *in vivo* animal study and clinical observations, as a next step, the following hypothesis was tested utilizing the same assay: Juxtacrine signaling with fibroblasts in the tumor microenvironment enhances migration and proliferation of breast cancer cells.

8.3 Results

The combination of a novel laser direct write photoablated scratch assay with a reaction-diffusion based mathematical model – that was developed and validated in the previous study – was herein used to analyze the influence of stromal signaling on TNBC growth, invasiveness and metastasis.

8.3.1 Study design

Migratory and proliferative characteristics of TNBC with and without stromal signaling were analyzed using the novel laser photoablated scratch assay described previously.

To simulate the juxtacrine signaling associated with stromal cells in the breast tumor microenvironment, 231 and 4IC cells were co-cultured with human BJ

fibroblasts in a 1:1 ratio by thoroughly homogenizing the cell suspension. The cancer cells and fibroblasts were allowed to co-culture unperturbed for at least 48 hours prior to the serum starving to facilitate the establishment of crosstalk in the co-culture dishes. Proliferation experiments were performed at a higher initial seeding density to ensure juxtacrine signaling between breast cancer cells and fibroblasts in the co-culture groups. The experimental groups are summarized in Table 8-1. Cancer cells and fibroblasts were cultured in serum-starved conditions for this assay, with the media formulation as follows: Opti-MEM supplemented with 0.5% FBS, 1% HEPES, 1% L-glutamine, 1% sodium pyruvate, 1% essential amino acids, 1% nonessential amino acids, 1% antibiotic-antimycotic and 0.012% insulin. Although the mathematical model accounts for cell proliferation, low serum media was used because factors in the serum can mask interactions between cancer cells and fibroblasts. Media changes were performed with the same frequency across all groups.

Experiments were conducted in triplicate (n=3). Statistical analyses were performed using one-way ANOVA and Tukey's test with Bonferroni corrected p< 0.05 considered significant (i.e. significance level α = 95%). Effect sizes were expressed as generalized eta squared (GES) values with 95% confidence intervals.

154

Table 8-1 Experimental groups for photoablated scratch assay to study the effect of stromal signaling on breast cancer migration

Cell Type(s)	Characteristics	Scratch Width
231	Standard triple negative breast cancer cell line	1mm
		2mm
231 + Fib	Standard TNBC cells co-cultured with human BJ fibroblasts	1mm
		2mm
4IC	Patient-derived metaplastic triple negative breast cancer cell line	1mm
		2mm
4IC + Fib	Patient-derived metaplastic TNBC cell line co-cultured with human BJ fibroblasts	1mm
		2mm
PDX	Cells harvested from triple negative metaplastic patient derived breast cancer xenografts	1mm
		2mm

8.3.2 Proliferation assays
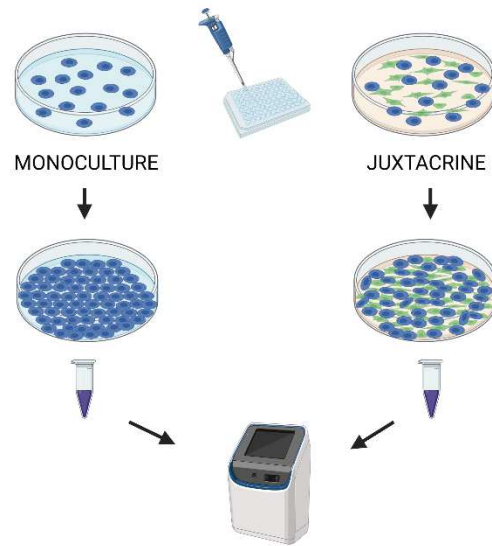
Figure 8-1 Proliferation assays for cancer cell fibroblast co-culture simulating juxtacrine signaling

Proliferation assays were performed and the doubling time was calculated using the methods described previously – with the only modification being the initial cell seeding density for the co-culture groups. In order to assess the influence of juxtacrine stromal signaling on proliferation, cancer cells and fibroblasts were seeded in a thoroughly homogenized suspension at a density of 10-15k of per well (of a 96 well plate), which has a confluence density of 40-45k cells. The higher seeding density ensures cell-cell contact between cancer

cells and fibroblasts in the well yet allows enough room for proliferation. Figure 8-1 illustrates this method.

Data were homoscedastic (Levene's p=0.552). The doubling times of 231 cells, 4IC cells, 231 co-cultured with BJ fibroblasts, 4IC co-cultured with BJ fibroblasts and PDX cells were compared using one-way ANOVA followed by Tukey's test with Bonferroni correction. This is graphically represented in Figure 4-1.

Proliferation was significantly enhanced when 231 or 4IC cells were co-cultured with human fibroblasts (3.89x and 2.62x respectively; p=0.000000176 and 0.00000212) – which can be attributed to cancer-stromal juxtacrine signaling.

The presence of mouse fibroblasts in PDX cells also significantly increased proliferation compared to 4ICs (2.55x p=0.00000251).

Interestingly, when 4IC cells were co-cultured with human fibroblasts, proliferation levels showed no significant difference to those of PDX cells (p=0.999). This suggests that co-culturing patient-derived cells with human fibroblasts could recapitulate the PDX tumor proliferation rate.

231s or 4ICs co-cultured with human fibroblasts displayed similar proliferation proliferation rates (p=0.0611). This mirrored the similar rates of proliferation in 231 and 4IC monocultures (p=0.088) as well.
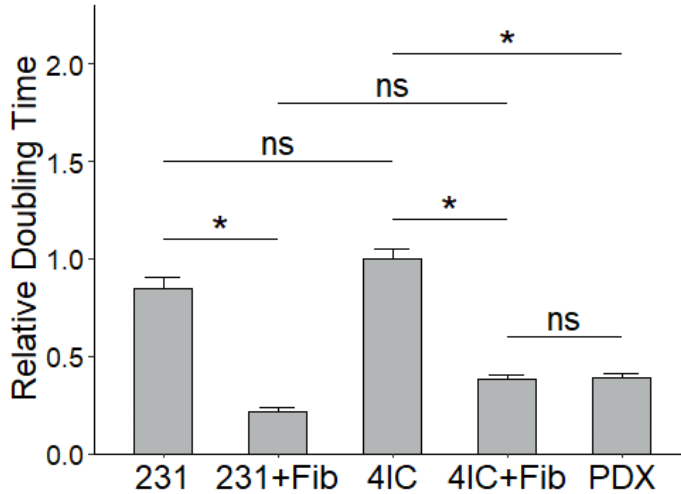
Figure 8-2 Doubling times of 231, 231+fibroblast co-culture, 4IC, 4IC+fibroblast co-culture and PDX cells. *p<0.05; error bars represent standard error of the mean

8.3.3 Diffusivity in photoablated 1mm scratches

Diffusivity was calculated using the rate of closure of 1mm wide laser photoablated scratches and the respective breast cancer cell doubling times. It serves as a measure of cancer cell invasiveness and metastatic potential in the context of the mathematical model.
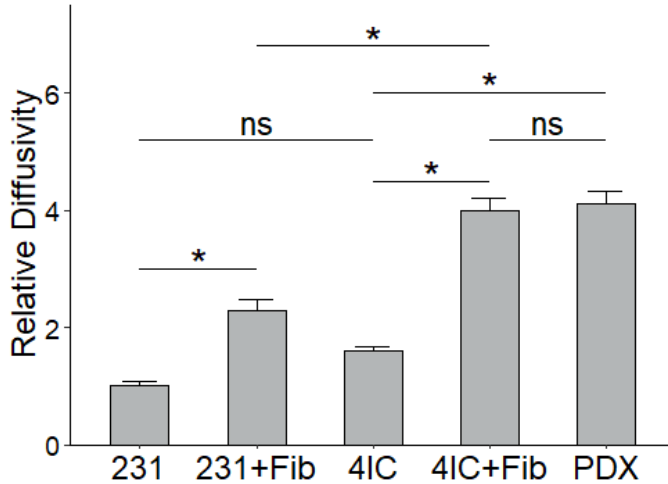
*Figure 8-3 Diffusivity of 231, 231+fibroblast co-culture, 4IC, 4IC+fibroblast co-culture and PDX cells in 1mm laser photoablated scratches. *p<0.05; error bars represent standard error of the mean*

Data were homoscedastic (Levene's p=0.578). The diffusivities of 231 cells, 4IC cells, 231 co-cultured with BJ fibroblasts, 4IC co-cultured with BJ fibroblasts and PDX cells were compared using one-way ANOVA followed by Tukey's test with Bonferroni correction. This is graphically represented in Figure 8-3.

Co-culturing with human stromal cells significantly enhanced diffusivity of both 231 and 4IC cells (2.29x and 2.48x, p=0.0023 and p=0.00000138) – which can be attributed to cancer-stromal juxtacrine signaling.

The presence of mouse stromal cells in PDX-derived cultures also significantly increased diffusivity (2.55x, p=0.00000889).

Interestingly, co-culturing 4IC cells with human fibroblasts resulted in diffusivity which was not significantly different compared to PDX cells (p=0.987). This suggests that co-culturing with human fibroblasts may recapitulate cancer cell migratory properties that patient-derived cells display when implanted *in vivo* as PDXs.

Also, 4ICs co-cultured with human fibroblasts displayed significantly higher diffusivity compared to 231s co-cultured with human fibroblasts (1.74x,p=0.000263), even though the monocultures displayed no significant difference (p=0.159). This suggests that stromal signaling seems to enable the aggressive metastatic migratory behavior of metaplastic TNBC cells.

8.3.4 Diffusivity in photoablated 2mm scratches

Diffusivity was calculated using the rate of closure of 2mm wide laser photoablated scratches and the respective breast cancer cell doubling times. It serves as a measure of cancer cell invasiveness and metastatic potential in the context of the mathematical model.
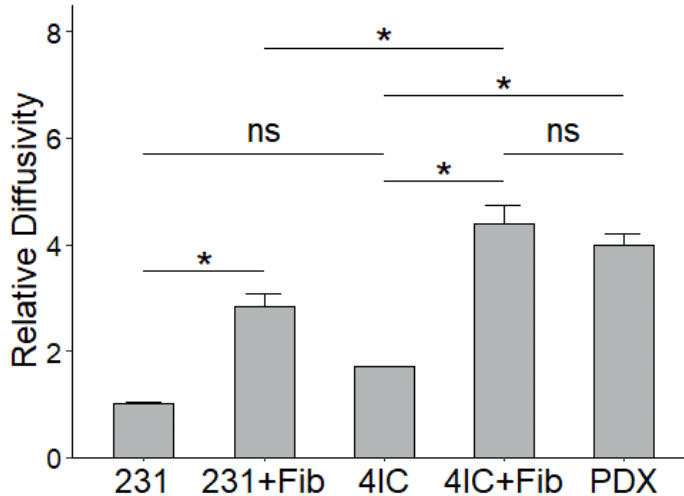
Figure 8-4 Diffusivity of 231, 231+fibroblast co-culture, 4IC, 4IC+fibroblast co-culture and PDX cells in 2mm laser photoablated scratches. *p<0.05; error bars represent standard error of the mean

Data were homoscedastic (Levene's p=0.385). The diffusivities of 231 cells, 4IC cells, 231 co-cultured with BJ fibroblasts, 4IC co-cultured with BJ fibroblasts and PDX cells were compared using one-way ANOVA followed by Tukey's test with Bonferroni correction. This is graphically represented in Figure 8-4.

Co-culturing with human stromal cells significantly enhanced diffusivity of both 231 and 4IC cells (2.83x and 2.58x, p=0.000927 and p=0.0000375) – which can be attributed to cancer-stromal juxtacrine signaling.

The presence of mouse stromal cells in PDX-derived cultures also significantly increased diffusivity (2.58x, p=0.000152).

Interestingly, co-culturing 4IC cells with human fibroblasts resulted in diffusivity which was not significantly different compared to PDX cells (p=0.69). This suggests that co-culturing with human fibroblasts may recapitulate cancer cell migratory properties that patient-derived cells display when implanted *in vivo* as PDXs.

Also, 4ICs co-cultured with human fibroblasts displayed significantly higher diffusivity compared to 231s co-cultured with human fibroblasts (1.55x,p=0.00329), even though the monocultures displayed no significant difference (p=0.221). This suggests that stromal signaling seems to enable the aggressive metastatic migratory behavior of metaplastic TNBC cells.

Since all of the effects that were observed in the 1mm scratch were also observed here, they were not an artifact of the 1mm wound width.

8.4 Discussion

This study serves as proof-of-principle that the novel scratch assay combining CAD/CAM laser photoablation with a theoretical model to decouple the contributions of cell motility and proliferation to wound closure, can also lead to novel biological insights. Not only was it demonstrated that juxtacrine signaling with fibroblasts enhances proliferation and migration in triple negative breast cancer cells – which aligns with prior results from literature which inspired the

initial hypothesis – but it was also shown that co-culturing breast cancer cell lines with human fibroblasts *in vitro* recapitulates the enhanced proliferative and migratory characteristics observed in PDX cells. Gene expression studies suggest that mouse stromal cells infiltrate PDXs and take over some over some functions of patient's stromal cells when the tumor is implanted into mice resulting in increased metastasis [40], and the findings from this study suggest that co-culturing patient cells with human fibroblasts *in vitro* may also elicit similar behavior from metaplastic triple negative breast cancer cells. It would be interesting to investigate this further, as it could aid in the development of advanced *in vitro* models to reduce dependance on animal models in the future. Also, going forward, patient-specific predictive models for the likelihood of distant metastasis could be developed by utilizing their cells in a co-culture. Therapeutic interventions that aim to disrupt tumor-stromal crosstalk could also be tested to check if they reduce the migratory potential of cancer cells.

Other future work could include extending this assay to a 3D model of the breast tumor microenvironment and/or to a microphysiolgical system incorporating vascular flow to gain further insight into cancer cell intravasation in response to stromal signaling.

8.5 Materials and Methods

Laser spot size characterization

A glass slide was coated with permanent marker ink and loaded on the substrate stage. The laser was focused on the slide and fired to ablate the ink. The slide was then imaged under a microscope and the spot size characterized.

Cell culture

MDA MB-231 human triple negative breast cancer cells were obtained from ATCC (Manassas, VA).

41C patient-derived metaplastic triple negative breast cancer cells and PDX cells derived from same patient specimen were obtained based on modified versions of previously published protocols by the Burow lab [40] [41]. Briefly, a mastectomy specimen from a 57 year old Caucasian female patient with metastatic breast cancer that was unresponsive to neoadjuvant chemotherapy with combination Adriamycin and cyclophosphamide therapy was procured. The TU-BcX-4IC tumor was dissected and a small tumor explant was plated in a 10 cm petri dish with DMEM supplemented with 10% FBS, 1% HEPES, 1% L-glutamine, 1% pyruvate, 1% essential amino acids, 1% nonessential amino acids, 1% antibiotic-antimycotic and 0.012% insulin (all reagents from Thermo Fisher Scientific, Waltham MA; FBS from Cytiva, Marlborough MA). Cells from

164

the plated tumor were propagated until a finished monoculture of adherent cancer cells, lacking stromal cells, was attained and the TU-BCx-4IC cell line was hence established.

TUBcX-4IC was also propagated in severe combined immunodeficient (SCID)/Beige mice (CB17.cg-PrkdcscidLystbg/ Crl), purchased from Charles River Laboratories (Wilmington, MA) that were 4–6 weeks old weighing approximately 10–18 g. The freshly procured tumor specimen was sectioned in 5 × 5 mm pieces under sterile conditions and encapsulated in a layer of Matrigel (Corning Life Sciences, Tewksbury MA) to improve of engraftment in the mouse. TU-BcX-4IC sections were implanted bilaterally into the mammary fat pads of female SCID/ Beige mice under general anesthesia (mixture of isoflurane and oxygen). Tumors were measured biweekly using digital calipers. Once the tumor volume reached 1000 mm^3, TU-BcX-4IC was harvested and serially passaged into a new mouse. To passage PDX tumors, mice were euthanized with CO_2 followed by cervical dislocation. Mice were given subcutaneous injections of melocixam (5 mg/kg/day) before surgery. Tumors were removed, dissected into 5 × 5 mm pieces, coated with Matrigel and transplanted bilaterally into another female SCID/Beige mouse under isoflurane anesthesia with oxygen.

Treated tumor explants were harvested after 72 hours. Explants were first minced using a scalpel in a 10cm dish and then enzymatically digested using

0.5mL of 50ug/mL DNase (Qiagen, Germantown MD) and 1mL of 10mg/mL collagenase type IV (Thermo Fisher Scientific, Waltham MA) on a rotary shaker for 1 hour. Next, the mixture was strained into centrifuge tubes, washing the dish with cold (4C) media and then centrifuged at 1200prm for 6 minutes. The PDX cells were then resuspended in desired concentrations and plated for *in vitro* culture. Before utilizing the cells for experiments, they were allowed to culture for several days, while rinsing with fresh media once a day to remove any suspended mouse red blood cells and attaining a culture of only adherent PDX cells.

All cancer cells were cultured in DMEM supplemented with 10% FBS, 1% HEPES, 1% L-glutamine, 1% pyruvate, 1% essential amino acids, 1% nonessential amino acids, 1% antibiotic-antimycotic and 0.012% insulin. (All reagents from Thermo Fisher Scientific, Waltham MA).

Cells were serum-starved 48 hours prior to commencing the scratch assays in Opti-MEM supplemented with 0.5% FBS, 1% HEPES, 1% L-glutamine, 1% pyruvate, 1% essential amino acids, 1% nonessential amino acids, 1% antibiotic-antimycotic and 0.012% insulin.

Motion control codes for laser ablation paths

Scratches with widths of 1mm and 2mm and a length of 6mm were sketched out and the sketches were overlaid with a grid with unit cell of the characterized laser spot size, 300um. Laser spot paths were created in a meandering pattern with 50% overlap between adjacent paths. The motion control codes for these paths were compiled into G-code and programmed into the laser direct write CAD/CAM controller.

Laser photoablation of scratches

The laser was warmed up by firing 2000 pulses at 20Hz and then 5000 pulses at 100Hz with maximum voltage applied to the electrodes (15kV). The discharge voltage was adjusted to attain a fluence of $0.31J/cm^2$ for a spot size of 300um.

Media was aspirated from the test dish and the dish was placed on the substrate stage. The substrate stage was raised to focus the laser beam on the interface of the thin film of media. The motion control code was executed synchronized with the laser pulsing. If photoablation did not start occurring, the laser discharge voltage was increased in small increments until it did, the threshold ablation fluence was noted. The substrate stage was lowered and the test dish removed. Next, the above procedure was repeated for the assay dish,

with the laser fluence set slightly above the ablation threshold for the respective cell layers.

1mm and 2mm scratches were photoablated in 231, 4IC and PDX cell layers, with one scratch per dish.

Cell proliferation assays

In order to assess the influence of juxtacrine stromal signaling on proliferation, cancer cells and fibroblasts were seeded in a thoroughly homogenized suspension at a density of 10-15k of per well (of a 96 well plate), which has a confluence density of 40-45k cells. The higher seeding density ensures cell-cell contact between cancer cells and fibroblasts in the well yet allows enough room for proliferation. The cells were grown until confluence while being imaged every 12 hours, detached and counted. The time taken to achieve confluence was recorded. Cell counting was done using an automated cell counter to reduce human error, with trypan blue exclusion of nonviable cells. At least 12 wells per experimental group were seeded to minimize sampling and counting errors. The doubling time was calculated using the standard cell growth equation.

Imaging and characterization

Photoablated scratches were imaged every 12 hours to begin with and then every 6 hours as they approached closure. At the first timepoint, the scratch width was measured and recorded. Scratches were considered fully closed when confluence was attained in the wound area and there was no change in the morphology of the cell layer on two consecutive readings, and then the first of those two readings was considered as the healed timepoint. The scratch closure rate was determined based on closure time and initial width, and was subsequently used to calculate the cellular diffusivity using on the traveling wave solution of the Fisher-KPP equation.

Statistical analysis

Each scratch was independent i.e., one scratch per dish. All experiments were performed in triplicate ($n = 3$). Statistical analyses were performed using one-way ANOVA and Tukey's test with Bonferroni corrected $p < 0.05$ was considered significant (i.e. significance level $\alpha = 95\%$). Effect sizes were expressed as generalized eta squared (GES) values with 95% confidence intervals. All analyses were performed in R.

Illustrations

Illustrations were created using BioRender.

9 Influence of Adipose Signaling on Breast Cancer Metastasis

9.1 Introduction

Having evaluated the influence of stromal juxtacrine signaling on triple negative breast cancer metastatic characteristics, an interesting next step was to consider elucidating the effects of paracrine signaling using the novel photoablated scratch assay. Obesity is a widely recognized risk factor for developing breast cancer and paracrine signaling with adipose tissue is thought to be play a significant role [45]. Hence, this study aimed to test the effect of obesity on triple negative breast cancer migration and proliferation. Utilizing cancer cells and adipose-derived stem cells harvested from patients increased the physiological relevance of this assay.

9.2 Hypothesis

Considering that obesity is a risk factor for triple negative breast cancer, using the previously developed novel laser photoablation scratch assay, the following hypothesis was tested: Paracrine signaling with obese but not lean adipose tissue enhances the migration and proliferation of breast cancer cells.

9.3 Results

The combination of a novel laser direct write photoablated scratch assay with a reaction-diffusion based mathematical model – that was developed and validated previously – was herein used to analyze the influence of obese and lean adipose signaling on TNBC growth, invasiveness and metastasis.

9.3.1 Study design

Migratory and proliferative characteristics of TNBC in response to crosstalk with obese and lean adipose cells were analyzed using the novel laser photoablated scratch assay described previously.

Human adipose derived stem cells (ASC) were harvested from liposuction aspirations of obese patients (BMI $\geq$ 25kg/m^2) and needle biopsies of lean patients (BMI < 25kg/m^2) [46] [47]. Both cancer cells and ASCs were normally cultured in DMEM supplemented with 10% FBS, 1% HEPES, 1% L-glutamine, 1% sodium pyruvate and 1% antibiotic-antimycotic. To simulate paracrine signaling between ASCs and cancer cells (standard 231 TNBC cell line and 4IC metaplastic TNBC patient-derived cell line), two-way crosstalk conditioned

media was prepared. Using low serum conditioned media was important because serum factors can mask the effects of cancer-adipose interactions.

Cancer cells and ASCs were simultaneously cultured in Opti-MEM – cancer cells in 0.5% FBS and ASCs in 1.5% FBS (with all other supplement concentrations as mentioned above) for 12 hours. Then, half of the ASC media was replaced with cancer conditioned media and the ASCs cultured for 72 hours. Next, half of the ASC crosstalk conditioned media was added back into the cancer cells, diluted 1:1 with fresh serum-free media (i.e. Opti-MEM with all supplements as above but 0% FBS). This protocol recapitulates two-way cancer-adipose crosstalk and results in a 0.5% FBS concentration for the assay, which – according to preliminary testing – is the minimum serum concentration required to keep the cancer cells viable for at least 14 days (assay duration was less than 5 days). Moreover, 1% FBS keeps the ASCs alive for at least a week and thus ASC viability was not affected in this protocol. Conditioned media was filtered via a 0.2um filter at each step to remove debris. A simplified schematic of this process is depicted in Figure 9-1.

The two-way crosstalk conditioned media was used for both the scratch and proliferation assays. Table 9-1 summarizes the experimental groups. Media changes were done with the same frequency across all groups. The photoablation setup is illustrated in Figure 9-2.

173

Experiments were conducted in triplicate (n=3). Statistical analyses were performed using one-way ANOVA and Tukey's test with Bonferroni corrected $p< 0.05$ considered significant (i.e. significance level α = 95%). Effect sizes were expressed as generalized eta squared (GES) values with 95% confidence intervals.
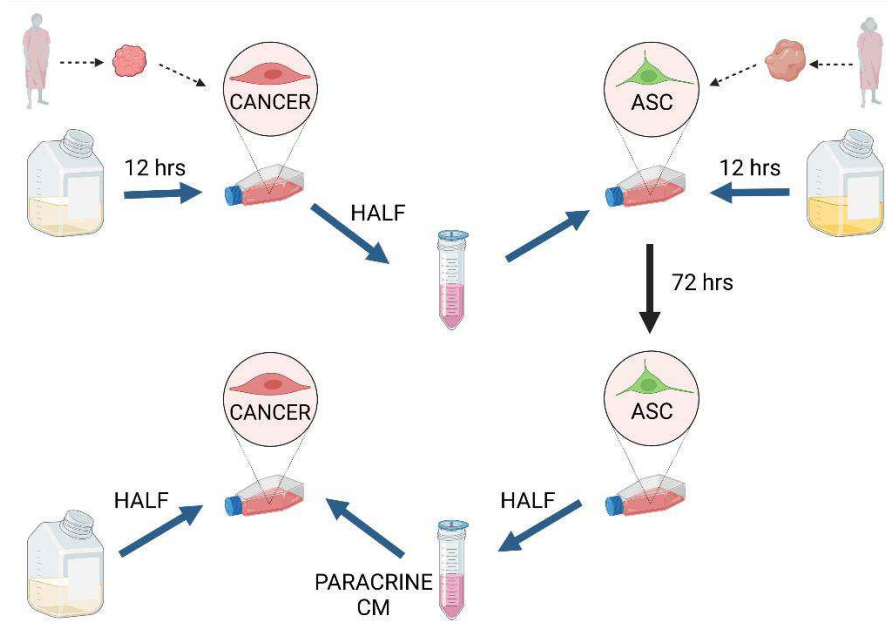
Figure 9-1 Simplified schematic of the preparation of two-way crosstalk ASC conditioned media for photoablated breast cancer scratch assays
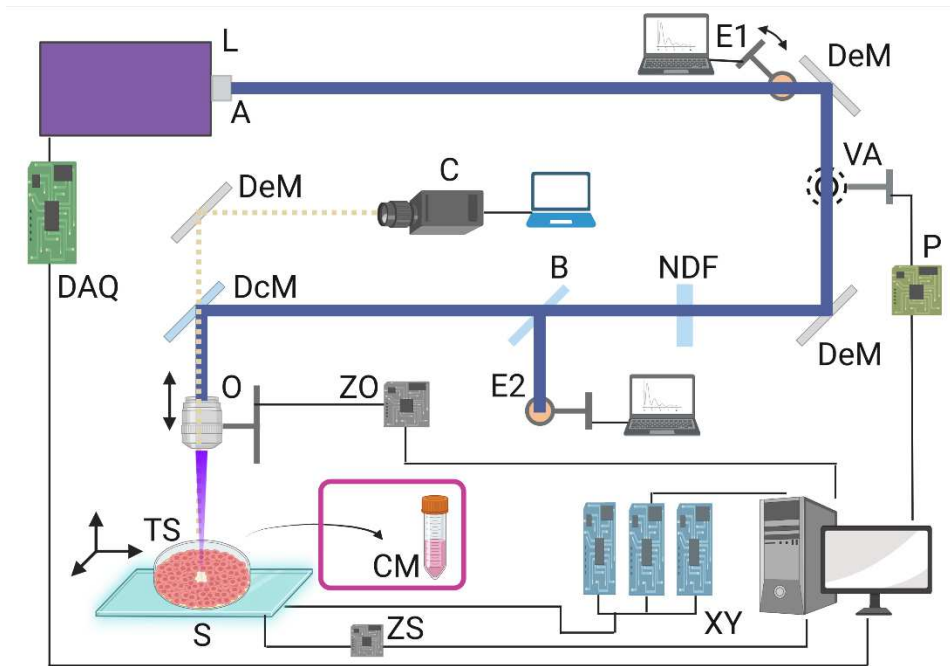
Figure 9-2 The laser direct write photoablation setup for elucidating adipose paracrine signaling in triple negative breast cancer

Table 9-1 Experimental groups for photoablated scratch assay to study the effect of obese and lean adipose signaling on breast cancer migration

Cell Type	Media	Scratch Width
231 (standard TNBC cell line)	Control	1mm
		2mm
231	Obese ASC conditioned media	1mm
		2mm
231	Lean ASC conditioned media	1mm
		2mm
4IC (patient-derived metaplastic TNBC cell line)	Control	1mm
		2mm
4IC	Obese ASC conditioned media	1mm
		2mm
4IC	Lean ASC conditioned media	1mm
		2mm

9.3.2 Proliferation assays

Proliferation assays were performed and the doubling time was calculated using the methods described previously – making sure to use conditioned media in the respective groups.

Data were homoscedastic (Levene's p=0.998). The doubling times of 231 cells, 231 cells cultured in obese adipose conditioned media, 231 cells cultured in lean adipose conditioned media, 4IC cells, 4IC cells cultured in obese adipose conditioned media and 4IC cells cultured in lean adipose conditioned media were compared using one-way ANOVA followed by Tukey's test with Bonferroni correction. This is graphically represented in Figure 9-3.

*Figure 9-3 Doubling times of 231 cells, 231 cells cultured in obese adipose conditioned media, 231 cells cultured in lean adipose conditioned media, 4IC cells, 4IC cells cultured in obese adipose conditioned media and 4IC cells cultured in lean adipose conditioned media. *p<0.05; error bars represent standard error of the mean*

Both 231 and 4IC cancer cells in conditioned media from obese patient ASCs displayed significantly increased proliferation compared to control media (2.71x in 231s p=0.000089; 2.43x in 4ICs p=0.0000325). Cancer cells in conditioned media from lean patient ASCs also displayed significantly increased proliferation compared to control media (1.44x in 231s p=0.0342; 1.34x in 4ICs p=0.0348).

However, obese ASC conditioned media enhanced cancer cell proliferation significantly more than lean ASC conditioned media (1.89x for 231s p=0.0216; 1.81x for 4ICs p=0.00569). This shows that while cancer-adipose crosstalk generally seems to enhance cancer growth, cancer cells are able to utilize obese adipose signaling to increase their proliferation with greater effect.

231s and 4ICs displayed no significant differences in proliferation in either control media (p=0.315), obese ASC CM (p=0.732) or lean ASC CM (p=0.31). For the sake of clarity, the nonsignificant findings were not marked on the graph.

9.3.3 Diffusivity in photoablated 1mm scratches

Diffusivity was calculated using the rate of closure of 1mm wide laser photoablated scratches and the respective breast cancer cell doubling times. It serves as a measure of cancer cell invasiveness and metastatic potential in the context of the mathematical model.

*Figure 9-4 Diffusivity in 1mm laser photoablated scratches of 231 cells, 231 cells cultured in obese adipose conditioned media, 231 cells cultured in lean adipose conditioned media, 4IC cells, 4IC cells cultured in obese adipose conditioned media and 4IC cells cultured in lean adipose conditioned media. *p<0.05; error bars represent standard error of the mean*

Data were homoscedastic (Levene's p=0.55). The diffusivity of 231 cells, 231 cells cultured in obese adipose conditioned media, 231 cells cultured in lean

adipose conditioned media, 4IC cells, 4IC cells cultured in obese adipose conditioned media and 4IC cells cultured in lean adipose conditioned media were compared using one-way ANOVA followed by Tukey's test with Bonferroni correction. This is graphically represented in Figure 9-4.

Obese ASC CM did not significantly enhance diffusivity of either 231 or 4IC cells (p=1.0 & 0.981).

On the other hand, 231 cells displayed significantly increased diffusivity in lean ASC CM compared to obese ASC CM but not compared to control (1.74x p=0.0445 and p=0.0509). 4IC cells also displayed significantly increased diffusivity in lean ASC CM compared to both obese ASC CM and control (1.83x p=0.000849 and 1.67x p=0.00245).

Significantly enhanced cancer cell diffusivity in lean ASC CM was an unexpected finding in the context of the initial hypothesis but does reconcile with clinical observations [45] which indicate that while of obese people are more likely to develop breast cancer, lean patients having significantly worse outcomes in terms of systemic metastasis if they do develop the disease. While this is commonly attributed to the cancer cells having to navigate greater obstacles to metastasize as well as the immunomodulatory properties of adipose tissue, these data suggest that enhanced cancer cell motility due to signaling with adipose tissue may also play a role.

In addition, 4IC cells in lean ASC CM showed significantly higher diffusivity than 231s in lean ASC CM (1.59x p=0.00426), which was not observed in control media or obese ASC CM (p=0.0894 and 0.229), suggesting that lean adipose paracrine signaling appears to enhance metastatic characteristics of metaplastic TNBC when compared to non-metaplastic TNBC.

9.3.4 Comparison with conventional scratch test

As a pertinent example of the importance of accounting for cell proliferation in scratch assays, the 1mm wound closure rates were simply compared without calculating diffusivity. The data were homoscedastic (Levene's p=0.917). One-way ANOVA was performed followed by Tukey's test with Bonferroni correction. This is graphically represented in Figure 9-5.

231 cells closed wound significantly faster in both obese and lean adipose conditioned media (p=0.0077 and 0.0179 respectively). There was no significant difference in the wound closure rates between 231s subject to obese and lean adipose signaling (p=0.995). Similarly, 4IC cells closed wounds significantly faster in both obese and lean adipose conditioned media (p=0.0177 in both cases) and there was no significant difference in the wound closure rate between 4ICs subject to obese and lean adipose signaling

(p=0.147). Additionally, no significant differences were noted between the closure rates by 231s and 4ICs in lean adipose conditioned media (p=0.824).
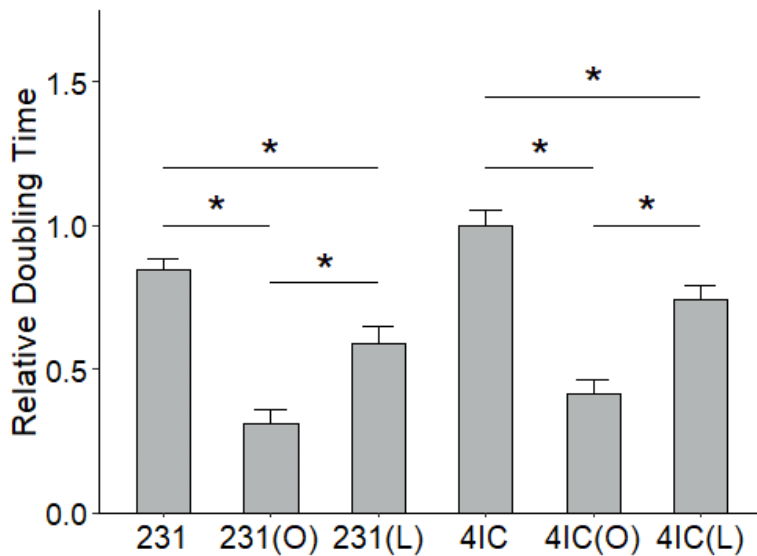

*Figure 9-5 Wound closure rates in 1mm laser photoablated scratches of 231 cells, 231 cells cultured in obese adipose conditioned media, 231 cells cultured in lean adipose conditioned media, 4IC cells, 4IC cells cultured in obese adipose conditioned media and 4IC cells cultured in lean adipose conditioned media. *p<0.05; error bars represent standard error of the mean*

A conventional scratch assay would have indicated that both obese and lean ASC CM enhance breast cancer cell migration simply based on the observation that the cells closed the gap faster. However, this would have been inaccurate, as by utilizing the mathematical model to account for proliferation revealed that the faster scratch closure in obese ASC CM is primarily due to increased cancer cell proliferation, and it is in fact the lean ASC CM that enhanced cancer cell

migration. Further, the finding indicating increased motility of metaplastic TNBC cells compared to non-metaplastic TNBC cells in lean ASC CM would have been missed.

9.3.5   Diffusivity in photoablated 2mm scratches

Diffusivity was calculated using the rate of closure of 2mm wide laser photoablated scratches and the respective breast cancer cell doubling times. It serves as a measure of cancer cell invasiveness and metastatic potential in the context of the mathematical model.

Data were homoscedastic (Levene's p=0.469). The diffusivity of 231 cells, 231 cells cultured in obese adipose conditioned media, 231 cells cultured in lean adipose conditioned media, 4IC cells, 4IC cells cultured in obese adipose conditioned media and 4IC cells cultured in lean adipose conditioned media were compared using one-way ANOVA followed by Tukey's test with Bonferroni correction. This is graphically represented in Figure 9-6.

Obese ASC CM did not significantly enhance diffusivity of either 231 or 4IC cells (p=0.833 & 0.966).
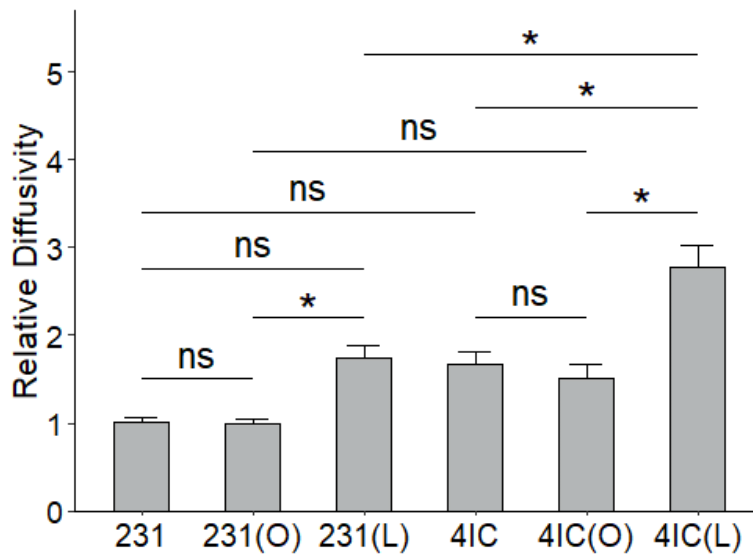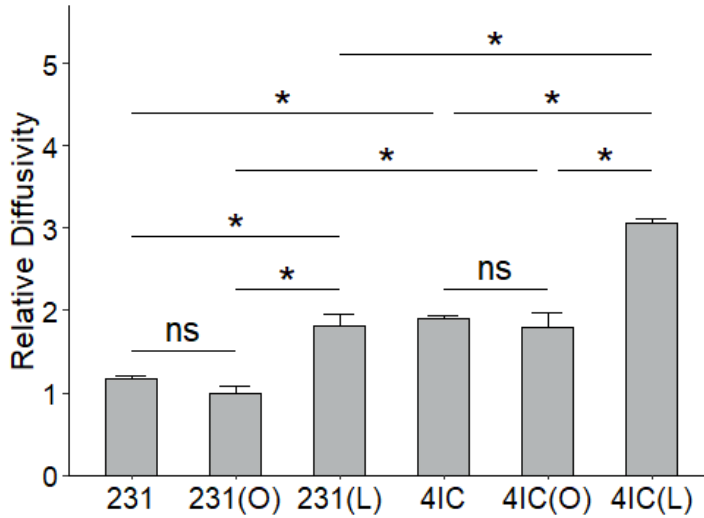
*Figure 9-6 Diffusivity in 2mm laser photoablated scratches of 231 cells, 231 cells cultured in obese adipose conditioned media, 231 cells cultured in lean adipose conditioned media, 4IC cells, 4IC cells cultured in obese adipose conditioned media and 4IC cells cultured in lean adipose conditioned media. *p<0.05; error bars represent standard error of the mean*

On the other hand, 231 cells displayed significantly increased diffusivity in lean ASC CM compared to both obese ASC CM and control (1.81x p=0.00135 and 1.54x p=0.0092). 4IC cells displayed significantly increased diffusivity in lean ASC CM compared to both obese ASC CM and control (1.71x p=0.0000175 and 1.61x p=0.000454). In 1mm scratches, 231s did not display significantly increased diffusivity in lean CM compared to control, suggesting that wider scratches may be necessary to uncover cellular behaviors that might be missed in narrower scratches.

Significantly enhanced cancer cell diffusivity in lean ASC CM was an unexpected finding in the context of the initial hypothesis but does reconcile with clinical observations [45] which indicate that while of obese people are more likely to develop breast cancer, lean patients having significantly worse outcomes in terms of systemic metastasis if they do develop the disease. While this is commonly attributed to the cancer cells having to navigate greater obstacles to metastasize as well as the immunomodulatory properties of adipose tissue, these data suggest that enhanced cancer cell motility due to signaling with adipose tissue may also play a role.

In addition, 4IC cells in lean ASC CM showed significantly higher diffusivity than 231s in lean ASC CM (1.69x p=0.0000201), which, unlike for 1mm scratches, was also observed in control media and obese ASC CM (1.79x p=0.00164 and 1.62x p=0.0031), suggesting that the observations relating to increased motility and metastatic characteristics of metaplastic TNBC cells may be missed in narrower scratches and only uncovered with wider scratches.

9.3.6   Comparison with conventional scratch test

As another pertinent example of the importance of accounting for cell proliferation in scratch assays, the 2mm wound closure rates were simply compared without calculating diffusivity. The data were homoscedastic

(Levene's p=0.878). One-way ANOVA was performed followed by Tukey's test with Bonferroni correction. This is graphically represented in Figure 9-7.

231 cells closed wound significantly faster in both obese and lean adipose conditioned media (p=0.0000577 and 0.000141 respectively). There was no significant difference in the wound closure rates between 231s subject to obese and lean adipose signaling (p=0.982). Similarly, 4IC cells closed wounds significantly faster in both obese and lean adipose conditioned media (p=0.0000158 and p=0.0000423 respectively) and there was no significant difference in the wound closure rate between 4ICs subject to obese and lean adipose signaling (p=0.96).

A conventional scratch assay would have indicated that both obese and lean ASC CM enhance breast cancer cell migration simply based on the observation that the cells closed the gap faster. However, this would have been inaccurate, as by utilizing the mathematical model to account for proliferation revealed that the faster scratch closure in obese ASC CM is primarily due to increased cancer cell proliferation, and it is in fact the lean ASC CM that enhanced cancer cell migration.
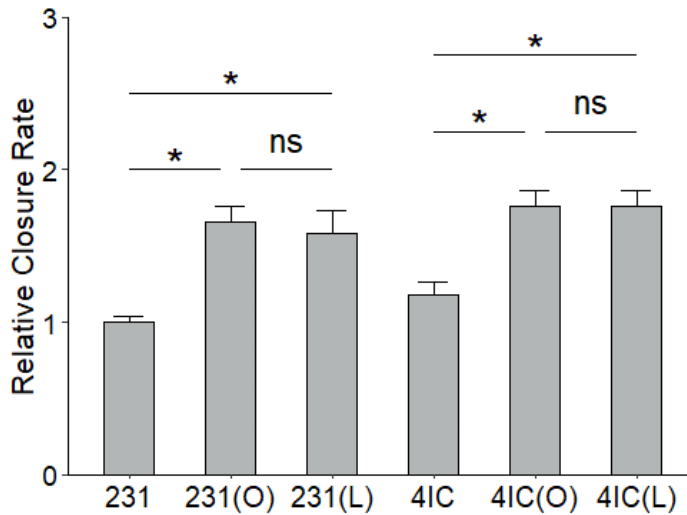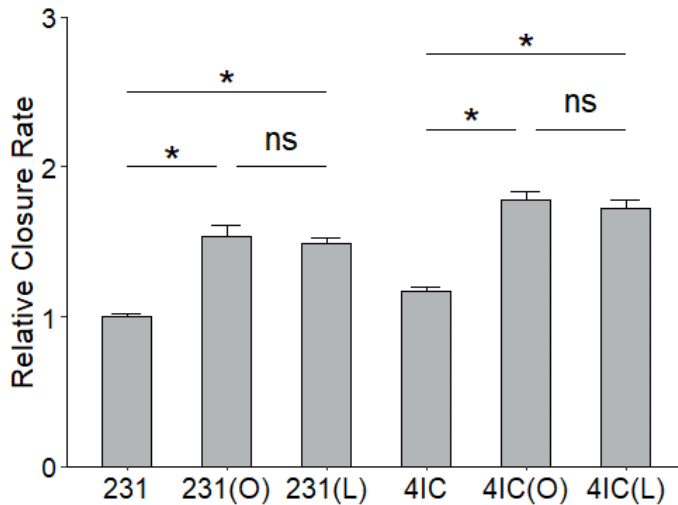
*Figure 9-7 Wound closure rates in 2mm laser photoablated scratches of 231 cells, 231 cells cultured in obese adipose conditioned media, 231 cells cultured in lean adipose conditioned media, 4IC cells, 4IC cells cultured in obese adipose conditioned media and 4IC cells cultured in lean adipose conditioned media. *p<0.05; error bars represent standard error of the mean*

9.4 Discussion

This study serves as another example of the utility and physiological relevance of the novel combination of a photoablated scratch assay and reaction-diffusion mathematical model. The initial hypothesis was confirmed and it was shown that paracrine signaling with obese adipose increases triple negative breast cancer cell proliferation, which aligns with clinical observations of higher risk of tumorigenesis and breast tumor growth in obese people. Additionally, an unexpected insight about triple negative breast cancer crosstalk with lean adipose was gained and the findings from this study demonstrate that paracrine

signaling with lean adipose significantly enhanced breast cancer cell motility, an effect that was not associated with obese adipose signaling. This was observed for both metaplastic and non-metaplastic triple negative breast cancer cells, as well as for both patient-derived cell line and a standard commercial cell line. It was also observed for both scratch widths, indicating that it wasn't an artifact of a specific wound width. While contrary to the initial hypothesis, it does recapitulate another significant clinical finding regarding obesity and breast cancer [45]. While obese patients are more likely to develop breast cancer, if lean do develop the disease, they tend to have worse outcomes particularly in terms of systemic metastasis. The general explanation has so far focused on there being fewer barriers for the cancer cells to navigate in order to intravasate into vasculature as well as the immunogenicity of adipose tissue. The findings from this study suggest that there may be another factor at play – the increased intrinsic motility of breast cancer cells due to crosstalk with lean adipose. It would be interesting to further examine why such crosstalk occurred with ASCs derived from lean patients but not obese patients, and if a therapeutic intervention could potentially exploit this interaction to inhibit metastasis.

Another noteworthy finding from this study was that the increased cancer cell motility due to signaling with lean ASCs and increased cancer cell proliferation due to signaling with obese ASCs would have appeared as identical effects if

a traditional scratch assay was performed, looking only at the wound closure rate and ignoring proliferation. A regular scratch assay would have concluded that both lean and obese adipose enhanced cancer cell migration. Using the novel assay, it was possible to decouple the contributions of proliferation and migration to scratch closure and subsequently delineate the inferences.

It would be interesting to translate this assay into a 3D breast tumor microenvironment model and consider the effect of biomechanical properties such as matrix stiffness. Incorporating vascular fluid in a microphysiological system would reveal further insights into the consequences of breast cancer-adipose signaling for cancer intravasation and metastasis. Further, patient specific models predicting tumor growth and metastasis could potentially be established going forward, by utilizing the patient's cancer cells and adipocytes, which could have interesting implications for personalized therapies.

9.5 Materials and Methods

Laser spot size characterization

A glass slide was coated with permanent marker ink and loaded on the substrate stage. The laser was focused on the slide and fired to ablate the ink. The slide was then imaged under a microscope and the spot size characterized.

Cell culture

MDA MB-231 human triple negative breast cancer cells were obtained from ATCC (Manassas, VA).

41C patient-derived metaplastic triple negative breast cancer cells derived from a patient specimen were obtained based on modified versions of previously published protocols by the Burow lab [40] [41]. Briefly, a mastectomy specimen from a 57 year old Caucasian female patient with metastatic breast cancer that was unresponsive to neoadjuvant chemotherapy with combination Adriamycin and cyclophosphamide therapy was procured. The TU-BcX-4IC tumor was dissected and a small tumor explant was plated in a 10 cm petri dish with DMEM supplemented with 10% FBS, 1% HEPES, 1% L-glutamine, 1% pyruvate, 1% essential amino acids, 1% nonessential amino acids, 1% antibiotic-antimycotic and 0.012% insulin (all reagents from Thermo Fisher Scientific, Waltham MA; FBS from Cytiva, Marlborough MA). Cells from the plated tumor were propagated until a finished monoculture of adherent cancer cells, lacking stromal cells, was attained and the TU-BCx-4IC cell line was hence established.

Patient adipose derived stem cells were obtained based on a previously published protocol [47]. Briefly, adipose tissue was collected by needle biopsy in lean patients and liposuction aspiration in obese patients (BMI < 25kg/m^2 and

BMI $\geq$ 25kg/m^2 respectively). ASCs were isolated from adipose tissue by first washing the tissue sample extensively with PBS containing 5% penicillin-streptomycin (Thermo Fisher Scientific, Waltham MA). Upon removal of debris, the sample was placed in a sterile tissue culture plate with 0.075% Collagenase Type I (Thermo Fisher Scientific, Waltham MA) prepared in PBS containing 2% pen-strep for tissue digestion. The adipose tissue sample was minced using scalpel and pipetted up and down with a 25-50 ml pipette several times to further facilitate the digestion. Next, the sample was incubated for 30 min and then the Collagenase Type I activity was neutralized by adding 5 ml of αMEM (Thermo Fisher Scientific, Waltham MA) containing 20% heat inactivated fetal bovine serum (Cytiva, Marlborough MA). The sample was again pipetted the sample up and down several times to further disintegrate aggregates of the adipose tissue. Upon disintegration, sample was strained into a 50 ml tube. The stromal vascular fraction, containing the ASCs, was obtained by centrifuging at 2000 rpm for 5 min. The pellet was resuspended to complete the separation of the stromal cells from the primary adipocytes. Centrifugation was repeated and all the collagenase solution above the pellet was aspirated without disturbing the cells. The pellet was then resuspended in 1 ml lysis buffer (Qiagen, Germantown MD), incubated for 10 min on ice, washed with 20 ml of PBS with 2% pen-strep and centrifuged at 2000 rpm for 5 min. The supernatant was aspirated, the cell pellet is resuspended in a maximum of 3 ml of stromal medium (alpha-MEM) supplemented with 20% FBS, 1% L-glutamine, and 1%

penicillin/streptomycin (Thermo Fisher Scientific, Waltham MA) and the cell suspension is filtered through 70 μm cell strainer. The cell strainer was washed with an additional 2 ml of stromal medium to obtain any additional cells. The sample containing the cells was plated in a PLL coated culture plate and incubated at 37 °C, 5% CO2. The cells in a single well of a 12 well plate were inoculated for an amount of about 500 mg of adipose tissue.

After 72 hours, entire medium was aspirated from the wells. If the SVF did not expand well, the FBS concentrated was increased to 25% as long as it did not promote premature adipogenesis. The cells were washed with prewarmed PBS with 1% antibiotic-antimycotic to clean the cells thoroughly from any tissue fragments and/or blood cells. Then, fresh stromal medium was added according to the well capacity of the culture plate. The cells were maintained in a humidified tissue culture incubator at 37 °C with 5% CO2. Medium was changed every second day until the cells reach 80–90% confluence, and then ASCs were harvested. For harvesting viable ASCs, 250-500 μl of sterile warm PBS was added to the wells and incubated for 2 min. The PBS was then replaced with 2.9mM EDTA solution in PBS and the cells were incubated for detachment. The ASCs were then resuspended and plated in desired concentrations, verifying their viability with Trypan blue exclusion and cell counting. Once harvested, ASCs were cultured in the same medium formulation as cancer cells as detailed in the following paragraph.

All cells were cultured in DMEM supplemented with 10% FBS, 1% HEPES, 1% L-glutamine, 1% pyruvate, 1% antibiotic-antimycotic and 0.012% insulin. (All reagents from Thermo Fisher Scientific, Waltham MA).

Cells were serum-starved 48 hours prior to commencing the scratch assays in Opti-MEM supplemented with 0.5% FBS, 1% HEPES, 1% L-glutamine, 1% pyruvate, 1% essential amino acids, 1% nonessential amino acids, 1% antibiotic-antimycotic and 0.012% insulin.

Two-way crosstalk conditioned media

Cancer cells and ASCs were simultaneously cultured in Opti-MEM – cancer cells in 0.5% FBS and ASCs in 1.5% FBS (with all other supplement concentrations as mentioned above) for 12 hours. Then, half of the ASC media was replaced with cancer conditioned media and the ASCs cultured for 72 hours. Next, half of the ASC crosstalk conditioned media was added back into the cancer cells, diluted 1:1 with fresh serum-free media (i.e. Opti-MEM with all supplements as above but 0% FBS). This protocol recapitulates two-way cancer-adipose crosstalk and results in a 0.5% FBS concentration for the assay, which – according to preliminary testing – is the minimum serum concentration required to keep the cancer cells viable for at least 14 days

(assay duration was less than 5 days). Moreover, 1% FBS keeps the ASCs alive for at least a week and thus ASC viability was not affected in this protocol. Conditioned media was filtered via a 0.2um filter at each step to remove debris.

Motion control codes for laser ablation paths

Scratches with widths of 1mm and 2mm and a length of 6mm were sketched out and the sketches were overlaid with a grid with unit cell of the characterized laser spot size, 300um. Laser spot paths were created in a meandering pattern with 50% overlap between adjacent paths. The motion control codes for these paths were compiled into G-code and programmed into the laser direct write CAD/CAM controller.

Laser photoablation of scratches

The laser was warmed up by firing 2000 pulses at 20Hz and then 5000 pulses at 100Hz with maximum voltage applied to the electrodes (15kV). The discharge voltage was adjusted to attain a fluence of 0.31J/cm^2 for a spot size of 300um.

Media was aspirated from the test dish and the dish was placed on the substrate stage. The substrate stage was raised to focus the laser beam on the interface of the thin film of media. The motion control code was executed

synchronized with the laser pulsing. If photoablation did not start occurring, the laser discharge voltage was increased in small increments until it did, the threshold ablation fluence was noted. The substrate stage was lowered and the test dish removed. Next, the above procedure was repeated for the assay dish, with the laser fluence set slightly above the ablation threshold for the respective cell layers.

1mm and 2mm scratches were photoablated for 231 and 4IC cell layers cultured in control, obese adipose conditioned media and lean adipose conditioned media, with one scratch per dish.

Cell proliferation assays

Approximately 5000-8000 cells were seeded per well in 96 well plates, grown until confluence while being imaged every 12 hours, detached and counted. The time taken to achieve confluence was recorded. Cell counting was done using an automated cell counter to reduce human error, with trypan blue exclusion of nonviable cells. At least 12 wells per experimental group were seeded to minimize sampling and counting errors. The doubling time was calculated using the standard cell growth equation. Two-way crosstalk conditioned media was used in the respective obese and lean adipose treatment groups.

Imaging and characterization

Photoablated scratches were imaged every 12 hours to begin with and then every 6 hours as they approached closure. At the first timepoint, the scratch width was measured and recorded. Scratches were considered fully closed when confluence was attained in the wound area and there was no change in the morphology of the cell layer on two consecutive readings, and then the first of those two readings was considered as the healed timepoint. The scratch closure rate was determined based on closure time and initial width, and was subsequently used to calculate the cellular diffusivity using on the traveling wave solution of the Fisher-KPP equation.

Statistical analysis

Each scratch was independent i.e., one scratch per dish. All experiments were performed in triplicate (n = 3). Statistical analyses were performed using one-way ANOVA and Tukey's test with Bonferroni corrected $p < 0.05$ was considered significant (i.e. significance level $\alpha = 95\%$). Effect sizes were expressed as generalized eta squared (GES) values with 95% confidence intervals. All analyses were performed in R.

Illustrations

Illustrations were created using BioRender.

10 Effect of EGF & TNF-α On Dermal Wound Healing

10.1 Introduction

Considering that the previous studies utilizing the novel photoablated wound healing assay focused on cancer cells, it was interesting to explore how the assay would fare in noncancerous cells, especially given that cancer cells generally have higher proliferative rates and accounting for proliferation is a key attribute of the assay. Herein, human dermal fibroblast migration and proliferation was assessed in response to a growth factor and cytokine treatment. The chosen growth factor (EGF) and cytokine (TNF-α) are known to play key roles in enhancing cutaneous wound healing [48] [49]. Unlike the tumor microenvironment, soluble factors in the cutaneous wound microenvironment are better characterized and have less redundancy and hence, it was reasonable to pick individual factors to test.

10.2 Hypotheses

Based on prior literature [50] [51] [52] [53] and using the previously developed novel photoablated scratch assay, the following hypotheses were tested:

- Epidermal growth factor (EGF) enhances fibroblast proliferation and migration in dermal wounds.

- Intermittently increased concentration of tumor necrosis factor alpha (TNF-α) enhances fibroblast proliferation and migration dermal wounds.

10.3 Results

The combination of a novel laser direct write photoablated scratch assay with a reaction-diffusion based mathematical model – that was developed and validated in the previous study – was herein used to analyze the influence of growth factor and cytokine treatment on cutaneous wound healing.

10.3.1 Study design

Migratory and proliferative characteristics of human dermal fibroblasts with a continuous EGF treatment and an intermittent TNF-α treatment were analyzed using the novel laser photoablated scratch assay described previously.

Since deeper cutaneous wounds are clinically significant, BJ CRL-2522 human dermal fibroblasts were the focus of this wound healing assay. Fibroblasts were normally cultured in DMEM supplemented with 10% FBS, 1% HEPES, 1% L-glutamine, 1% sodium pyruvate and 1% antibiotic-antimycotic and serum-

starved for the scratch assay in Opti-MEM supplemented with 2% FBS, 1% HEPES, 1% L-glutamine, 1% sodium pyruvate and 1% antibiotic-antimycotic. Preliminary testing showed that 2% FBS was the minimum concentration required to maintain fibroblast viability for at least 14 days (assay duration was less than 5 days). The cells were serum-starved for 48 hours prior to photoablative wounding to eliminate any persisting effects of the serum factors. Although the mathematical model takes cell proliferation into account, low serum media was used for the scratch assay because factors in the serum can mask the effects of the growth factor and cytokine treatments.

The influence of a key growth factor on dermal wound healing was studied by treating the human fibroblasts with 20ng/mL of recombinant human EGF. Previous studies have suggested that similar concentrations of EGF led to improved dermal wound healing [54] [55] [48] [56].

The influence of a key cytokine on dermal wound healing was studied by intermittently treating the human fibroblasts with 20ng/mL of recombinant human TNF-α from hour 48-72 after wounding. The reasons for using an intermittent treatment instead of a continuous treatment were twofold. First, preliminary testing showed that continuous TNF-α treatment led to fibroblast apoptosis – a finding that is also replicated in literature [49]. Second, *in vivo* studies have shown that administering TNF-α early in the wound healing process (but not immediately upon wounding) leads to faster wound healing

[53]. The experimental groups are summarized in Table 10-1 and the laser direct write photoablation setup is depicted in Figure 10-1.

Laser photoablated scratch assays and proliferation assays were performed as previously described.

Experiments were conducted in triplicate (n=3). Statistical analyses were performed using one-way ANOVA and Tukey's test with Bonferroni corrected $p < 0.05$ considered significant (i.e. significance level $\alpha = 95\%$). Effect sizes were expressed as generalized eta squared (GES) values with 95% confidence intervals.

Table 10-1 Experimental groups for laser photoablated scratch assay to study the influence of EGF and TNF-α on dermal wound healing

Treatment	Type
Control	-
20ng/mL EGF	Continuous
20ng/mL TNF-α	Intermittent, from hour 48-72
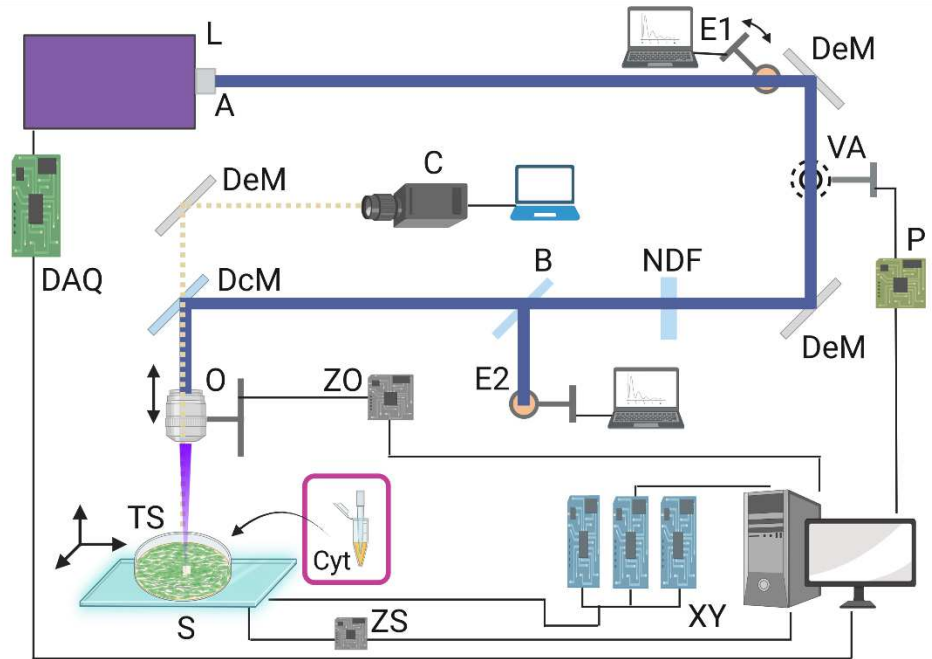
Figure 10-1 Laser direct write photoablation setup for elucidating the effect of cytokines and growth factors on dermal wound healing (Cyt = cytokine treatment)

10.3.2 Proliferation assays

Proliferation assays were performed and the doubling time was calculated using the methods described previously – with the growth factor and cytokine treatment administered identically to the photoablated scratches i.e. continuous EGF treatment but intermittent TNF-α treatment.

Data were homoscedastic (Levene's p=0.989). The doubling times of human dermal fibroblasts with EGF and TNF-α treatment were compared using one-

way ANOVA followed by Tukey's test with Bonferroni correction. This is graphically represented in Figure 10-2.
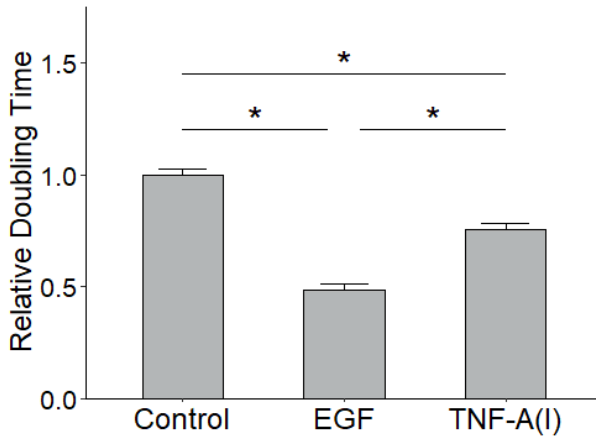
*Figure 10-2 Doubling times of human dermal fibroblasts with epidermal growth factor and tumor necrosis factor alpha treatment. *p<0.05; error bars represent standard error of the mean*

Both EGF and intermittent TNF- α (TNF-A(I)) treatments significantly enhanced human dermal fibroblast proliferation compared to control (2.06x and 1.32x respectively; p=0.0000139 and 0.00096). Further, EGF significantly increased fibroblast proliferation compared to TNF- α (1.55x p=0.000576).

10.3.3 Diffusivity in photoablated 1mm scratches

Figure 10-3 Diffusivity of human dermal fibroblasts with epidermal growth factor and tumor necrosis factor alpha treatment in laser photoablated 1mm wounds. *p<0.05; error bars represent standard error of the mean

Diffusivity of human fibroblasts was calculated using the rate of closure of 1mm wide laser photoablated scratches and the respective. It serves as a measure of fibroblast infiltration into the wound in the context of the mathematical model.

Data were homoscedastic (Levene's p=0.268). The diffusivity of fibroblasts treated with EGF and TNF-α were compared with one-way ANOVA followed by Tukey's test with Bonferroni correction. This is graphically represented in Figure 10-3.

EGF treatment significantly enhanced fibroblast infiltration into wounds compared to control (2.59x p=0.000043). Intermittent TNF-α, on the other hand, significantly reduced fibroblast motility (0.53x p=0.0234).

10.3.4 Comparison with conventional scratch test

As an example of the importance of accounting for cell proliferation in scratch assays, the 1mm wound closure rates were simply compared without calculating diffusivity. The data were homoscedastic (Levene's p=0.8535). One-way ANOVA was performed followed by Tukey's test with Bonferroni correction. This is graphically represented in Figure 10-4.

EGF treated fibroblasts closed wounds significantly faster compared to control and intermittent TNF-α treated fibroblasts (p=0.0000328 and 0.0000162 respectively). Also, there was no significant difference between the closure rates of control and TNF-α treated fibroblasts (p=0.311).

If a conventional scratch test was performed, simply looking at the gap closure rate, then it would appear as if TNF-α has no significant effect on fibroblast migration – whereas in reality, as demonstrated by above, the significantly increased proliferation makes up for significantly decreased motility, resulting in a closure rate similar to control. A traditional scratch assay would also overestimate the effect of EGF on migration.
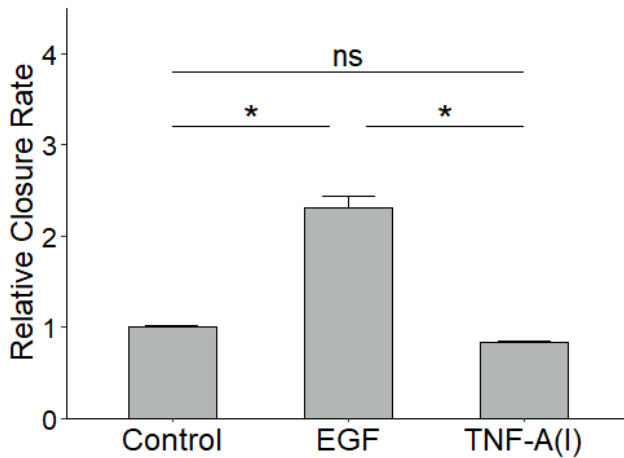
Figure 10-4 1mm wound closure rates of human dermal fibroblasts with epidermal growth factor and tumor necrosis factor alpha treatment. *p<0.05; error bars represent standard error of the mean

10.3.5 Diffusivity in photoablated 2mm scratches

Diffusivity of human fibroblasts was calculated using the rate of closure of 2mm wide laser photoablated scratches and the respective. It serves as a measure of fibroblast infiltration into the wound in the context of the mathematical model.

Data were homoscedastic (Levene's p=0.536). The diffusivity of fibroblasts treated with EGF and TNF-α were compared with one-way ANOVA followed by Tukey's test with Bonferroni correction. This is graphically represented in Figure 10-5.

EGF treatment significantly enhanced dermal fibroblast infiltration into wounds compared to control (2.72x p=0.0000000828). Intermittent TNF-α treatment, on the other hand, significantly reduced dermal fibroblast diffusivity (0.55x p=0.000161).

These findings were replicated in both 1mm and 2mm wounds, indicating that they were not an artifact of a specific scratch width.
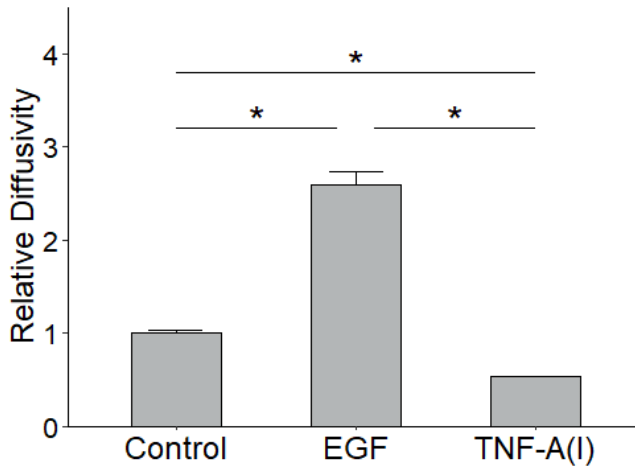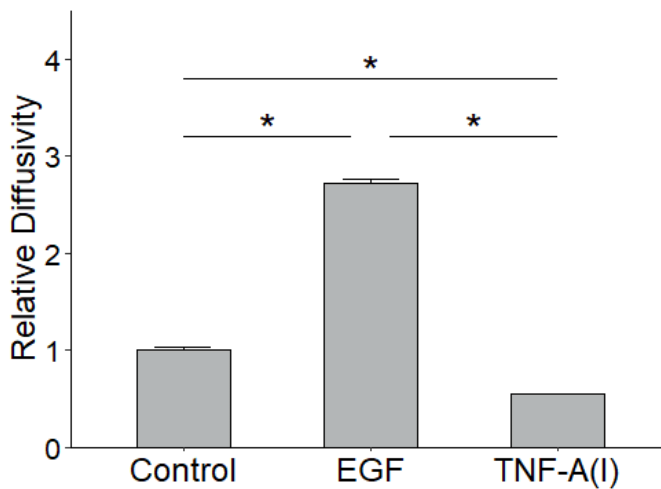

*Figure 10-5 Diffusivity of human dermal fibroblasts with epidermal growth factor and tumor necrosis factor alpha treatment in laser photoablated 2mm wounds. *p<0.05; error bars represent standard error of the mean*

10.3.6 Comparison with conventional scratch test

As an example of the importance of accounting for cell proliferation in scratch assays, the 2mm wound closure rates were simply compared without calculating diffusivity. The data were homoscedastic (Levene's p=0.645). One-way ANOVA was performed followed by Tukey's test with Bonferroni correction. This is graphically represented in Figure 10-6.
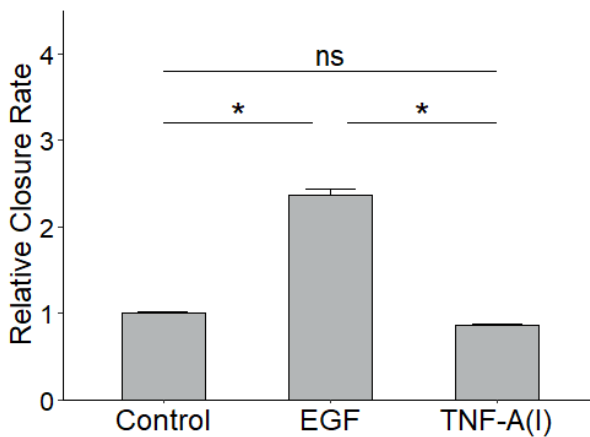
*Figure 10-6 2mm wound closure rates of human dermal fibroblasts with epidermal growth factor and tumor necrosis factor alpha treatment. *p<0.05; error bars represent standard error of the mean; error bars represent standard error of the mean*

EGF treated fibroblasts closed wounds significantly faster compared to control and intermittent TNF-α treated fibroblasts (p=0.00000092 and 0.000000608

respectively). Also, there was no significant difference between the closure rates of control and TNF-α treated fibroblasts (p=0.0943).

If a conventional scratch test was performed, simply looking at the gap closure rate, then it would appear as if TNF-α has no significant effect on fibroblast migration – whereas in reality, as demonstrated by above, the significantly increased proliferation makes up for significantly decreased motility, resulting in a closure rate similar to control. A traditional scratch assay would also overestimate the effect of EGF on migration.

10.4 Discussion

This study served as a useful example of the application of the laser photoablation based assay in combination with the mathematical model for noncancerous cells. Continuous presence of EGF was demonstrated to enhance dermal fibroblast proliferation and migration during wound healing. Intermittent presence of TNF-α, on the other hand, was shown to enhance proliferation but inhibit migration. EGF also led to a significantly greater increase in fibroblast proliferation compared to TNF-α. The effect of TNF-α differed from the initial hypothesis, indicating the utility of this assay to obtain biological insights in noncancerous cells as well. Again, findings held true for

two scratch widths, indicating that they were not artifacts of a particular scratch width.

Upon comparing the conclusions from this assay to a conventional scratch assay, important differences were observed – highlighting its advantage for studies involving noncancerous cells as well. A regular scratch assay solely looking at scratch closure rate and ignoring proliferation would conclude the TNF-α had no effect on fibroblast migration. The novel assays reveals that the reduced migration negates the effect of increased proliferation with intermittent TNF-α treatment, making the scratch closure times not significantly different compared to the control group.

Future work could include translating this assay into a 3D multilayered skin model and/or a microphysiological system incorporating vascular fluid flow to add further physiological relevance. Examining the effects of other characteristics such as matrix stiffness would lead to further insights into the wound healing process. Moreover, the simultaneous influence of glycemic conditions and wound symmetry, as well as their interactions, could be examined by combining this assay with the previously developed technique for photoablating wounds of any given geometry.

10.5 Materials and Methods

Laser spot size characterization

A glass slide was coated with permanent marker ink and loaded on the substrate stage. The laser was focused on the slide and fired to ablate the ink. The slide was then imaged under a microscope and the spot size characterized.

Cell culture

BJ CRL-2522 human dermal fibrobasts (ATCC, Manassas VA) were cultured in DMEM supplemented with 10% FBS, 1% HEPES, 1% L-glutamine, 1% pyruvate, 1% antibiotic-antimycotic. (All reagents from Thermo Fisher Scientific, Waltham MA; FBS from Cytiva, Marlborough MA).

Cells were serum-starved 48 hours prior to commencing the scratch assays in Opti-MEM supplemented with 2% FBS, 1% HEPES, 1% L-glutamine, 1% pyruvate, 1% antibiotic-antimycotic.

The effects of EGF on wound healing were studied by supplementing the low serum media continuously with 20ng/mL of human recombinant EGF (Lonza, Walkersville MD). The effects of TNF-α on wound healing were studied by supplementing the low serum media intermittently – from hour 48-72 after wounding – with 20ng/mL human recombinant TNF-α (Bio-Techne, Minneapolis MN).

Motion control codes for laser ablation paths

Scratches with widths of 1mm and 2mm and a length of 6mm were sketched out and the sketches were overlaid with a grid with unit cell of the characterized laser spot size, 300um. Laser spot paths were created in a meandering pattern with 50% overlap between adjacent paths. The motion control codes for these paths were compiled into G-code and programmed into the laser direct write CAD/CAM controller.

Laser photoablation of scratches

The laser was warmed up by firing 2000 pulses at 20Hz and then 5000 pulses at 100Hz with maximum voltage applied to the electrodes (15kV). The discharge voltage was adjusted to attain a fluence of $0.31J/cm^2$ for a spot size of 300um.

Media was aspirated from the test dish and the dish was placed on the substrate stage. The substrate stage was raised to focus the laser beam on the interface of the thin film of media. The motion control code was executed synchronized with the laser pulsing. If photoablation did not start occurring, the laser discharge voltage was increased in small increments until it did, the threshold ablation fluence was noted. The substrate stage was lowered and the

test dish removed. Next, the above procedure was repeated for the assay dish, with the laser fluence set slightly above the ablation threshold for the respective cell layers.

1mm and 2mm scratches were photoablated in dermal fibroblast cell layers, with one scratch per dish.

Cell proliferation assays

Approximately 5000-8000 cells were seeded per well in 96 well plates, grown until confluence while being imaged every 12 hours, detached and counted. The time taken to achieve confluence was recorded. Cell counting was done using an automated cell counter to reduce human error, with trypan blue exclusion of nonviable cells. At least 12 wells per experimental group were seeded to minimize sampling and counting errors. The doubling time was calculated using the standard cell growth equation. Growth factor and cytokine supplemented media was used in the respective treatment groups.

Imaging and characterization

Photoablated scratches were imaged every 12 hours to begin with and then every 6 hours as they approached closure. At the first timepoint, the scratch width was measured and recorded. Scratches were considered fully closed

when confluence was attained in the wound area and there was no change in the morphology of the cell layer on two consecutive readings, and then the first of those two readings was considered as the healed timepoint. The scratch closure rate was determined based on closure time and initial width, and was subsequently used to calculate the cellular diffusivity using on the traveling wave solution of the Fisher-KPP equation.

Statistical analysis

Each scratch was independent i.e., one scratch per dish. All experiments were performed in triplicate (n = 3). Statistical analyses were performed using one-way ANOVA and Tukey's test with Bonferroni corrected $p < 0.05$ was considered significant (i.e. significance level α = 95%). Effect sizes were expressed as generalized eta squared (GES) values with 95% confidence intervals. All analyses were performed in R.

Illustrations

Illustrations were created using BioRender.

11 Summary and Future Directions

The laser direct write system was successfully re-engineered. The issues with excimer laser were diagnosed, repaired and its functionality restored by repairing the power supply DC converter and reconfiguring the electronic control board. Further, its output energy was enhanced to be conducive for processing of biological materials by replacing the thyratron and out coupler, removing the internal aperture and installing an external gas valve. Next, the laser control system was configured, which involved building an external 3D printed air-cooled assembly for the DAQ card. In addition, the control systems for all components of the laser direct write system were re-engineered – the XY CAD/CAM motion control stages, the Z-stages, the energy meters, the variable aperture and the telescopic as well as side-view cameras. Driver conflicts were avoided by spreading control across multiple computers. All parameter files were backed up to allow future users to restore functionality with a single click. The next-generation laser direct write system was stress tested by simulating scenarios which caused serious issues with the previous generation system, and robust and reliable functionality of the current system was confirmed.

The laser direct write system was successfully utilized for additive processing. Heterocellular arrays of cancer and stromal cells, with homotypic and

heterotypic spots were bioprinted in defined geometries to allow for study of cell-cell interactions in the breast tumor microenvironment. Human macrophages were viably printed with high fidelity to address the lack of immune component in most *in vitro* engineered tissues, paving the way for bioprinting immunocompetent constructs.

The laser direct write system was also successfully utilized for subtractive processing. A novel laser photoablation assay was developed to generate wounds of any given geometry and used to elucidate the influence of wound symmetry and how it interacts with glycemic conditions. Symmetric wounds were found to heal at higher rates even after controlling for glycemic conditions, and vice versa. The influence of symmetry dominated in smaller wounds whereas the influence of glycemic condition dominated in larger wounds. Further, a novel photoablated scratch assay was developed and combined with a reaction-diffusion based mathematical model to decouple the influence of cell migration and proliferation on wound closure. This assay was performed to elucidate the influence of juxtacrine stromal signaling on breast cancer using patient derived cells and patient derived xenografts. Stromal signaling enhanced breast cancer migration and proliferation, and the influence of stromal cells in the patient-derived xenografts could be recapitulated *in vitro* by co-culturing patient cells with human fibroblasts. The assay was also performed to elucidate the influence of paracrine adipose signaling on breast cancer using

patient derived cancer and adipose stem cells from obese and lean patients. Obese adipose signaling led to increase in breast cancer cell proliferation but lean adipose signaling led to increase breast cancer cell motility, which reconciles with clinical findings of obese people more likely to develop breast cancer but lean patients faring worse if they do develop the disease largely due to systemic metastasis. Finally, this assay was utilized with noncancerous cells – dermal fibroblasts to elucidate the influence of epidermal growth factor and tumor necrosis factor alpha on fibroblast migration and proliferation during wound healing. Continuous treatment with epidermal growth factor enhanced fibroblast migration and proliferation while intermittent tumor necrosis alpha treatment enhanced proliferation but suppressed fibroblast migration. All of the laser photoablated assays led to physiologically relevant insights that would not have been revealed in conventional assays.

Now, the natural question is: What is the next phase of development for the laser direct write system? Since more than 90% drugs that show positive results in standard cell culture and animal models fail in clinical trials [57], there exists a massive need for tissue engineered humanized models for disparate organs and tissues in healthy and diseased states, which comprise physiologic cues to elicit physiologically relevant cell behavior and interactions and are also conducive to high throughput screening of candidate drug compounds.

Such platforms are termed microphysiologcal or "organ-on-chip" systems [58]. Being an emergent technology, these systems tend to be non-standardized and as a result, it is difficult to achieve experimental validity. To increase their physiological relevance and reproducibility, they require human cells arranged in heterocellular biomimetic patterns subject to physiological cues. The cells should either be derived from patients or differentiated from patient-derived induced pluripotent stem cells. Microfluidic vascular flow is essential, along with organ or tissue-specific biomechanical and biochemical cues, which would dictate the chip design. Incorporating such features would represent a significant step towards standardization and greater experimental validity. Laser direct write technology is capable of incorporating all of the above into a single uniquely integrated platform to fabricate standardized organ chips with highly customizable designs and configurations for high throughput, reproducible drug efficacy and toxicity assays. This suggests strong commercialization potential.

A successful commercialization strategy is predicated on two important pillars: Technological validation and market validation.

The body of work summarized above highlights the capabilities of the laser direct write system as a platform technology. Precise laser direct write bioprinting (additive processing) and photoablation (subtractive processing) were demonstrated to have led to clinically relevant findings. Moreover, the

next-generation instrument is robust, reliable and has a highly automated workflow, which are essential qualities for successful commercialization. By combining the precise subtractive and additive processing dual functionality of this system, customized organ chips can be fabricated. CAD/CAM photoablation can generate precisely etched microfluidic channels and wells in elastomers, and multiple cell types can then be patterned in desired geometries with high resolution. In addition to printing cells, laser direct write is also capable of printing 3D organoids and cell-laden encapsulated constructs on a wide variety of substrates. The full range of capabilities of this system that make it highly conducive for fabrication of standardized, customizable organ-on-chip systems are summarized in Figure 11-1.

One such example is the patent-pending competitive differentiation/migration assay that was developed using the laser direct write platform. A spoke-channel pattern ("sunburst") surrounding a central well was photoablated on a hydrogel substrate to provide simultaneous cues with customizable gradients to the entity (cells, 3D multicellular organoid, spheroid, embryoid body etc.) that is printed precisely into the central well. A single channel configuration allows for elucidating the effect of a factor individually ("horserace"). The combination of single and multiple highly customizable cues within the same assay leads to unique insights. Here, this assay was utilized to investigate differentiation of embryonic stem cells in response to simultaneous cues from extracellular

matrix proteins in the channels. 3D embryoid bodies were printed in the wells

(Figure 11-2) and displayed direction-specific differentiation.

Figure 11-1 The attributes of laser direct write make it highly conducive for customized organ-on-chip fabrication
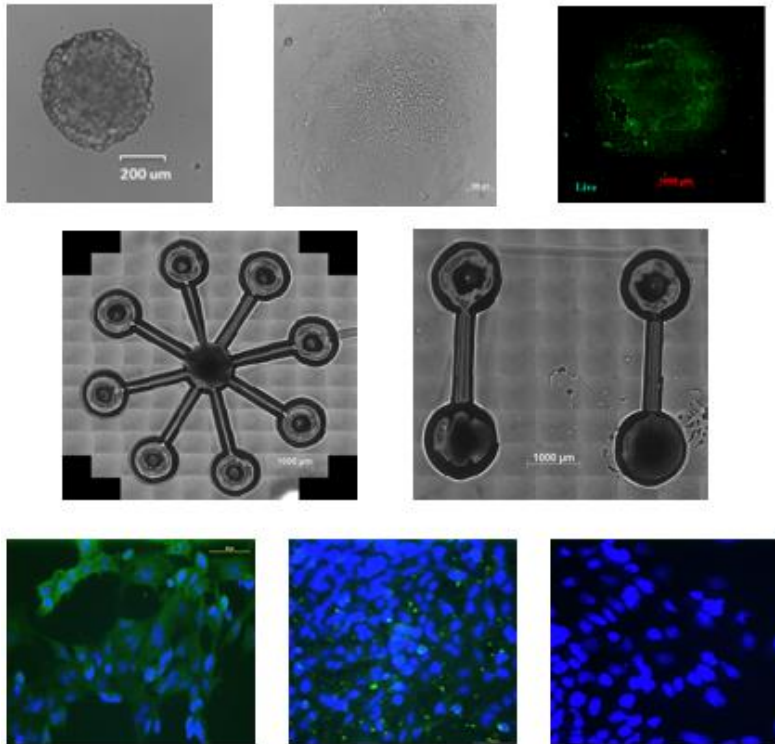
Figure 11-2 Patent-pending "sunburst" and "horserace" assays fabricated using laser direct write. Printed embryoid body displays direction-specific differentiation

The other pillar for a successful commercial strategy is market validation. The

Chrisey Lab engaged in the NSF I-Corps program to elicit feedback from

potential biotech and pharmaceutical clients focused on drug discovery.

Pharmaceutical companies were interested in specific organ-on-chip assays

depending upon the application (tissue/organ, disease, endpoints, readout etc.)

Understandably, they sought standardization and experimental validity. Some

pharmaceutical companies preferred to outsource the entire process including

the fabrication of organ chips as well as the drug efficacy and toxicity assays

and receive the data. Other pharmaceutical companies preferred to purchase

organ chips tailored to their applications and do the assays in-house.

Biotechnology companies that specialized in organ chips, on the other hand,

were interested in advanced systems such as the laser direct write platform to

address manufacturing bottlenecks. However, biotech organ chip companies

generally lacked the requisite capital to be able to purchase the entire laser

direct write instrument as one integrated system. Since the true strength of this

platform is as a single, uniquely integrated system, it seemed logical to target

the pharmaceutical clients as a contract research organization – as opposed to

attempting to sell different modules of the laser direct write system separately.

Hence, CytoFocale LLC was co-founded by Prof. Chrisey and me as a contract

research organization that would offer both services and products to

pharmaceutical clients focused on drug discovery. The services side of the

business would target the pharmaceutical companies that choose to outsource

their assays, and CytoFocale would offer microphysiological or organ-on-chip

based assays that are highly tailored to the specific application such as a disease, tissue/organ, therapy, endpoint etc. On the other hand, the products side of the business would target the pharmaceutical companies that choose to purchase their organ chips and perform assays in-house, and CytoFocale would offer on-demand organ chip fabrication customized to a specific application. Our dual-focus would ensure continual improvement and increased efficiency in both fabricating organ chips and conducting biological assays, and the company would hence be well-positioned to capitalize as we approach an era of personalized medicine and patient-specific therapies, which are critically needed to improve patient responses to multifaceted diseases such as cancer and autoimmune conditions [58]. Additionally, we also plan on having a special commitment to focus on understudied diseases and disorders that are prevalent among underserved populations. The next step would be to apply for a Phase 1 SBIR/STTR small business grant to focus our initial offerings and commence R&D as well as client engagement, that would enable progression onto Phase 2 and hopefully attract venture capital investment.

References

[1] S. V. Murphy and A. Atala, "3D bioprinting of tissues and organs," *Nat. Biotechnol.*, vol. 32, no. 8, pp. 773–785, Aug. 2014, doi: 10.1038/nbt.2958.

[2] C. Mandrycky, Z. Wang, K. Kim, and D.-H. Kim, "3D bioprinting for engineering complex tissues," *Biotechnol. Adv.*, vol. 34, no. 4, pp. 422–434, Jul. 2016, doi: 10.1016/j.biotechadv.2015.12.011.

[3] J. Saksena, S. C. Sklare, T. B. Phamduy, Y. Huang, and D. B. Chrisey, "The Power of CAD/CAM Laser Bioprinting at the Single-Cell Level: Evolution of Printing," in *3D Bioprinting and Nanotechnology in Tissue Engineering and Regenerative Medicine*, Elsevier, 2022, pp. 93–121. doi: 10.1016/B978-0-12-824552-1.00004-9.

[4] T. Baldacchini *et al.*, "Translation of laser-based three-dimensional printing technologies," *MRS Bull.*, vol. 46, no. 2, pp. 174–185, Feb. 2021, doi: 10.1557/s43577-021-00042-2.

[5] N. R. Schiele, D. B. Chrisey, and D. T. Corr, "Gelatin-Based Laser Direct-Write Technique for the Precise Spatial Patterning of Cells," *Tissue Eng. Part C Methods*, vol. 17, no. 3, pp. 289–298, Mar. 2011, doi: 10.1089/ten.tec.2010.0442.

[6] J. L. Curley, S. C. Sklare, D. A. Bowser, J. Saksena, M. J. Moore, and D. B. Chrisey, "Isolated node engineering of neuronal systems using laser direct write," *Biofabrication*, vol. 8, no. 1, p. 015013, Feb. 2016, doi: 10.1088/1758-5090/8/1/015013.

[7] H. E. Burks *et al.*, "Laser Direct-Write Onto Live Tissues: A Novel Model for Studying Cancer Cell Migration," *J. Cell. Physiol.*, vol. 231, no. 11, pp. 2333–2338, Nov. 2016, doi: 10.1002/jcp.25363.

[8] M. H. Niemz, *Laser-tissue interactions: fundamentals and applications*, 3rd, enlarged ed ed. Berlin ; New York: Springer, 2004.

[9] D. Young, R. C. Y. Auyeung, A. Piqué, D. B. Chrisey, and D. D. Dlott, "Time-resolved optical microscopy of a laser-based forward transfer process," *Appl. Phys. Lett.*, vol. 78, no. 21, pp. 3169–3171, May 2001, doi: 10.1063/1.1372200.

[10] K. F. Renk, *Basics of Laser Physics*. Berlin, Heidelberg: Springer Berlin Heidelberg, 2012. doi: 10.1007/978-3-642-23565-8.

[11] C. Roma-Rodrigues, R. Mendes, P. Baptista, and A. Fernandes, "Targeting Tumor Microenvironment for Cancer Therapy," *Int. J. Mol. Sci.*, vol. 20, no. 4, p. 840, Feb. 2019, doi: 10.3390/ijms20040840.

[12] N. Ibata and E. M. Terentjev, "Development of Nascent Focal Adhesions in Spreading Cells," *Biophys. J.*, vol. 119, no. 10, pp. 2063–2073, Nov. 2020, doi: 10.1016/j.bpj.2020.09.037.

[13] B. Gok Yavuz *et al.*, "Cancer associated fibroblasts sculpt tumour microenvironment by recruiting monocytes and inducing immunosuppressive PD-1+ TAMs," *Sci. Rep.*, vol. 9, no. 1, p. 3172, Dec. 2019, doi: 10.1038/s41598-019-39553-z.

[14] A. Buttenschön and L. Edelstein-Keshet, "Bridging from single to collective cell migration: A review of models and links to experiments," *PLOS Comput. Biol.*, vol. 16, no. 12, p. e1008411, Dec. 2020, doi: 10.1371/journal.pcbi.1008411.

[15] G. Shabestani Monfared, P. Ertl, and M. Rothbauer, "An on-chip wound healing assay fabricated by xurography for evaluation of dermal fibroblast cell migration and wound closure," *Sci. Rep.*, vol. 10, no. 1, p. 16192, Oct. 2020, doi: 10.1038/s41598-020-73055-7.

[16] K.-A. Norton, K. Jin, and A. S. Popel, "Modeling triple-negative breast cancer heterogeneity: Effects of stromal macrophages, fibroblasts and tumor vasculature," *J. Theor. Biol.*, vol. 452, pp. 56–68, Sep. 2018, doi: 10.1016/j.jtbi.2018.05.003.

[17] K.-A. Norton, C. Gong, S. Jamalian, and A. Popel, "Multiscale Agent-Based and Hybrid Modeling of the Tumor Immune Microenvironment," *Processes*, vol. 7, no. 1, p. 37, Jan. 2019, doi: 10.3390/pr7010037.

[18] K. A. Owen *et al.*, "Regulation of lamellipodial persistence, adhesion turnover, and motility in macrophages by focal adhesion kinase," *J. Cell Biol.*, vol. 179, no. 6, pp. 1275–1287, Dec. 2007, doi: 10.1083/jcb.200708093.

[19] H. Wu *et al.*, "Effects of Environmental pH on Macrophage Polarization and Osteoimmunomodulation," *ACS Biomater. Sci. Eng.*, vol. 5, no. 10, pp. 5548–5557, Oct. 2019, doi: 10.1021/acsbiomaterials.9b01181.

[20] P. A. Kramer, S. Ravi, B. Chacko, M. S. Johnson, and V. M. Darley-Usmar, "A review of the mitochondrial and glycolytic metabolism in human platelets and leukocytes: Implications for their use as bioenergetic biomarkers," *Redox Biol.*, vol. 2, pp. 206–210, 2014, doi: 10.1016/j.redox.2013.12.026.

[21] K. T. Iida *et al.*, "Insulin Inhibits Apoptosis of Macrophage Cell Line, THP-1 Cells, via Phosphatidylinositol-3-Kinase–Dependent Pathway," *Arterioscler. Thromb. Vasc. Biol.*, vol. 22, no. 3, pp. 380–386, Mar. 2002, doi: 10.1161/hq0302.105272.

[22] M. B. Maeß, B. Wittig, and S. Lorkowski, "Highly Efficient Transfection of Human THP-1 Macrophages by Nucleofection," *J. Vis. Exp.*, no. 91, p. 51960, Sep. 2014, doi: 10.3791/51960.

[23] M. Genin, F. Clement, A. Fattaccioli, M. Raes, and C. Michiels, "M1 and M2 macrophages derived from THP-1 cells differentially modulate the response of cancer cells to etoposide," *BMC Cancer*, vol. 15, no. 1, p. 577, Dec. 2015, doi: 10.1186/s12885-015-1546-9.

[24]   S. Gordon, W. Newman, and B. Bloom, "Macrophage proteases and rheumatic diseases: Regulation of plasminogen activator by thymus-derived lymphocytes," *Agents Actions*, vol. 8, no. 1–2, pp. 19–26, Jan. 1978, doi: 10.1007/BF01972397.

[25]   H. M. Kaminski and J. B. Feix, "Effects of D-Lysine Substitutions on the Activity and Selectivity of Antimicrobial Peptide CM15," *Polymers*, vol. 3, no. 4, pp. 2088–2106, Dec. 2011, doi: 10.3390/polym3042088.

[26]   K. Kobayakawa *et al.*, "Macrophage centripetal migration drives spontaneous healing process after spinal cord injury," *Sci. Adv.*, vol. 5, no. 5, p. eaav5086, May 2019, doi: 10.1126/sciadv.aav5086.

[27]   S. Pérez-Rodríguez, C. Borau, J. M. García-Aznar, and J. Gonzalo-Asensio, "A microfluidic-based analysis of 3D macrophage migration after stimulation by Mycobacterium, Salmonella and Escherichia," *BMC Microbiol.*, vol. 22, no. 1, p. 211, Aug. 2022, doi: 10.1186/s12866-022-02623-w.

[28]   D. Tyteca *et al.*, "Regulation of Macrophage Motility by the Water Channel Aquaporin-1: Crucial Role of M0/M2 Phenotype Switch," *PLOS ONE*, vol. 10, no. 2, p. e0117398, Feb. 2015, doi: 10.1371/journal.pone.0117398.

[29]   F. Y. McWhorter, T. Wang, P. Nguyen, T. Chung, and W. F. Liu, "Modulation of macrophage phenotype by cell shape," *Proc. Natl. Acad. Sci.*, vol. 110, no. 43, pp. 17253–17258, Oct. 2013, doi: 10.1073/pnas.1308887110.

[30]   M. Cardinal, D. E. Eisenbud, and D. G. Armstrong, "Wound shape geometry measurements correlate to eventual wound healing," *Wound Repair Regen.*, vol. 17, no. 2, pp. 173–178, Mar. 2009, doi: 10.1111/j.1524-475X.2009.00464.x.

[31]   D. R. Gorin, P. R. Cordts, W. W. LaMorte, and J. O. Menzoian, "The influence of wound geometry on the measurement of wound healing rates in clinical trials," *J. Vasc. Surg.*, vol. 23, no. 3, pp. 524–528, Mar. 1996, doi: 10.1016/S0741-5214(96)80021-8.

[32]   C. Ueck *et al.*, "Comparison of In-Vitro and Ex-Vivo Wound Healing Assays for the Investigation of Diabetic Wound Healing and Demonstration of a Beneficial Effect of a Triterpene Extract," *PLOS ONE*, vol. 12, no. 1, p. e0169028, Jan. 2017, doi: 10.1371/journal.pone.0169028.

[33]   T. J. McKee and S. V. Komarova, "Is it time to reinvent basic cell culture medium?," *Am. J. Physiol.-Cell Physiol.*, vol. 312, no. 5, pp. C624–C626, May 2017, doi: 10.1152/ajpcell.00336.2016.

[34]   A. N. Hellman *et al.*, "Examination of axonal injury and regeneration in micropatterned neuronal culture using pulsed laser microbeam dissection," *Lab. Chip*, vol. 10, no. 16, p. 2083, 2010, doi: 10.1039/b927153h.

[35]   H. L. Glenn, J. Messner, and D. R. Meldrum, "A simple non-perturbing cell migration assay insensitive to proliferation effects," *Sci. Rep.*, vol. 6, no. 1, p. 31694, Oct. 2016, doi: 10.1038/srep31694.

[36]   M. Vang Mouritzen and H. Jenssen, "Optimized Scratch Assay for In Vitro Testing of Cell Migration with an Automated Optical Camera," *J. Vis. Exp.*, no. 138, p. 57691, Aug. 2018, doi: 10.3791/57691.

[37]   J. Crank, *The mathematics of diffusion*, 2d ed. Oxford, [Eng]: Clarendon Press, 1975.

[38]   P. K. Maini, D. L. S. McElwain, and D. I. Leavesley, "Traveling Wave Model to Interpret a Wound-Healing Cell Migration Assay for Human Peritoneal Mesothelial Cells," *Tissue Eng.*, vol. 10, no. 3–4, pp. 475–482, Mar. 2004, doi: 10.1089/107632704323061834.

[39]   M. El-Hachem, S. W. McCue, W. Jin, Y. Du, and M. J. Simpson, "Revisiting the Fisher–Kolmogorov–Petrovsky–Piskunov equation to interpret the spreading–extinction dichotomy," *Proc. R. Soc. Math. Phys. Eng. Sci.*, vol. 475, no. 2229, p. 20190378, Sep. 2019, doi: 10.1098/rspa.2019.0378.

[40]   M. D. Matossian *et al.*, "In-depth characterization of a new patient-derived xenograft model for metaplastic breast carcinoma to identify viable biologic targets and patterns of matrix evolution within rare tumor types," *Clin. Transl. Oncol.*, vol. 24, no. 1, pp. 127–144, Jan. 2022, doi: 10.1007/s12094-021-02677-8.

[41]   T. C. Chang *et al.*, "Evaluation of deacetylase inhibition in metaplastic breast carcinoma using multiple derivations of preclinical models of a new patient-derived tumor," *PLOS ONE*, vol. 15, no. 10, p. e0226464, Oct. 2020, doi: 10.1371/journal.pone.0226464.

[42]   E. Sahai *et al.*, "A framework for advancing our understanding of cancer-associated fibroblasts," *Nat. Rev. Cancer*, vol. 20, no. 3, pp. 174–186, Mar. 2020, doi: 10.1038/s41568-019-0238-1.

[43]   A. Aydiner *et al.*, "Metaplastic Breast Carcinoma Versus Triple-Negative Breast Cancer: Survival and Response to Treatment," *Medicine (Baltimore)*, vol. 94, no. 52, p. e2341, Dec. 2015, doi: 10.1097/MD.0000000000002341.

[44]   E. T. Roussos, J. S. Condeelis, and A. Patsialou, "Chemotaxis in cancer," *Nat. Rev. Cancer*, vol. 11, no. 8, pp. 573–587, Aug. 2011, doi: 10.1038/nrc3078.

[45]   A. E. Lohmann and P. J. Goodwin, "Obesity and Breast Cancer: Expanding the Hypothesis Space," *JNCI J. Natl. Cancer Inst.*, vol. 113, no. 2, pp. 107–108, Feb. 2021, doi: 10.1093/jnci/djaa091.

[46]   J. M. Gimble and B. A. Bunnell, Eds., *Adipose-Derived Stem Cells: Methods and Protocols*, vol. 702. Totowa, NJ: Humana Press, 2011. doi: 10.1007/978-1-61737-960-4.

[47]   B. Bunnell, M. Flaat, C. Gagliardi, B. Patel, and C. Ripoll, "Adipose-derived stem cells: Isolation, expansion and differentiation," *Methods*, vol. 45, no. 2, pp. 115–120, Jun. 2008, doi: 10.1016/j.ymeth.2008.03.006.

[48]   D. Kim, S. Y. Kim, S. K. Mun, S. Rhee, and B. J. Kim, "Epidermal growth factor improves the migration and contractility of aged fibroblasts cultured on 3D collagen matrices," *Int. J. Mol. Med.*, vol. 35, no. 4, pp. 1017–1025, Apr. 2015, doi: 10.3892/ijmm.2015.2088.

[49]   G. S. Ashcroft *et al.*, "Tumor necrosis factor-alpha (TNF-α) is a therapeutic target for impaired cutaneous wound healing: TNF-α and wound healing," *Wound Repair Regen.*, vol. 20, no. 1, pp. 38–49, Jan. 2012, doi: 10.1111/j.1524-475X.2011.00748.x.

[50]   G. Schultz, W. Clark, and D. S. Rotatori, "EGF and TGF-α in wound healing and repair," *J. Cell. Biochem.*, vol. 45, no. 4, pp. 346–352, Apr. 1991, doi: 10.1002/jcb.240450407.

[51]   P. Krzyszczyk, R. Schloss, A. Palmer, and F. Berthiaume, "The Role of Macrophages in Acute and Chronic Wound Healing and Interventions to Promote Pro-wound Healing Phenotypes," *Front. Physiol.*, vol. 9, p. 419, May 2018, doi: 10.3389/fphys.2018.00419.

[52]   R. J. Bodnar, "Epidermal Growth Factor and Epidermal Growth Factor Receptor: The Yin and Yang in the Treatment of Cutaneous Wounds and Cancer," *Adv. Wound Care*, vol. 2, no. 1, pp. 24–29, Feb. 2013, doi: 10.1089/wound.2011.0326.

[53]   M. Ritsu *et al.*, "Critical role of tumor necrosis factor-α in the early process of wound healing in skin," *J. Dermatol. Dermatol. Surg.*, vol. 21, no. 1, pp. 14–19, Jan. 2017, doi: 10.1016/j.jdds.2016.09.001.

[54]   A. Yu, Y. Matsuda, A. Takeda, E. Uchinuma, and Y. Kuroyanagi, "Effect of EGF and bFGF on Fibroblast Proliferation and Angiogenic Cytokine Production from Cultured Dermal Substitutes," *J. Biomater. Sci. Polym. Ed.*, vol. 23, no. 10, pp. 1315–1324, Jul. 2012, doi: 10.1163/092050611X580463.

[55]   H. N. Monsuur *et al.*, "Methods to study differences in cell mobility during skin wound healing in vitro," *J. Biomech.*, vol. 49, no. 8, pp. 1381–1387, May 2016, doi: 10.1016/j.jbiomech.2016.01.040.

[56]   E. K. Tiaka, N. Papanas, A. C. Manolakis, and G. S. Georgiadis, "Epidermal Growth Factor in the Treatment of Diabetic Foot Ulcers: An Update," *Perspect. Vasc. Surg. Endovasc. Ther.*, vol. 24, no. 1, pp. 37–44, Mar. 2012, doi: 10.1177/1531003512442093.

[57]   D. Sun, W. Gao, H. Hu, and S. Zhou, "Why 90% of clinical drug development fails and how to improve it?," *Acta Pharm. Sin. B*, vol. 12, no. 7, pp. 3049–3062, Jul. 2022, doi: 10.1016/j.apsb.2022.02.002.

[58]   D. E. Ingber, "Human organs-on-chips for disease modelling, drug development and personalized medicine," *Nat. Rev. Genet.*, vol. 23, no. 8, pp. 467–491, Aug. 2022, doi: 10.1038/s41576-022-00466-9.